UNIVERSITY OF CALIFORNIA, SAN DIEGO

A New Ultra-Cold Positron Beam and Applications To Low-Energy Positron Scattering and Electron-Positron Plasmas

A dissertation submitted in partial satisfaction of the requirements for the degree of Doctor of Philosophy in Physics

by

Steven Jay Gilbert

Committee in charge:

Clifford M. Surko, Chair
Robert Continetti
Andrew Kummel
Thomas O'Neil
Arthur Wolfe

2000

The dissertation of Steven Jay Gilbert is approved and it is acceptable in quality and form for publication on microfilm.

_____

_____

_____

_____

_____

_____

Chairman

University of California, San Diego

2000

This thesis is dedicated to my life-mate, Anne.

Contents

List of Figures

Acknowledgments

I would like to thank all of the people who helped me through the ups and downs of my graduate career.

It goes without saying that the single most influential person in shaping my progress through the graduate program was my advisor, Profesor Cliff Surko. The process of choosing a graduate advisor is part research, part intuition, and part luck. I sought out someone who could guide me through all of the difficulties of a graduate research program. Cliff turned out to be an excellent choice in every respect. He has subtly taught me over the years how to get through, over, or around the many brick walls which arise during the experimental process.

Along with Cliff, I am indebted to all of the people I had the pleasure of working with in his lab. Thanks to Greg, Christof, Koji, James, Gene, Rod, Chris Lund, Chris Kurz, and Judy. Special thanks to Chris Kurz, a wonderful mentor who introduced me to the art of experimental research, and helped greatly on the work presented in this thesis relating to the cold-beam formation. Researcher Rod Greaves offered his keen insight into both experimental design and the physical processes at work. Thanks to him I have gained confidence in my ability to design, build, and implement an experiment from the ground up.

None of this work could have been done without Gene Jerzewski's expert technical assistance. He is a true Zen master of the lab. Despite the many attempts of the lab to break down, he was always there with a smile to tell me not to worry, that it could be fixed, and he was always right. For the last year James Sullivan has educated me in the ways of an atomic-physicist. He has also helped to take much of the recent data presented in Chapter 4, while I have been hunched over the computer writing this dissertation.

On a personal note, I would like to thank my family and friends for keeping me mostly sane through it all. Thanks to Mom, Eric, Dad, Pauline, Dennis, Nancy, Debbie, Mike, Stefanie, Jordan, Nan, and Ken, who complete one of the greatest families ever. Most of all I would like to thank Anne, for sticking so close to me through the thick and thin of it all. She has been a great source of inspiration and the Ph.D. degree is as much hers as it is mine. I would also like to thank my mother for teaching me that the day to day of work was something to be enjoyed not wished away until the next weekend or vacation. She also never discouraged me from asking why, no matter how many frustrating times I posed the question, and this is what led me into the sciences. I owe my sense of perspective to my brothers and sisters, although we have each pursued different things to become happy, your successes have inspired me.

An integral aspect of my life has been my love of the outdoors which originated during the many walks through the woods taken with my step-farther Eric. Whether I am hiking, skiing, climbing, or biking, he will always be part of me when I am in the woods. Even though Eric started my love of the outdoors, he would never have pushed me towards rock-climbing. For that I owe my good

friend Todd, thanks for being a great teacher. Since I have been in San Diego, the Thursday-Sunday climbing group has been responsible for an uncountable number of great times outdoors. Thanks Doug, Garnet, Cindy, Frank, Mike, and all of the other wonderful people in the group.

Lastly, I would like to thank the friends I have made throughout my college and graduate career for all the good times that they have given me. At the University of Rochester, I met Dylan and learned that being yourself, and remaining forever a kid was something worth striving for. At Rutgers, Amy started me on the way to making a number of life-choices, including becoming a vegetarian. Since I have been at the University of California, San Diego, my friends Thor, Neda, and Jason, were first my study partners, and later my commiseration partners, as we all worked our way through the graduate process. Finally, thanks to Ray for sharing his enthusiasm for life, always with a stupid joke on hand.

Vita

May 12, 1970	Born, New Jersey, USA.
1993	B.A., Physics, Rutgers University.
1994	Research Assistant, University of California, San Diego.
1995	M.S., Physics, University of California, San Diego.
2000	Ph.D., Physics, University of California, San Diego.

Publications

ARTICLES

1. S. J. Gilbert, D. H. E. Dubin, R. G. Greaves, and C. M. Surko, "An Electron Positron Beam-Plasma Instability," manuscript in preparation.

2. S. J. Gilbert, J. Sullivan, R. G. Greaves, and C. M. Surko, "Low Energy Positron Scattering from Atoms and Molecules using Positron Accumulation Techniques," *Nuclear Instruments and Methods in Physics Research B*, in press.

3. S. J. Gilbert, R. G. Greaves, and C. M. Surko, "Positron Scattering from Atoms and Molecules at Low Energies," *Physical Review Letters* **82**, 5032-5035 (1999).

4. C. Kurz, S. J. Gilbert, R. G. Greaves, and C. M. Surko, "New Source of Ultra-Cold Positron and Electron Beams," *Nuclear Instruments and Methods in Physics Research B* **143**, 188-194 (1998).

5. S. J. Gilbert, C. Kurz, R. G. Greaves, and C. M. Surko, "Creation of a monoenergetic pulsed positron beam," *Applied Physics Letters* **70**, 1944-1946 (1997).

6. K. Iwata, R. G. Greaves, C. Kurz, S. J. Gilbert and C. M. Surko, "Studies of positron-matter interactions using stored positrons in an electrostatic trap," *Materials Science Forum* **24**, 223-227 (1997).

7. C. M. Surko, K. Iwata, C. Kurz, and S. J. Gilbert, "Atomic and Molecular Physics using Positrons in a Penning Trap," *Photonic, Electronic and Atomic Collisions*, F. Aumayr and H. P. Winter, eds. (World Scientific, 1997), pp. 383-392.

INVITED TALKS

- S. J. Gilbert, "Low-energy Positron Scattering from Atoms and Molecules," 10th Workshop on Low-Energy Positron and Positronium Physics (a satellite conference of the International Conference on the Physics of Electronic and Atomic Collisions), Tsukuba, Japan (1999).

Fields of Study

Major Field: Physics

Studies in Atomic and Molecular Physics
Professor Clifford M. Surko

Studies in Plasma Physics
Professor Clifford M. Surko

Studies in Positron Physics
Professor Clifford M. Surko

ABSTRACT OF THE DISSERTATION

A New Ultra-Cold Positron Beam and Applications To Low-Energy Positron Scattering and Electron-Positron Plasmas

by

Steven Jay Gilbert

Doctor of Philosophy in Physics

University of California, San Diego, 2000

Professor Clifford M. Surko, Chair

A new technique was developed to generate intense, cold, magnetized positron and electron beams. The beam is formed by extracting particles from a thermalized, room-temperature, single-species plasma confined in a Penning trap. Cold positrons with an energy spread of 18 meV can be produced either in a pulsed or continuous mode at energies ranging from < 50 meV upward. Cold, quasi-steady-state electron beams have also been generated with electron currents of 0.1 μA for several milliseconds using this method. These cold beams have been used to study both positron-matter interactions and electron-positron plasma interactions. Positron-atom differential cross-sections (DCS), positron-molecule total vibrational excitation cross sections, and total scattering cross sections are presented. Absolute values of the DCS for elastic scattering from argon and krypton are measured at energies ranging from 0.4 to 2.0 eV and agree well with theoretical predictions. The first low-energy positron-molecule vibrational excitation cross sections were measured (i.e., for carbon tetrafluoride at energies ranging from 0.2 to 1 eV), and recent extensions of this work to CO, CO_2, and CH_4 are described. Total cross section measurements at the lowest positron energies (i.e., down to 50 meV) are also discussed. The electron-positron plasma study consists of an electron beam transmitted through a positron plasma stored in a quadrupole Penning trap. The transit-time instability, which is excited by the beam, was studied from onset through the maximum in growth rate. The experimental results are compared with the results of a new cold-fluid model and are in good agreement over a broad range of energies and beam currents.

Chapter 1

Introduction

Positrons were first predicted by Dirac [20] in 1930 and discovered soon after by Anderson in 1932 [3, 4]. Anderson made his discovery by studying tracks of cosmic rays in a cloud chamber. He noticed a particle with a positive charge that appeared to be lighter than both the proton and the alpha particle (the only known positive particles at the time). The new particle appeared to have the same mass as an electron. Anderson called this new particle a positive electron or positron.

Two years later Joliot generated the first man-made radioelement, and coincidentally the first man-made positron source, by bombarding a thin sheet of aluminum with alpha particles [57]. The isotope ^{30}P that he created decays into a stable isotope of silicon by emitting a β^+ (i.e., a positron) and a neutrino. Thus, Joliot developed the first radioactive source of positrons. Advances in positron sources progressed quickly after Joliot's discovery, generating stronger sources with longer life times.

Since the discovery of the positron [3], it has been clear that the study of positron interactions with matter is an important and insightful area of physics research. In order to study positron interactions with matter experimentally, two criteria must be met. The first is that the signal-to-noise ratio of the experiment must be sufficiently large. The second is that the energy and or spatial resolution of the positrons must be small enough for these results to be meaningful.

The signal-to-noise ratio in a positron-matter experiment is typically related to the abundance of low-energy positrons and the efficiency of their detection. Positrons can either be detected using a scintillator, which detects the γ-ray emitted when the positron annihilates with an electron, or by measuring the positron charge using a charge multiplier. In either case, low-noise positron detectors with near unity efficiency are more-or-less conveniently available.

1.1 Positron Sources

Positron sources of sufficient yield to perform experiments have been available almost since the discovery of the positron. Currently, there are two methods for producing a high intensity positron source. Positrons can either be created using a linear accelerator (LINAC) [1, 48, 101] or a radioactive isotope. A LINAC produces positrons by bombarding a high-Z material such as tantalum with high-energy electrons ($\sim$ 100 MeV). The rapid deceleration of the electron generates Bremsstrahlung γ rays, which in turn create electron-positron pairs. The positrons are then extracted and formed into a positron beam. The main advantage of a LINAC-based positron source is that the intensity can be very high (i.e., $> 10^{11}$ positrons/s). Disadvantages of using a LINAC-based positron source include an electrically noisy environment generated during the high-energy electron pulse, limited availability of LINAC facilities, and relatively high capital and operating costs.

Radioactive positron sources have improved considerably since Joliot's discovery of a phosphor source with a three minute half-life. The most common sources in use today are ^{22}Na, ^{68}Ge, and ^{58}Co. The main advantages of using a radioactive source are that they are relatively inexpensive (e.g., compared to a LINAC source), small, and can be self contained. A self contained source is critical for the accumulation and trapping of positrons used in the experiments described in this thesis. The positron accumulation efficiency is very sensitive to impurities, such as hydrocarbons, and so having to connect the vacuum chamber to another vacuum system, such as a LINAC, would make maintaining a hydrocarbon free system more difficult.

A ^{22}Na source is used in the experiments described in this thesis. It has a 2.6 year half-life and is attainable with activities up to 150 mCi. The only disadvantage to using a radioactive source over a LINAC based positron source is a lower positron intensity ($\sim 10^9$ positrons/s for 150 mCi ^{22}Na source vs. 10^{11} for a LINAC). For our experiments, the advantages clearly outweigh the disadvantages making a radioactive source an attractive choice.

Positrons emitted from either radioactive sources or particle accelerators have a broad energy spread ranging up to several hundred keV and therefore need to be slowed down before they can be effectively used in a positron-matter experiment. Unfortunately, advances in producing mono-energetic positrons were not as forthcoming as advances in positron sources. In fact, as late as 1969 in a review on the theory of 'Positron Collisions', Bransden lamented that:

> the points of contact between the experiments and theory are not as many as could be wished and are somewhat indirect. The reason for this is that, in contrast to the electron in positron scattering, there are at present no controlled mono-energetic beams of low-energy positrons [8].

1.2 Moderators to Produce Low-Energy Positrons

In 1972, Costello *et al.* made a critical breakthrough, finding evidence that fast positrons impinging on a gold surface are slowed to a few electron volts and then ejected from the surface [17]. This resulted in a practical technique to produce a low-energy positron beam. Not long after this, improvements on the gold moderator were made by Coleman *et al.* [15] and then further improved by Canter *et al.* [11]. These discoveries led to the first low-energy positron beams used in positron-matter experiments, which were measurements of the total cross sections for low-energy positron-helium collisions [11]. Canter's moderator consisted of a system of gold vanes. Each vane had a fine MgO powder deposited onto it, increasing the moderating efficiency by a factor of 10 from that of the gold vanes alone. A positron beam of variable beam energy was produced by extracting the moderated positrons through an electrostatic field. The final moderator had an energy spread of 1.5 eV FWHM and a yield of $\epsilon \sim 10^{-5}$, where ϵ is the ratio of low energy positrons extracted from the moderator to the high energy positrons impinging on the moderator.

Work on producing more efficient positron moderators has progressed continually since Canter's work [11]. Single crystal metal moderators, such as tungsten [33], nickel [110] and copper [77] have efficiencies as large as $\epsilon \sim 10^{-4}$. Tungsten is especially appealing because of its narrow energy distribution, 0.3 eV FWHM, making possible some of the highest resolution positron-matter experiments to date [60, 100]. The introduction of solid rare-gas moderators in the 1980s improved positron moderator efficiencies by another two orders of magnitude [80]. The most efficient rare-gas moderator to date is made by freezing neon gas onto a metal surface at ~ 8 K. For the experiments described in this dissertation, a solid neon moderator was used. It has an efficiency $\epsilon \sim 10^{-2}$, and an energy spread of 1 eV FWHM.

Until the work presented in this thesis, almost all efforts to reduce the energy spread in the available positron beam sources and to increasing positron brightness have been focused on improved moderator schemes. One successful method is through the use of *remoderators*. It has been shown that positron moderator efficiency increases as the energy of the incident positron decreases, and can be as large as $\epsilon \sim 0.3$ for a 3 keV incident positron [9]. There is also evidence that the energy distribution of the emitted positrons is nearer to that of a thermalized distribution at the moderator temperature. For example, the moderated beam energy distribution of a 3 keV incident positron beam on a Ni(100) moderator at 300 K and 23 K is 80 meV and 24 meV FWHM, respectively [25]. Unfortunately the moderation efficiencies are greatly reduced as the moderator temperature is decreased [9], and so a cold beam can only be generated using this technique at the expense of a low overall moderator efficiency.

Another use of remoderators is to increase the positron beam brightness (i.e., flux per unit area per unit energy). This can be accomplished by accelerating

and then electrostatically focusing a moderated beam onto a second moderator. The re-emitted positrons will have a spatial resolution comparable to that of the focused beam and an energy resolution ~ 0.1 eV. By successive acceleration, focusing, and remoderation steps, smaller beam sizes can be achieved without the expense of increased energy spread [59]. Because of the high remoderation efficiency, the brightness of such a beam can be increased although, as mentioned above, the positron flux decreases with each remoderation step.

Since Canter's positron-helium total cross section measurements [11], a large body of work has been performed to study positron-matter interactions at low-energies. Examples in atomic physics include total cross section and positron annihilation rate measurements, inelastic cross sections for positronium formation, excitation and ionization of atoms, and differential elastic scattering cross sections. Excellent reviews on positron-atom and positron molecule cross sections measurements can be found in Refs. [12, 53, 60]. An account of the earlier work on measurements of total cross sections can be found in Refs. [40,73]. There have also been great advances in the study of surfaces using slow positron beams, including defect-depth profiling, low energy positron diffraction and reflection, and high-energy positron diffraction [78, 94].

1.3 Positron Physics at Lower Energies

Despite these developments, there is still a largely unexplored region of energy (i.e. < 1 eV) which cannot be studied easily using the existing moderated beams. This is a very interesting energy regime. For example, in atomic physics many important processes occur at these low energies, such as vibrational [19, 28, 62] and rotational [30] excitation of molecules, which have not yet been experimentally studied by positron impact. The low-energy interaction of positrons and ordinary matter is important in fields such as astrophysics, atomic physics, and chemical physics. Exploring this energy regime should provide important new information, such as understanding the role of virtual positronium states in positron interactions with matter [53], the mechanisms by which positrons bind to atoms and molecules [39], and the process of large molecule fragmentation by positrons [47, 89].

1.4 Overview of the Thesis

This thesis describes a new technique to produce a state-of-the-art mono-energetic positron beam [32, 65]. To form a cold beam, positrons are first accumulated in a Penning trap where they thermalize to room temperature through collisions with a background gas. These cold positrons are then extracted from the trap by decreasing the depth of the potential well confining them, thus forcing the cold positrons out of the potential well and into a beam. The beam has an energy

distribution of 18 meV FWHM, and it can be tuned over a wide range of energies from < 50 meV upward. Both pulsed and steady-state beams can be produced depending on the requirements of the experiment at hand. Positron throughput is $> 1 \times 10^6$ positrons/s, and in pulsed operation, the beam brightness is greater than that achieved using two remoderation stages [94].

This thesis also describes the first uses of this new beam in two areas of positron-matter interactions. The first is a study of positron-atomic and positron-molecular physics at energies below 1 eV. We have measured the differential cross sections for positron collisions with argon and krypton at energies below that of any previous measurement. We have also made the first measurements of the cross sections for vibrational excitation of molecules by positrons, studying the excitation of CF_4 at positron energies as low as 0.2 eV. Most recently we have extended our study of positron-molecular vibrational cross sections to include CO, CO_2, and CH_4. We have also recently studied the total cross section for positron-molecule scattering at energies from 50 meV to several electron volts, which represents a higher energy resolution measurement than any previous work. Both the technique developed to produce the cold positron beam and the new method to measure scattering cross sections are in the early stages of development. We expect improvements in both will continue to extend our ability to explore atomic and molecular physical processes at energies below 1 eV.

The second area of positron-matter interactions we have examined using the cold beam is the study of electron-positron plasmas. Because of difficulties in simultaneously confining both positrons and electrons, the simplest experimental arrangement in which electron-positron plasma interactions can be studied is an electron beam passing through a positron plasma. The unique ability to accumulate and store large numbers of positrons that the group has developed greatly facilitates this kind of experiment. The work by Greaves *et al.* [34] was the first experimental study of this system; it was done by transmitting an electron beam through positron plasmas stored in Penning traps with both cylindrical and quadrupole potential wells. In these experiments, a conventional hot-cathode electron gun was used as the electron beam source. Unfortunately, the large energy spread of the hot-cathode electron gun restricted beam-plasma studies to energies above ~ 1 eV.

Although conventional means to create mono-energetic electron beams are available, they do not work in the high magnetic field (~ 1 kG) necessary to confine the positron plasma. We have been able to apply the same technique used to produce cold positron beams to generate cold electron beams. Because this technique was designed to operate in the high field needed for the beam-plasma experiments, it was an ideal way to carry out the beam-plasma experiments at the lower beam energies where the maximum growth rate and instability onset were predicted to occur. This thesis discusses research using the cold electron beam to investigate further the instability generated by passing a cold electron beam through a positron plasma confined in a quadrupole well. We

were able to study the instability down to beam energies as low as ~ 0.2 eV, which corresponds to the onset of the instability.

The organization of the thesis is as follows. Chapter 2 discusses specific details of the experimental apparatus which pertain to all of the experiments described in this thesis. The technique used to generate cold positron and electron beams is presented in Chapter 3 along with specific characteristics of the types of beams. Chapters 4 and 5 describe new experiments using the cold beams to study positron-matter interactions. In Chapter 4 positron-atom and positron-molecule studies are described in the largely unexplored range of energies below 1 eV. Positron-electron plasma physics studies are described in Chapter 5, in the form of an electron-beam positron-plasma transit-time instability. Finally, a summary of the work and concluding remarks are presented in Chapter 6.

Chapter 2

General Description of the Experiment

This chapter describes the apparatus and techniques used which are common to all aspects of the experiments discussed in this thesis. Positrons emitted from a radioactive ^{22}Na source are moderated to low energies and magnetically guided into a three stage Penning trap used to accumulate the positrons. The entire system is enclosed in a ultra-high vacuum (UHV) chamber, which has achieved pressures as low as 6×10^{-11} torr. A confining magnetic field is generated using a number of solenoids which surround the vacuum vessel. The field varies from ~ 200 G in the source chamber and beam tube up to 1500 G in the accumulator, where a high field is necessary for good positron confinement. Once a plasma is accumulated it is either used as a reservoir to form a cold beam as described in Chapter 3, or as a cold plasma in a beam-plasma experiment (see Chapter 5).

The apparatus described in this chapter has been completely redesigned from the knowledge gained by operating an earlier version of a positron accumulator. A detailed description of the earlier accumulator can be found in Ref. [84]. Some of the work described in this thesis was done using the earlier apparatus. In these cases, a note will be made in the text that the earlier accumulator was used, and any additional information pertaining to the particular experiment is given. However, in most cases, the operation of these two machines is similar enough to not warrant this.

2.1 Charged Particle Motion in a Magnetic Field

Because all of the experiments described in this thesis are conducted in a magnetic field, it is helpful to briefly review charged particle motion in such a field.

The most basic motion is that of a charged particle moving through a constant magnetic field. Figure 2.1 shows a schematic diagram of this motion. The particle follows a helical orbit which can be conveniently split into two distinct

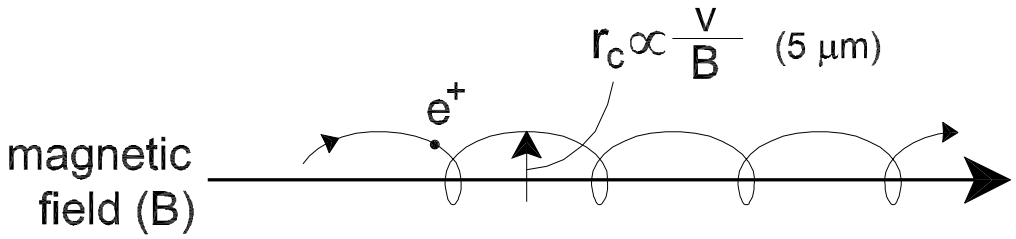

Figure 2.1: Charged particle motion in a magnetic field. The helical path can be separated into a circular motion in the plane perpendicular to the field and a linear motion along the field. The total kinetic energy, E, of the particle is the sum of the kinetic energy associated with motion along the field, $E_{||}$, and the kinetic energy due to the circular motion, $E_{\perp}$, where $E = E_{\perp} + E_{||}$.

motions, a linear motion along the magnetic field and a circular motion in the direction perpendicular to the field. The radius of this orbit, known as the cyclotron radius r_c, is proportional to the particle velocity and inversely proportional to the magnetic field strength. Specifically, $r_c = mv_{\perp}/eB$, where m, is the charged particle mass, $v_{\perp}$ is the particle velocity perpendicular to the magnetic field, e is the charge, and B is the magnetic field strength. For example, a typical positron in our cold positron beam (see Section 3.3) will have $v_{\perp} \sim \sqrt{2kT/m}$, where kT is the thermal energy of the room temperature positrons (≈ 0.025 eV). The cyclotron radius of such a positron when placed in a 0.1 tesla field will therefore be, $r_c \sim 5$ μm, which has been greatly exaggerated in Fig. 2.1 to show the helical motion.

It is convenient to split the total particle kinetic energy into the components due to these two motions. We express the total energy of the particle as $E = E_{\perp} + E_{||}$, where $E_{||}$ is the kinetic energy along the magnetic field and $E_{\perp}$ is the kinetic energy in the circular motion perpendicular to the magnetic field. Chapter 4 describes how this convention simplifies the analysis of the scattering events in the strong magnetic field.

When the magnetic field strength varies as a function of position, the trajectory of the charged particles can be described with the help of a useful adiabatic invariant. The ratio $E_{\perp}/B$ is adiabatically invariant as long as the distance over which the magnetic field strength changes appreciably is small compared to the cyclotron radius. For example, as a charged particle moves into a region of decreasing magnetic field $E_{\perp}$ must decrease. Conservation of energy implies that $E_{||}$ must therefore increase. As the particle continues to move into a weaker field, $E_{||}$ increases until nearly all of the particles energy is in $E_{||}$. At this point the charged particle is moving almost directly along the magnetic field with a very small cyclotron radius. Section 4.3.2 describes how we take advantage of the adiabatic invariant to determine the total vibrational cross section of a positron-molecule scattering event.

Lastly, when the lines of magnetic induction curve, and the radius of curvature R is large compared to the cyclotron radius, the zero-order approximation to the motion of the particle in the field is to follow the lines of force. For the experiments described here this approximation always holds, and therefore the guiding center of the particles, to zero-order, always follows the magnetic field. To first-order there is a drift velocity in the guiding center motion, associated with the curvature R. This motion, which is in a direction perpendicular to the magnetic field, is too small to effect the particle trajectory in a single pass, for example, when transferring the positrons from the source to the accumulator (see Section 2.3). When the particles make many passes through a curved region of field the accumulative drift can be quite large. For this reason, the magnetic field is highly uniform throughout the positron accumulator, therefore minimizing any drifts which would reduce the confinement time of the trapped positrons.

2.2 Source and Moderator

There are several possible approaches to generating the slow positron beams necessary for trapping and accumulation [88, 94]. In all of these approaches the positrons originate from either a radioactive source or from a particle accelerator. In the case of radioactive sources, one of the most intense positron producers is ^{64}Cu. Although the fast-positron count rate for ^{64}Cu is quite large (1×10^{12} e^+/s), the production requires a reactor with a high thermal neutron flux and must be generated daily because it has a half-life of only 12.8 h [69]. For these reasons, we have chosen to use the more practical radioactive positron source ^{22}Na. ^{22}Na has many properties which make it a good choice, most importantly it has a high branching ratio of 90%, a long life time, and is commercially available.

The ^{22}Na positron source that is used in the experiment was obtained from DuPont Merck Pharmaceuticals in September 1997 with a source strength of 150 mCi and a quoted efficiency of 70% of the 2π value. The ^{22}Na source has a half life of 2.6 y and emits a broad energy range of positrons with a fairly continuous spectrum up to 540 keV. The source is sealed in a titanium capsule used to isolate it from the vacuum system. The current source efficiency is reported to be a factor of two higher than past efficiencies. This improvement is obtained by increasing the purity of the source material, and therefore reducing positron annihilation.

In order to slow the keV positrons to eV energies a moderator is needed [13, 41, 79, 80, 94]. Positron moderators take advantage of positron interactions with solids as follows. A high energy positron hits the solid and initially looses energy by ionization or creation of electron-hole pairs. At lower energies, the positron loses energy by positron-phonon interactions and eventually thermalizes

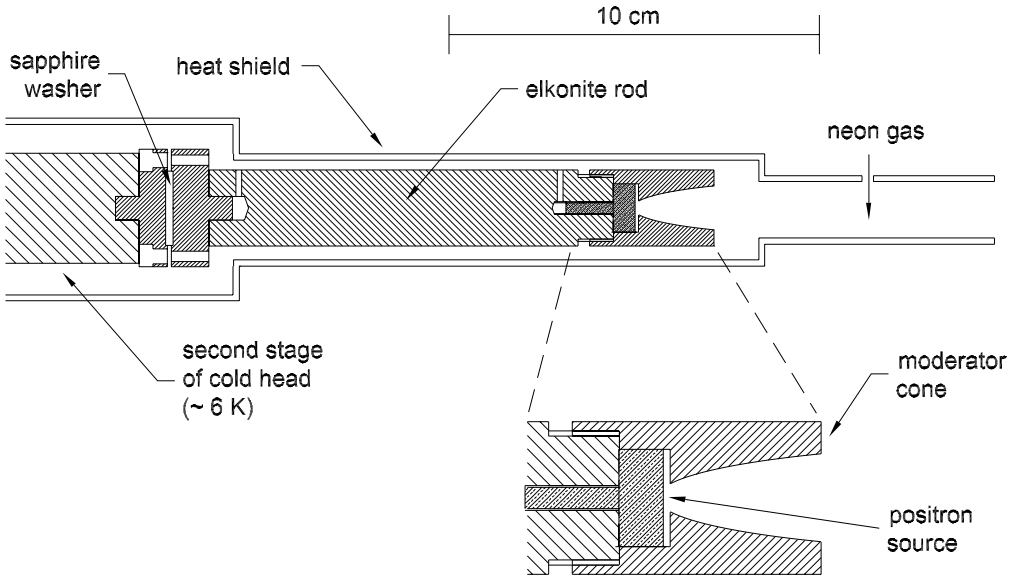

Figure 2.2: Schematic diagram of the positron source and moderator showing the positron source relative to the moderator cone. The cone is kept at ~ 8 K by a two-stage refrigerator, which is in thermal contact through an elkonite rod with the cone. A heat shield surrounds the source and cone to reduce the radiative heat loss.

with the solid. Because the time it takes for the positron to thermalize ($\sim 10^{-12}$s) [64] is short compared to their annihilation lifetime, a fraction of the thermalized positrons can diffuse (via positron-phonon collisions) to the surface. By using a solid with a positive work function, a portion of these positrons are then ejected from the solid with an energy comparable to the positron work function of the solid.

There are a number of different types of moderators in use. Single-crystal metal moderators, such as tungsten [33], nickel [110] and copper [77] were originally used, and have efficiencies as large as $\epsilon \sim 10^{-4}$. More recently rare-gas solid moderators such as neon have been shown to have much higher efficiencies ($\epsilon \sim 2.6 \times 10^{-2}$) [35], and are therefore used in these experiments. The minor draw-back of a larger energy spread (~ 1 eV FWHM in the neon moderator vs. ~ 0.3 eV FWHM for the tungsten) is not an important factor because the positron accumulator (see Section 2.4) is almost as efficient at trapping a positron beam generated from the neon moderator as it is from the tungsten moderator [52].

Figure 2.2 is a schematic diagram of the source and moderator arrangement. The ^{22}Na source is located in a titanium capsule which has a 13 μm titanium window welded onto its front. The titanium capsule is attached to an elkonite rod (tungsten-copper alloy used for its high thermal conductivity and good γ-ray shielding abilities), which is, in turn, attached to a two-stage refrigerator. An

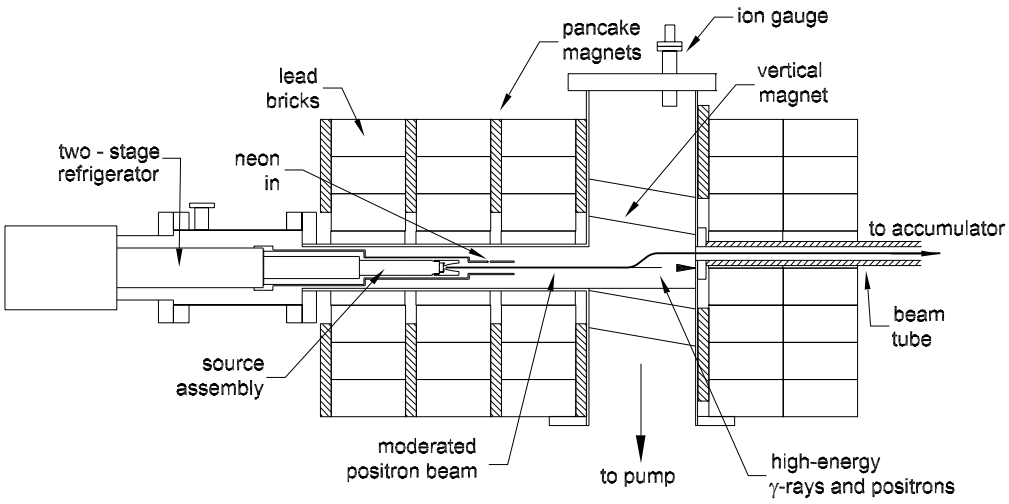

Figure 2.3: Schematic diagram of the positron source and moderator vacuum chamber showing the source and moderator mounted to the two-stage refrigerator. The source assembly is offset from the beam tube to block the line of sight from the source to the accumulator. A magnetic field generated by a set of pancake coils and a vertical coil guides the moderated positrons into the beam tube. Radiation from the source is blocked by lead bricks, which surround the vacuum chamber.

OFHC aluminum cone is screwed on over the titanium capsule and serves as a cold surface to form a frozen neon moderator. The cone is in thermal contact with the second stage of the refrigerator and is typically cooled to ~ 8 K, which is measured using a calibrated silicon diode. Thermal regulation is obtained by a heating coil located on the refrigerator and a control feedback system. To reduce the heat load on the second stage, a heat shield (35 K) surrounds the entire source/moderator assembly and is in thermal contact with the first stage of the refrigerator, which has a greater heat capacity.

A schematic diagram of the UHV vacuum chamber that houses the source and moderator is shown in Fig. 2.3. The vacuum system is pumped by a ion pump and has a typical base pressure of $\sim 5 \times 10^{-8}$ torr. The positron moderator is generated by introducing neon gas directly in front of the 8 K moderator cone (see Fig. 2.2). We have no direct measurement of the neon gas pressure near the moderator cone, and instead regulate the pressure using a stable ion gauge located in the UHV chamber. The pressure outside is maintained at $\sim 2 \times 10^{-4}$ torr, and one can assume that the pressure near the cone is much higher. The moderated positron count rate is monitored as a function of time during the grow cycle by a small γ-ray detector located near the beam tube, and the growth cycle is stopped when the positron count rate saturates, which typically takes ~ 1 h. After the moderator has finished growing, its efficiency continues to rise for ~ 1 h, perhaps by a rearrangement of the neon crystal

structure. A moderator grown in this fashion typically yields a positron flux of $\sim 6 \times 10^6 e^+/s$ and can last for many months. The moderator used in our earlier apparatus had a life time of ~ 12 h, making the calibration of long term experiments difficult. The current improvement, which we attribute to a cleaner UHV system, eliminates this difficulty. A detailed description of the solid neon moderator apparatus and operation can be found in Ref. [35]

2.3 Beam Extraction and Transport

The neon moderator is biased to $\sim$ 30 V for beam extraction and efficient positron accumulation (see Section 2.4). The moderated positrons are guided from the moderator to the accumulator by a magnetic field ($\sim$ 200 G) generated from the series of pancake coils shown in Fig. 2.3. Pancake coils are used so that lead shielding can be located as close to the ^{22}Na source as possible. To prevent the 1.27 MeV γ-rays and high-energy positrons emitted from the source from interfering with the γ-ray detectors located beyond the accumulator, the source and moderator are offset from the axis of the positron accumulator by 2 cm. A vertical coil is wound around the source chamber to transport the low-energy positrons from the offset position onto the axis of the accumulator, while the high energy positrons and γ-rays hit the wall of the source chamber. The positrons then enter the beam tube, which is a small diameter ($\sim$ 2 cm) vacuum tube surrounded by a magnetic coil. They are then guided into the positron accumulator.

2.4 Positron Accumulation

The low-energy positron beam enters the positron accumulator at a rate of $\sim 6 \times 10^6 e^+/s$. A specially designed Penning-Malmberg trap [38,84,104] is then used to efficiently trap the positrons. Figure 2.4 shows a schematic diagram of the modified trap used in the experiment. The trap uses a set of cylindrically symmetric electrodes to produce an electrostatic potential well that confines the positrons axially. Radial confinement is achieved with a magnetic field generated along the axis of the electrode structure. This design, which offers excellent long-term confinement of positrons [71,86], enabled the creation of the first laboratory positron plasma in 1989 [104].

Trapping the slow positron beam as it enters the accumulator is a non-trivial task. For the case of an abundant charged particle, such as electrons, an acceptable trapping scheme is simply to raise a potential barrier when the trap is flooded with particles, thereby trapping all of the particles within the electrodes. Because electron beams with densities $n_b > 10^9 cm^{-3}$ are easily attained, electron plasmas with the same density can be trapped using the above technique. For the case of positrons from our ^{22}Na source and moderator the beam density is

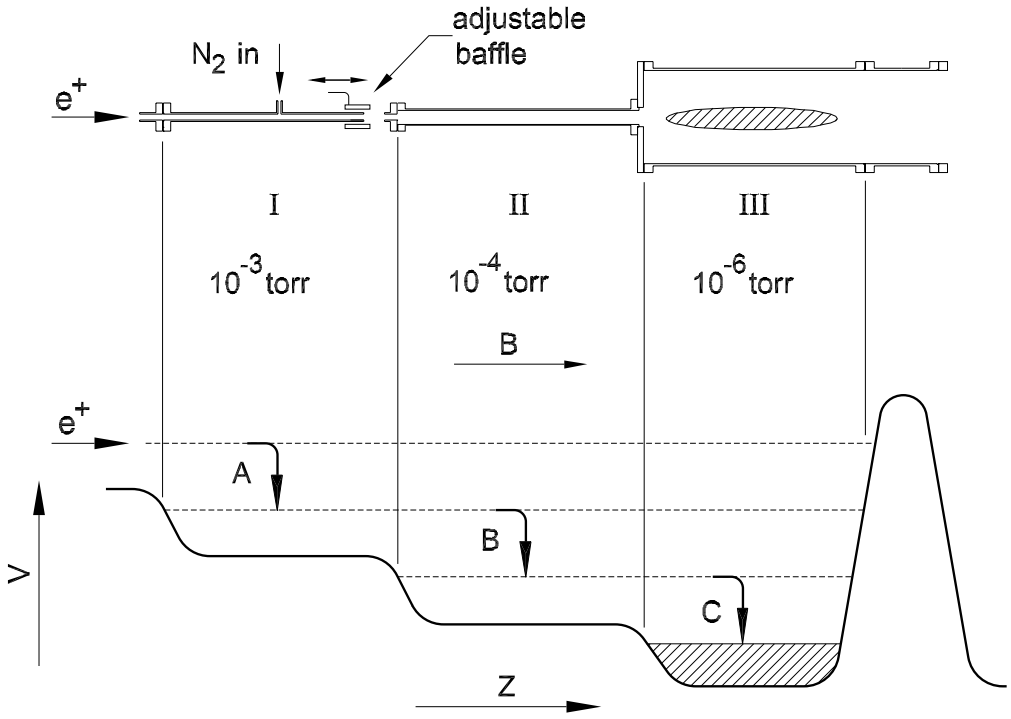

Figure 2.4: Schematic diagram of the three-stage positron accumulator, showing the electrode structure (above), which is used to create regions with different pressures of nitrogen buffer gas by differential pumping. (below) The electrostatic potential profile used to trap the positrons.

only $n_b > 10^{-1}\mathrm{cm}^{-3}$, therefore an efficient means of accumulating positrons over a relatively long period of time must be used.

To achieve this, a buffer-gas trapping scheme is used in the following manner. The moderated positrons enter the positron accumulator with a beam energy of ~ 32 eV and an energy spread of ~ 1 eV FWHM. A nitrogen buffer gas is introduced into the middle of the first stage of the accumulator and is pumped out at both ends. Differential pumping is used to generate three pressure regimes from 10^{-3} down to 10^{-6} torr, corresponding to the three stages. As the moderated positrons enter the first stage of the accumulator they inelastically collide with the N_2 buffer gas ("A" in Fig. 2.4) losing energy, and becoming trapped in the potential well. By making another two inelastic collisions with the buffer gas ("B" and "C") the positrons move from the relatively high pressure region of stage I into the low pressure region of stage III, where they cool to room temperature (0.025 eV) in approximately 1 s by further collisions with the N_2 buffer gas [38].

The most effective inelastic process for trapping the positrons is electronic excitation of N_2 by positron collision at approximately 8.6 eV. In order to max-

imize the trapping efficiency via the electronic excitation, the potential well depth in each of the stages must be adjusted so that the cross section of the electronic excitation is maximized through that stage. Unfortunately, another dominant cross section which turns on at energies near the electronic excitation is positronium formation at 8.8 eV. Because positronium formation is a positron loss mechanism it is critical to operate the accumulator at energies below where this is a dominant loss mechanism. In practice, the maximum trapping efficiency is found by mapping out the trapping rate as a function of well depth and searching for a maximum. Typically the maximum efficiency occurs when the accumulator is operated with a step height between stages of $\Delta V \sim 9$ V.

Another critical factor which effects the trapping efficiency of the accumulator is the buffer gas pressure profile through the three stages. In order to trap the moderated positrons the pressure in the first stage is adjusted so that the probability of an inelastic collision occurring on the first pass through the accumulator is large (labeled "A" in Fig. 2.4). Once the positron has been trapped it can make multiple passes through all three stages until the inelastic collision labeled "B" occurs and the positron falls into the next potential well. The pressure in stage II has to be large enough for the second transition to occur before the positron annihilates on the N_2 buffer gas in stage I. Similarly, once the positron is trapped in stages II and III, the transition into the stage III ("C") must occur before the positron annihilates in stage II.

The pressure of the nitrogen buffer gas in all three stages can be adjusted as follows. The stage I pressure is controlled by adjusting the rate of nitrogen introduced into the center of the stage I electrode structure. The right end of the stage I electrode has a 5 cm long slotted section which allows some of the buffer gas to exit the stage I electrode before entering stage II. A baffle, which is externally adjustable, can slide over this slotted region restricting this flow of gas through the slots (see Fig. 2.4). By moving this baffle from a completely closed to open position the pressure ratio between the stage I and stage II electrodes can be adjusted from 2 to 20, respectively. The stage III pressure can be altered by adjusting the flow of a second nitrogen gas line which is located near the third stage. In practice, the trapping efficiency of the accumulator is maximized by adjusting the large parameter space, which includes the accumulator electrode potentials and the pressure profile through each of the three stages, and searching for maxima. The electrode optimization is achieved using a computer assisted optimization routine [38]. The pressure optimization, which is not yet under computer control, was maximized by manually sweeping the parameter space.

There are two regimes in which the accumulator is operated. Typically the accumulator is run at its highest trapping efficiency. Figure 2.4 shows the pressures used in the three stages to achieve the maximum trapping efficiency, which for our new accumulator is $\sim 20\%$. Operating the accumulator for maximum efficiency requires a fairly high pressure in the third stage and therefore the positron life time is only ~ 40 s. If a longer positron lifetime is needed the nitro-

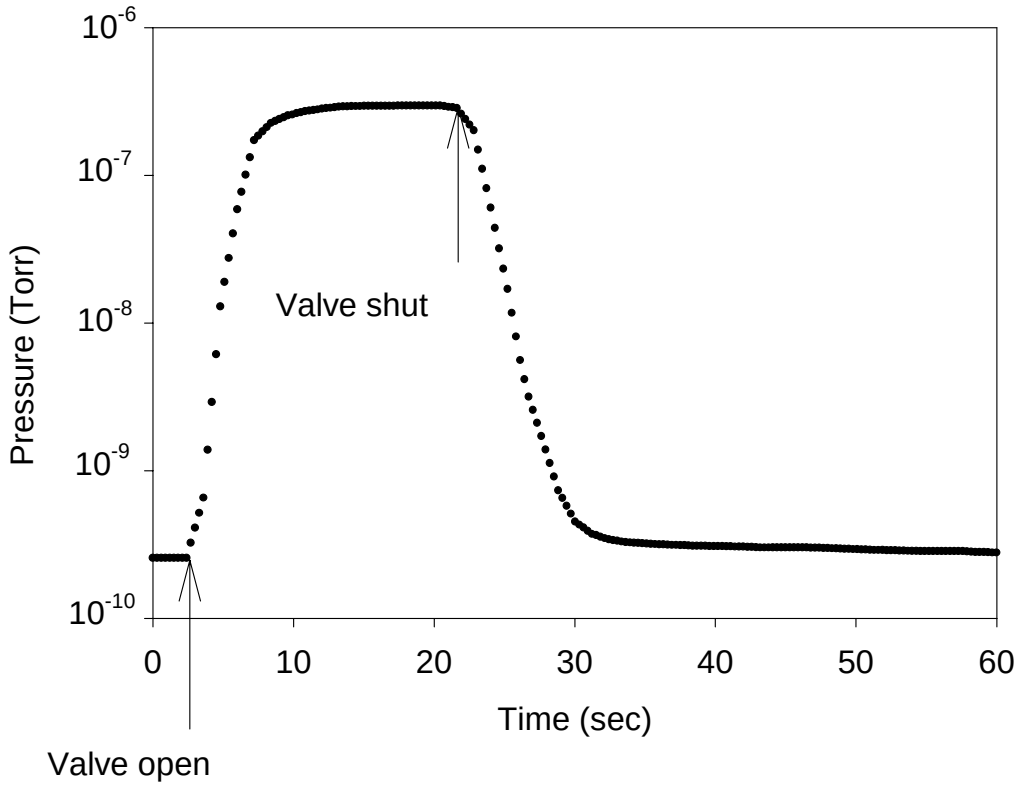

Figure 2.5: Buffer gas pressure in the third stage as the gas is cycled from its base pressure to its operating pressure and back to its base pressure. The pressure in the third stage can be decreased by three orders of magnitude in 10 s.

gen buffer gas can be quickly pumped. Figure 2.5 shows the pressure in the third stage of the accumulator as the buffer gas is cycled from its operating pressure of $\sim 3 \times 10^{-7}$ torr to its base pressure of $< 1 \times 10^{-9}$ torr in a few seconds. With the buffer gas pumped out the positron lifetime increases to 20 min, limited by impurities in the vacuum chamber. In the earlier accumulator a dewar filled with liquid nitrogen, which pumped out these impurities, surrounded a quadrupole Penning trap, and in this trap positron lifetimes of over 2 hours were possible. Currently we are constructing a high-field (5 tesla) positron storage stage, which will incorporate a 4 K cold trap around the electrode structure, with expected positron lifetimes of many hours to days (see Section 6.2.1).

When a large number of accumulated positrons are needed it is more efficient to operate the accumulator with a lower pressure in the third stage. Figure 2.6 shows the results of a computer particle code used to simulate the pressure profile throughout the accumulator [5] when it is optimized for a maximum number of trapped positrons. Operating under these conditions allows the trap to accumulate positrons for over 6 min, trapping approximately 3×10^8 positrons

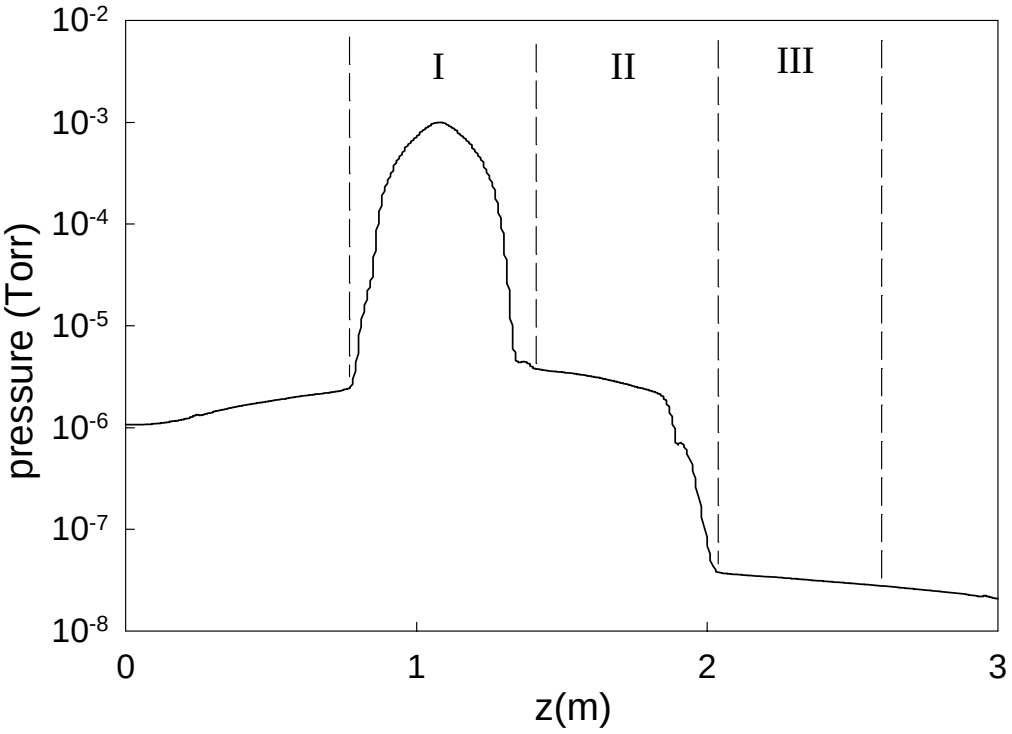

Figure 2.6: Calculated pressure profile as a function of distance along the three-stage positron accumulator. The pressure profile shown here is used to maximize the total number of positrons accumulated.

[37].

A schematic diagram of the accumulator and its surrounding vacuum vessel is shown in Fig. 2.7. The accumulator is contained in a UHV vacuum chamber, bakeable to 130° C, with a base pressure which has reached as low as 6×10^{-11} torr. Two cryo-pumps located at both ends of the accumulator are used to generate the differential pumping of the buffer gas and to quickly pump out the gas when needed. The simplified design of the new electrode structure allows a single magnet to surround the entire vessel (the earlier design had two magnets), which improves the uniformity of the magnetic field throughout the accumulator, and simplifies the magnet alignment procedure. The accumulator is typically operated with a magnetic field of 1500 G.

2.5 Retarding Potential Analyzer (RPA)

The positron and electron beam energy distributions are measured using a retarding potential analyzer (RPA). An RPA consists of an electrode at a potential of V_0 that rejects all particles with a parallel energy less than eV_0. The particles

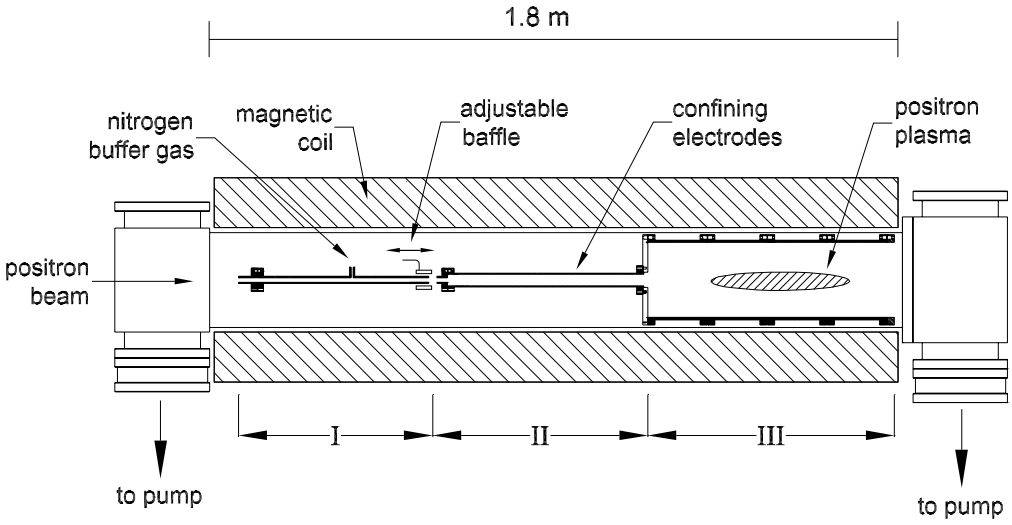

Figure 2.7: Schematic diagram showing the three-stage accumulator and surrounding vacuum chamber.

are guided magnetically through the RPA and those that are not rejected by the potential barrier are detected on the other side of the analyzer. The RPA electrode used in these experiments consists of a gold plated aluminum cylinder with a large length to diameter ratio. This insures that the potential in the center of the electrode is the same as the applied potential. Electrons are collected on an aluminum plate located beyond the RPA. A 3 kΩ shunt resistor is used in conjunction with a voltage amplifier to measure the beam current. Positrons are detected using a NaI(TI) γ-ray detector, which measures γ-rays emitted when a positron annihilates on the aluminum plate.

By measuring the number of particles that pass through the RPA as a function of applied potential, the parallel energy distribution of the beam can be measured. It is important to understand that only the particle velocity along the magnetic field, $v_{||}$, is affected by the RPA and therefore, only the parallel energy, $E_{||}$ is measured. Figure 2.8 shows the parallel energy distribution of a moderated positron beam measured using the RPA. The filled circles are the measured data. For applied voltages less than the beam energy (in this case 32 eV) all of the positrons pass through the RPA and are detected. When the applied voltage is above the beam energy none of the positrons are transmitted through the RPA. As the applied voltage on the RPA scans through the beam energy from low to high, the coldest positrons are rejected first, followed by positrons with larger parallel energies until all of the positrons are rejected. The open circles in Fig. 2.8 is the derivative of the data showing the FWHM of ~ 1 eV.

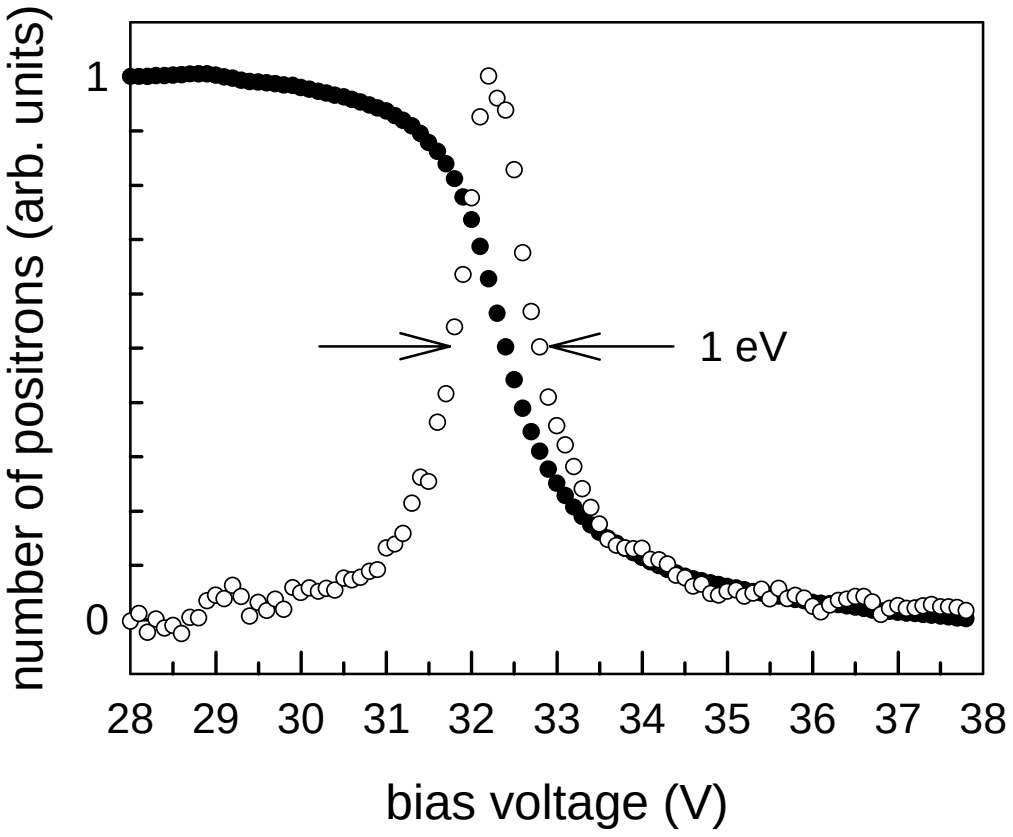

Figure 2.8: Energy distribution of a positron beam emitted from a neon moderator. Filled circles are measured data. The open circles, which represent the energy distribution, are calculated by taking the derivative of the data.

Chapter 3

Bright, Cold Charged Particle Beams

3.1 Introduction

This chapter describes a new and versatile method to create bright, cold positron and electron beams. The beams can be generated in either a quasi steady-state or pulsed mode. There are numerous potential applications for such bright beams. Examples include material surface characterization, such as defect depth profiling, positron and positronium scattering from atoms and molecules, and annihilation studies [37, 60, 78, 94]. Furthermore, many applications of positron beams, such as time-of-flight measurements, positron lifetime experiments, and time tagging, require pulses of positrons. One advantage of pulsed, as compared with steady-state beams, lies in the potential for greatly enhanced signal-to-noise ratios in a variety of applications. While several techniques to create pulsed positron beams have been discussed previously [18,81,105], many of these techniques have disadvantages. One example is achieving pulse compression at the expense of degradation in the beam energy spread.

There are several possible approaches to generate slow positron beams [88, 94]. The positrons originate from either a radioactive source or from a particle accelerator, but in either case they must be slowed from initial energies of several hundred keV to energies in the electron Volt range before beam formation and handling becomes practical. At present, this is accomplished most effectively using a solid-state moderating material (see Section 2.2). In general, positrons emerge from the moderator with an energy of several electron Volts and an energy spread in the range 0.3–2 eV, although methods have been described to reduce this energy spread by as much as an order of magnitude. [10, 25].

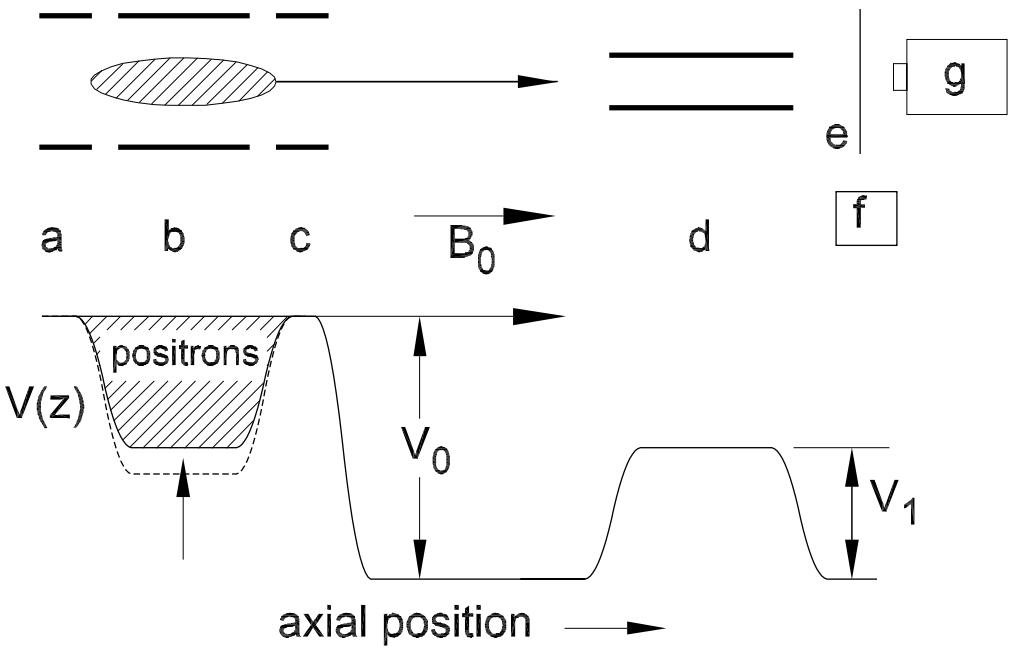

Figure 3.1: Schematic diagram of the experiment. The electrodes are shown schematically in the upper diagram. Below, the solid line represents the potentials applied to the electrodes: (a) entrance gate, (b) dump electrode, (c) exit gate, (d) RPA, (e) accelerating grids and phosphor screen, (f) NaI gamma-ray detector and (g) CCD camera. The energies eV_0 and eV_1 are the electrostatic potentials of the exit gate electrode and the energy analyzer, respectively.

3.2 Experimental Setup

The upper panel of Fig. 3.1 shows a schematic diagram of the apparatus to generate and analyze cold beams. Positrons or electrons are accumulated and cooled in the third stage of the three stage accumulator shown as electrodes ("a"), ("b") and ("c") in Fig. 3.1. The lower panel of Fig. 3.1 shows the potential profile of a confining well generated by the electrodes used to store the positron plasma. A cold positron beam is generated by reducing the size of the confining well, forcing the positrons over the exit gate electrode. To generate an electron plasma the same technique is used with the inverse potentials applied to all of the electrodes.

The radial density variations and temporal evolution of the beam profile are analyzed using a CCD camera, viewing a phosphor screen located behind the energy analyzer ("e" and "g" in Fig. 3.1). Particles are accelerated to 8 keV before being imaged on the screen. For positrons, a 3-inch NaI(Tl) γ-ray detector provides measurements of the particle flux. The electron flux is sufficiently large to be measured by a standard current-to-voltage amplifier connected to

a collection plate. The RPA labeled ("d") is used to determine the energy distribution of both the electron and positron beams. A detailed description of the positron accumulation techniques along with an explanation of the RPA can be found in Chapter 2.

3.3 Positron Beams

For the experiments described here, positrons were accumulated for 10 s, resulting in about 10^7 positrons in the trap. Because the fill time is much shorter than the 40-s positron lifetime, the loss of captured positrons during the filling phase is small. The positron beam is formed within a few milliseconds, so that in this mode of operation, the duty cycle for accumulation is close to unity. The average throughput is the same as the accumulation rate of about 1×10^6 positrons per second.

A pulsed positron beam is formed using the following procedure. After a positron plasma has been accumulated in the trap, incremental voltage steps are applied to the dump electrode (labeled "b" in Fig. 3.1), with each increase in voltage ejecting a fraction of the stored positrons. After each pulse the dump electrode is lowered, confining the plasma until the next pulse is formed. During this process, the entrance gate ("a") is placed 1 V above the exit gate ("c") to insure that the positrons leave the trap via the exit gate. The energy of the positron pulses is set by the potential of the exit gate electrode. In order to achieve a narrow energy spread, it is important that the steps in the dump voltage are small compared to the plasma space charge, otherwise collective modes can be excited in the charge cloud, which can, in turn, degrade the achievable energy resolution [24, 44]. Using the central electrode to dump small fractions of the plasma, the energy of the released positrons is kept the same for all pulses and is determined solely by the potential of the exit gate.

Figure 3.2(a) shows a pulse train obtained by applying equal-amplitude voltage steps to the dump electrode. For approximately the first 30% of the pulses in the train, the pulse height increases and then stays constant for the remainder of the pulses. The envelope of the pulse train is highly repeatable and unaffected by the number of pulses contained in it. In many cases it is advantageous to have equal-amplitude pulses throughout the pulse train.

By adjusting the size of the voltage steps in the following manner, it is possible to compensate for variations in pulse height and achieve a longer flat-topped region. The integrated charge dumped from the trap for a given pulse depends only on the dump voltage at the time of the pulse. Because the pulse-train envelope is highly reproducible, it can be used as an inverse look up table to determine the voltage steps needed to produce an arbitrary pulse envelope. The envelope of the pulse train produced with constant height steps in the dump voltage is shown in Fig. 3.2(a). The results of a wave form adjusted for a constant

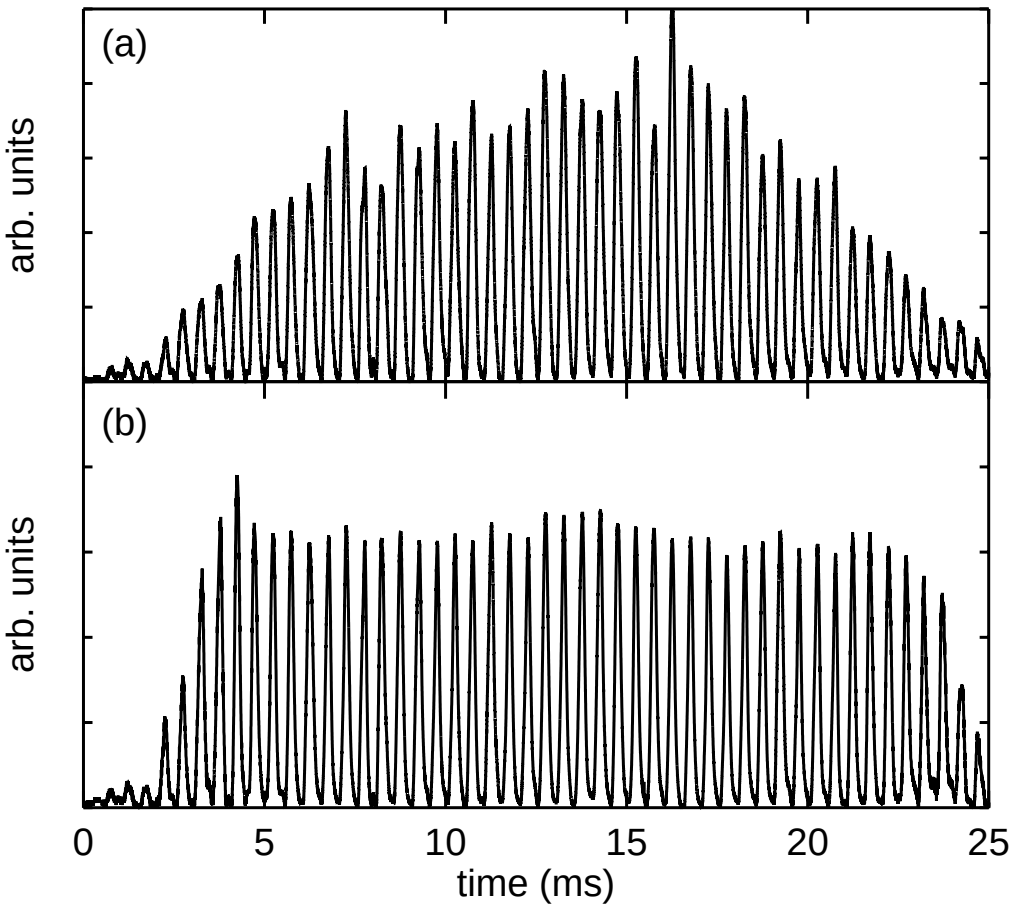

Figure 3.2: A pulse train of 60 pulses, each consisting of approximately 10^5 positrons, illustrating the ramp-up, flat-top and terminal phases of the pulse envelope, which is independent of the specific number of pulses: (a) corresponds to equal size steps in the dump voltage, whereas in (b) an adapted step size was used to correct for unequal pulse amplitudes.

pulse amplitude is shown in Fig. 3.2(b).

To insure that all particles with energies greater than the exit gate potential have sufficient time to leave the trap, we apply each voltage step for > 15 μs, which is longer than the axial bounce time in the trap ($\tau_b \approx 6\mu$s). Pulse durations less than τ_b can be produced by increasing the dump electrode potential for a time shorter than τ_b before returning it to a lower value. This latter protocol produces shorter pulses with a corresponding reduction in the number of positrons per pulse.

Using a CCD camera, we imaged the radial structure of the pulses, obtaining a size of about 2 cm (FWHM), roughly equal to the measured plasma size. This is representative of the first 75% of the pulse train. Thereafter, the profiles

broaden and become hollow for the last few pulses.

Positron beams with a well-defined energy are important for many applications. Room-temperature plasmas in the trap will equilibrate to an energy spread corresponding to $\frac{1}{2}kT$ per degree of freedom. We have shown that the perpendicular energy spread of the plasma is not affected by the dumping process and remains at the room temperature value [38].

In the regime where the steps in the potential of the dump electrode are small compared to the plasma space charge, the axial pulse energy spread is not affected significantly by the step size or the position of the pulse in the pulse train. Contributing factors to the axial energy spread include the radial variation of the exit gate potential across the plasma width, collective plasma effects [44], and electrical noise on the electrodes. Experimentally, we have shown that the axial energy spread varies little over pulses in a pulse train.

The axial energy distribution of a pulse taken at the beginning of the flat-topped portion of the pulse envelope is shown in Fig. 3.3. A description of the RPA operation is given in Section 2.5. The number of positrons which pass through the energy analyzer (c.f. Fig. 3.1) is plotted as a function of analyzer voltage, with the exit gate electrode set at 2 V and a step size of the dump electrode of 37 mV. An error function is fitted to the data and indicates a pulse centroid energy of 1.69 eV, with an energy spread of 0.018 eV FWHM. We attribute the difference of about 0.3 eV between the measured positron energy and the applied exit gate potential to a combination of contact potentials and the radial potential gradient in the trap. A lower limit of the beam energy is expected to be the axial temperature spread of the beam. The highest beam energy used in this experiment was 9 eV, but this was limited only by the maximum output voltage of the digital-to-analog voltage converters.

In practice, the pulse repetition frequency is limited at the lower end by the positron lifetime and at the high end by the positron bounce time. Pulse amplitudes will be inversely proportional to the number of pulses in the pulse train. However, if small energy spreads are desired, it is necessary to operate in the limit where each step in dump voltage is small compared to the plasma space charge.

We have also created quasi steady-state positron beams of 0.5 s duration with a current of 0.8 pA. This was done by raising the dump voltage continuously on a time scale much longer than the particle bounce time. The beam energy spread in this case was 0.017 eV FWHM, which is comparable to that of the pulsed positron beam.

We are aware of one other report of a Penning trap used as a pulsed source of positrons [95]. Positrons from a LINAC, were captured in a Penning trap and then extracted by applying voltage pulses to the exit gate. However, in this case, no attempt was made to achieve a well defined beam energy or narrow energy spread.

Brightness is an important figure of merit for beam sources. Use of the

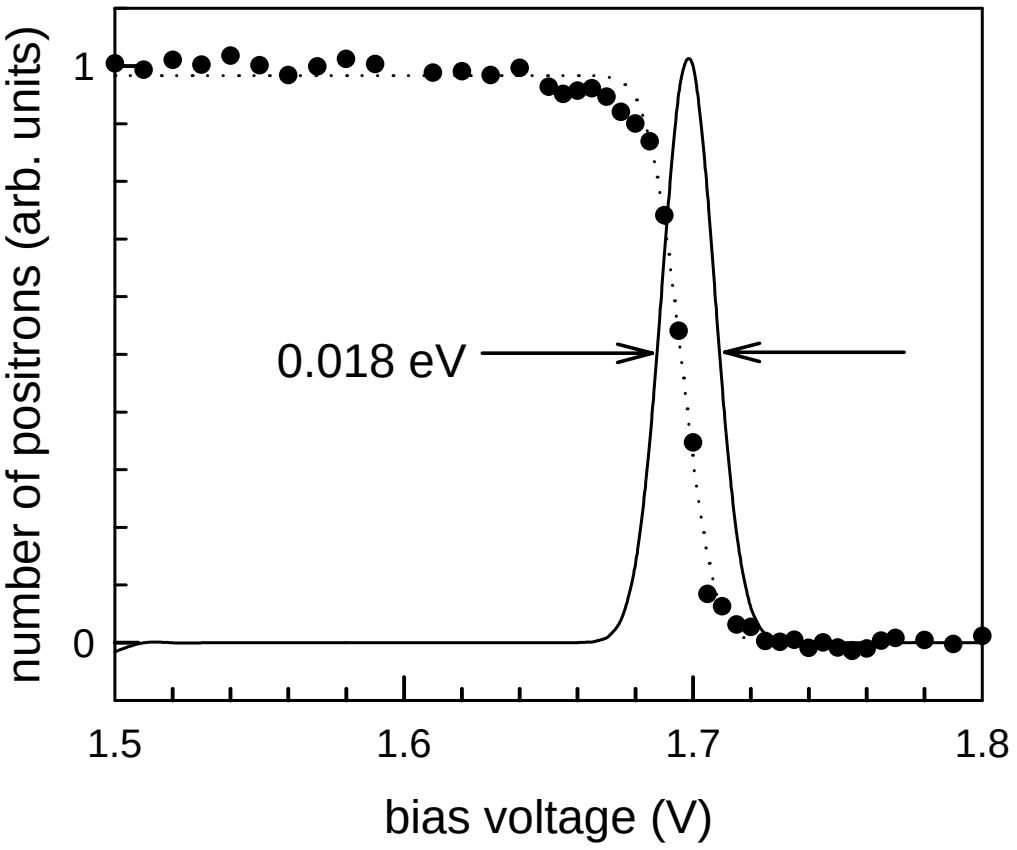

Figure 3.3: Energy distribution of a pulse. Filled circles are measured data, and the dashed line is an error function fit to the data. The solid line, which represents the energy distribution, is the derivative of the fit.

positron trap and a buffer gas to cool the positrons increases their phase space density, and hence the beam brightness, without significant loss of beam intensity. The brightness of our pulsed positron beam is 1×10^9 s^{-1} rad^{-2} mm^2 eV^{-1}, which is significantly higher than the brightness reported for a steady state positron beam with two remoderation stages [94]. In principle, compressing the stored plasma radially by applying an azimuthally rotating electric field to segmented electrodes surrounding the plasma or using a source of positrons at cryogenic temperatures could enhance the brightness even further (see Section 6.2.1).

3.4 Electron Beams

A conventional hot-cathode electron gun produces electron beams with an energy spread typically corresponding to several times the cathode temperature (≈ 0.5 eV). Electron guns optimized for low energy spreads ($\Delta E \approx 0.2$ eV at a current of several microamps) have been described (e.g., Ref. [58]). However, their operation in a magnetic field has not been tested, and the design described in Ref. [58] cannot be used in a magnetic field without modifications. The energy resolution of an electron beam can be improved by energy filters of various designs, such as $E \times B$ filters, spherical deflectors, etc. A general discussion of electron monochromator designs in non-magnetized beams shows that 0.3 μA of beam current presents an upper limit, if the energy uncertainty is to remain below 0.1 eV [67].

There are other processes which can produce electrons of well defined energies. For example, a synchrotron photo-ionization technique has been described, capable of producing electron beams with an energy uncertainty of about 3.5 meV. However, the achievable beam currents are low (of the order of 10^{-12} A) and the processes requires a source of synchrotron radiation.

We have shown that it is possible to generate well defined, accurately controllable, and cold steady-state or pulsed electron beams, by extracting electrons from a stored plasma, in a manner similar to that described above for positrons. For example, an electron beam of 0.1 μA lasting 4.8 ms can be extracted from a reservoir of 3×10^9 cold electrons (i.e. 4.8×10^{-10} Coulombs).

For the electron experiments, we use a commercial dispenser-type cathode with a 2.9 mm aperture as an electron source to fill the Penning trap. The cathode heater current is set so that an extraction voltage of 0.5 V applied to a grid in front of the cathode results in an emission current of about 2 μA. The simplest method for filling the trap with electrons is to raise a potential barrier around the trap while the electron source is on (see Section 2.4). This method cannot be used here because the beam currents attained from the hot-cathode source are insufficient to generate the needed electron densities. Instead the following trapping technique was used.

Filling the trap with electrons was achieved without the use of a buffer gas by creating a confining well of gradually increasing depth, so that an approximately constant trapping potential is maintained. The final well depth of 90 V is reached in 100 steps in a total time of about 1 s. The resulting electron plasma, which cools to room temperature by collisions with a neutral background gas [66], contains 3×10^9 particles and has a space charge of 90 V. Using a nitrogen buffer gas while accumulating the electrons does increase the trapping efficiency. Unfortunately, this also greatly accelerates the radial transport, resulting in an increased electron beam diameter, which needs to be small for many applications.

After an electron plasma has been accumulated in the trap, a cold beam is generated by continuously reducing the depth of potential well confining the

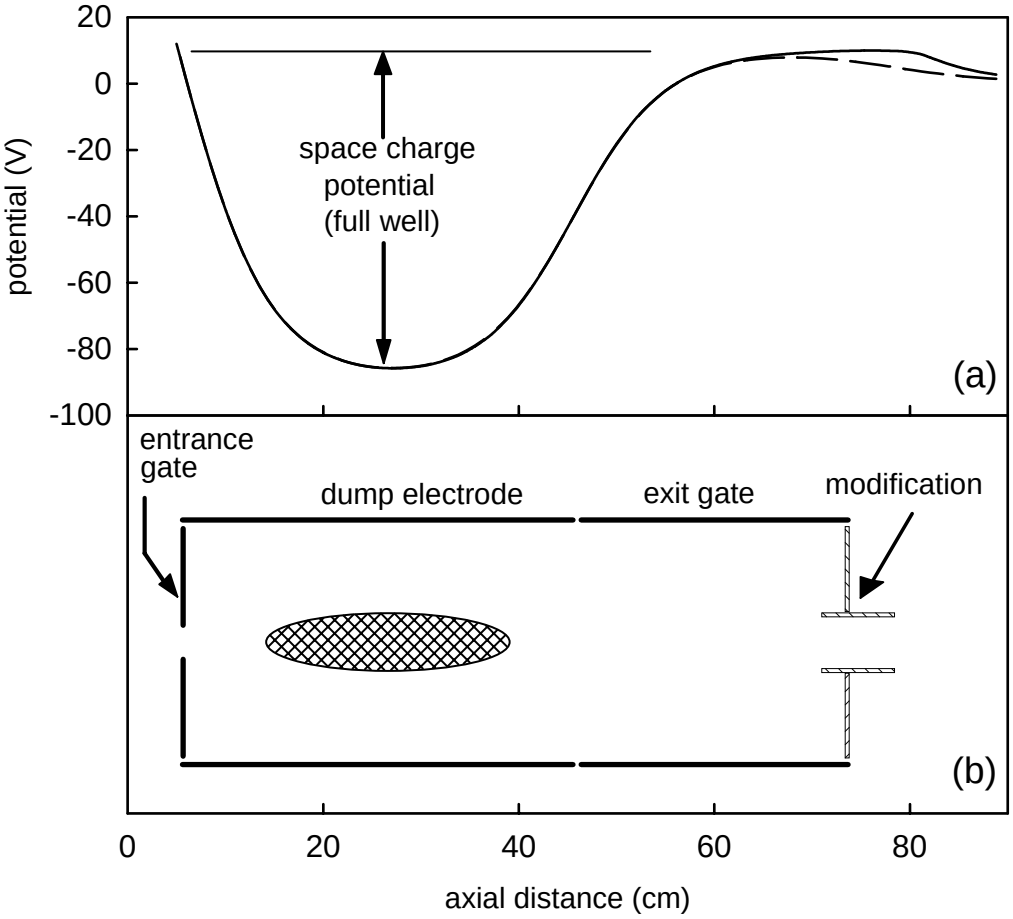

Figure 3.4: (a) The axial potential distribution in the empty trap. (b) A schematic drawing of the electrode configuration. An electrode added into the electrode structure (shown in hash) gives rise to the potential depicted by the solid line. The dashed line was calculated without the modified electrode in place. The approximate position of the electron plasma is shown in (b).

electrons. As the magnitude of the potential well decreases, the electrons are forced over the exit-gate electrode, which sets the electron beam energy. The entrance-gate electrode is set 1 volt below the exit-gate electrode to insure that the electrons leave via the exit-gate electrode.

The large number of electrons in the trap (3×10^9, as compared to 10^7 positrons) creates a space charge, which can distort the potential near the exit gate electrode and lead to large uncertainties in the resulting beam energy. The modified exit gate electrode design shown in Fig. 3.4 increases the separation between the charge cloud and the exit gate and thereby decouples the extracted

beam energy from the number of particles stored in the trap. A self-consistent Poisson-Boltzmann calculation, which includes the modified electrode geometry in the presence of the electron plasma, confirmed that the plasma potential has a negligible effect on the resulting beam energy.

The energy distribution of the beam is measured using an RPA (see Section 2.5). Electrons which pass through the RPA are collected on an aluminum plate and recorded on a digital oscilloscope. The plate is biased slightly positively ($\sim$ 2 V) to insure that all of the electrons are collected. A potential bias much larger than this is avoided, since it can cause secondary electron emission from the aluminum plate, which leads to an apparent increase in the beam current. Care must be taken while measuring the energy distribution of the electron beam in a magnetic environment. In particular, when the beam is partially reflected by the analyzer electrode, the reflected particles interact with the incident beam, causing a space charge to build up. This increased space charge can force electrons through the RPA, which appears as an increase in the energy spread of the beam. To minimize this effect, the retarding energy analyzer is raised for only a short time ($\sim$ 10 μs) and then lowered to release any charge build up.

The axial energy distribution for an 0.1 μA electron beam was measured in this manner (c.f. Fig. 3.5) and indicates an energy spread of 0.10 eV FWHM. Both experiment and potential calculation using a Poisson-Boltzmann solver (c.f. Fig. 3.4) confirm that the absolute beam energy is set accurately by the externally applied exit gate potential. Larger beam currents have also been generated and show a corresponding increase in the axial energy spread, which is believed to be at least in part due to the increased space charge of the beam. For example, a 1 μA electron beam has an energy spread of approximately 0.5 eV. It should also be possible using the technique described here to generate an electron beam with an energy spread as low as that of the positron beam (0.018 eV). In this case the achievable beam currents would be comparable to those used in the positron beam ($\sim$ 1 pA). Unfortunately, our present measuring technique is unable to detect a current this small. Future plans to install a microchannel plate in the experiment will allow us to explore the possibility of studying these low-energy electron beams.

As with positrons, having the ability to generate an electron beam with a fast rise time and constant current thereafter is often advantageous (see Chapter 5 for an example). This can be accomplished by modifying the dump waveform in the following manner. The total charge dumped from the well at any given time during the beam extraction depends only on the dump voltage at that time. Therefore, the time-integrated current (i.e. total charge) resulting from a beam dump using a linear ramp can be used as an inverse lookup table to find the dump voltage required to achieve an arbitrary current waveform. The current waveform produced by dumping the electrons using a simple linear ramp is shown in Fig. 3.6(a), and has a rather slow current rise of over 1 ms. By using this waveform as an inverse lookup table an electron beam with an arbitrary

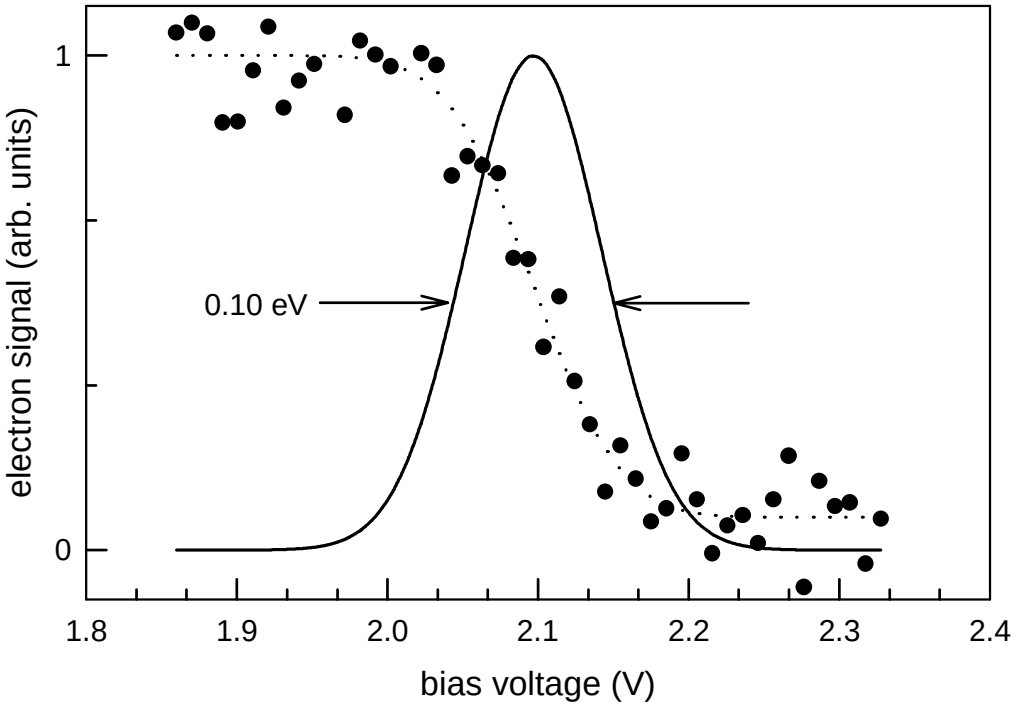

Figure 3.5: Energy distribution of a 0.1 μA quasi steady-state electron beam. Filled circles are measured data, and the dotted line is an error function fit to the data. The solid line, which represents the energy distribution, is the derivative of the fit.

waveform can be generated. Figure 3.6(b) shows a beam current generated using this technique to produce a quick current rise ($t_r \sim 3$ μs) and $\sim$ 0.08 μA current thereafter.

3.5 Chapter Summary

We have shown that room-temperature plasmas stored in Penning traps can be used as versatile sources of pulsed and steady-state beams of positrons and electrons. In the case of positrons, we measured an energy spread of 0.018 eV for both pulsed and quasi steady-state beams. Electron beams were extracted from a plasma of 3×10^9 particles. At a current of 0.1 μA, beams lasting 5 ms can be formed with an energy spread of 0.10 eV (FWHM). It is likely that the performance of these cold, bright, electron and positron beam sources can be further improved by relatively straight forward modifications of the techniques described above.

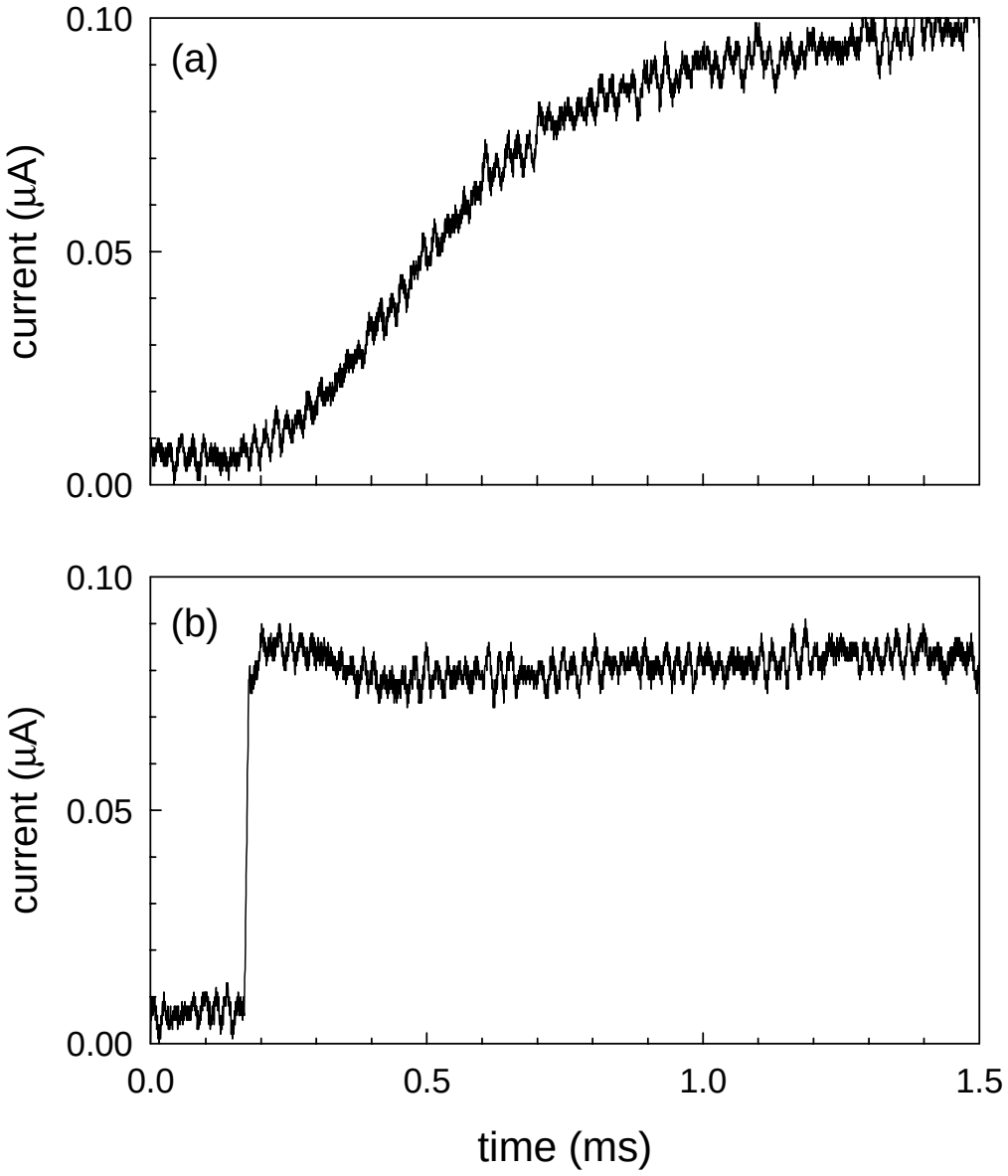

Figure 3.6: (a) Current waveform of an electron beam obtained using a linear voltage ramp to dump the plasma. (b) Current waveform using an optimized dump voltage waveform to dump the plasma. Note the much faster turn-on ($\approx 3\ \mu$s) and the extended region of constant current.

Chapter 4

Positron Scattering from Atoms and Molecules

4.1 Introduction

The interaction of antimatter with matter is an interesting and active field of study [39, 43, 47, 53, 54, 60, 62, 68, 79, 89, 94, 100, 114]. One of the simplest of these types of interactions is that between a positron and an atom or molecule. Such interactions are important in atomic physics [39, 43, 53, 54, 60, 62, 68, 100, 114] and surface science [46, 94], and they have potential technological applications such as mass spectrometry [47, 89]. Although some aspects of these interactions have been studied in detail [12, 54, 60, 114], most positron scattering experiments to date have been limited to positron energies greater than 1 eV due to technical limitations. For example, before the work described here, the lowest energy positron differential cross-section $d\sigma/d\Omega$ (DCS) measurements were from argon at 2.2 eV [16], and the only known positron total vibrational excitation cross sections were for CO_2 at energies above 2 eV [62]. The only exceptions to this are total cross sections which have been measured at energies below 1 eV [43, 60, 100]. There are, however, many interesting questions at low values of positron energy, including the existence of positron bound states with atoms or molecules [91], the role of vibrational excitation in the formation of long lived positron-molecule resonances [39, 53], and understanding the fragmentation of large-molecules stimulated by positrons [47, 89].

To form a cold positron beam, the limited supply of positrons must be used efficiently. Until now, most positron scattering experiments have used moderated beams of the form discussed in Section 2.2 as a cold positron source, limiting the experiments to energies greater than about 1 eV [43, 60, 62, 68, 100, 114]. In Section 2.4, we describe a novel technique that we developed to overcome these limitations to achieve a high intensity, cold, magnetized positron beam (i.e., 18 meV FWHM) [32, 65]. Using the cold beam, we were able to make new kinds

of positron scattering measurements. These include measuring positron-argon and positron-krypton DCS at energies lower than any previous measurements (0.7–2.0 eV), and making the first low-energy measurement of positron-molecule total vibrational cross sections at energies as low as 0.2 eV, studying the υ_3 excitation of CF_4 [31].

Aside from some total cross section measurements [43,60,100], positron scattering experiments have been traditionally carried out using moderated positrons in an *electrostatic* beam. The positrons are focused onto a highly compact target such as a gas jet, which defines the scattering angle precisely. Typically, a channeltron detector with a retarding potential grid in front of it is placed on a movable arm to measure the DCS [49]. Because our cold positron beam is formed in a magnetic field, it is expedient for us to conduct the positron scattering experiments in a field of comparable magnitude. This led us to combine existing techniques and develop new ones in order to perform measurements such as elastic DCS, total inelastic cross sections, and total cross sections for positrons scattering in a magnetic field.

Many of the techniques described in this chapter have been used elsewhere in one form or another. For example, positron-atom total cross sections are typically measured using a gas cell and a positron beam which is guided through the cell by a weak magnetic field [43,60,100]. RPA measurements have been used previously in conjunction with a spatially varying magnetic field to characterize the energy distributions of moderated positrons [41]. Positron-atom DCS have been measured in a magnetic field using time of flight methods [16]. Magnetized pulsed beams have been created using a non-thermal reservoir of positrons [61,95, 105]. In addition to combining these techniques in a unique fashion, the ability to resolve inelastic from elastic scattering events using a varying magnetic field between the scattering and analysis regions [see Section 4.3.2], and the use of an N_2 buffer gas and three-stage Penning trap to from a cold pulsed or continuous beam [32, 65, 104] are new developments in the field of positron atomic and molecular physics. By combining the cold positron beam formed in this manner with methods to perform scattering experiments in a magnetic field, we have been able to extend the limits of positron-atom and positron-molecule scattering experiments into a new range of positron energies.

Using the information gained from initial experiments performed on our earlier apparatus, a new scattering apparatus was constructed to be used in conjunction with the new positron accumulator (see Section 2.4) [103]. Initial work using the new accumulator and scattering apparatus has improved our capability to study low-energy positron physics, because of the brighter positron beam and increased positron throughput. The new scattering apparatus also has the capability to operate at a magnetic field ratio four times greater than that previously possible. As discussed, this provides correspondingly greater discrimination for inelastic scattering studies. These improvements lead to increased signal-to-noise ratio and improved energy resolution. The initial results from the new appa-

ratus are promising. The studies described here are the beginning of a broad experimental program in low energy positron atomic physics.

This chapter is organized in the following manner. First, scattering from atoms and molecules in a magnetic field is described, followed by a discussion of the methods used to measure differential elastic, inelastic, and total cross sections. Measurements of elastic positron DCS on argon and krypton, and inelastic vibrational cross sections for CF_4, are then summarized. The chapter continues with a discussion of other effects relevant to this kind of measurement, and concludes with a set of remarks emphasizing the future of experiments in this area of low-energy positron atomic physics.

4.2 Experimental Setup

The scattering experiments are conducted in the following manner. First, positrons are accumulated for ~ 0.1 s and then cooled to room temperature in ~ 1 s. A cold beam of approximately 10^5 positrons is formed using the technique described in Section 3.3. It is guided magnetically through the scattering cell where it interacts with the test gas. The parallel energy distribution of the scattered beam is then measured with an RPA and analyzed using the techniques described in Section 4.3. In order to improve the statistics, the entire 2 second sequence is typically repeated 1000 times, and so a typical data run takes 11 hours to complete. A schematic diagram of the scattering experiment is displayed in Fig. 4.1(a), showing the third stage of the positron accumulator, the scattering cell and the RPA. The scattering apparatus is located in a UHV vacuum chamber which attaches to the end of the three stage accumulator. Two 60 cm magnets are used to generate a uniform field through the scattering cell and RPA.

Test gas is continually introduced into the center of the scattering cell, which is 38 cm long with a 1 cm internal diameter, and is pumped out at both ends using two cryo-pumps [see Fig. 4.1(a)]. A well localized region of higher gas pressure is created by differential pumping between the 1 cm diameter scattering cell and the 9 cm diameter vacuum chamber. Figure 4.1(b) shows the calculated pressure profile of the test gas in the scattering apparatus. A typical gas pressure of 0.5 mtorr in the center of the gas cell is reduced by over two orders of magnitude by the ends of the cell. This permits operation of the experiment in steady-state with the test gas isolated in the scattering cell and the nitrogen buffer gas confined to the accumulator. In our previous scattering apparatus it was necessary to pump out the nitrogen buffer gas before the test gas could be introduced. By eliminating this complication we have been able to increase the positron throughput by an order of magnitude.

To further reduce the effects of the test gas on the accumulator fill cycle, a 1.2 cm diameter gas baffle was placed between the scattering cell and accumulator [see Fig. 4.1]. In order to reduce the effects of multiple scattering, the

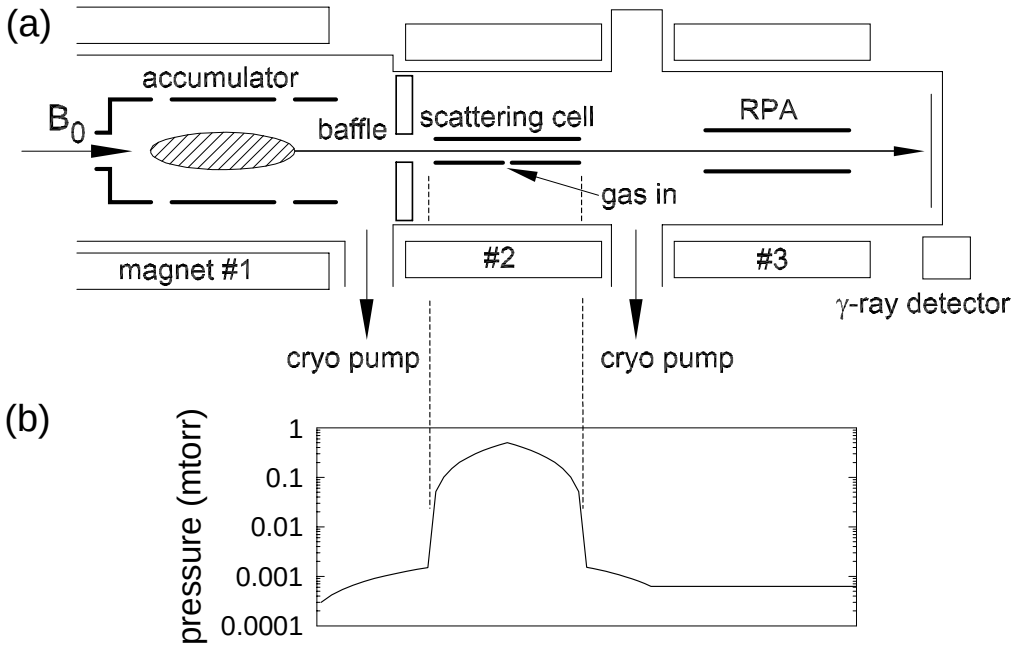

Figure 4.1: (a) Schematic diagram of the scattering apparatus showing the third stage of the positron accumulator, the scattering cell and the RPA, which are located in a UHV chamber. Magnetic coils labeled 1 through 3 are used to generate a uniform magnetic field through the accumulator, scattering cell, and RPA, respectively. (b) Calculated test-gas pressure profile along the axis of the scattering apparatus. The gas pressure near the ends of the scattering cell is more than two orders of magnitude smaller than at the center.

test gas pressure in the scattering cell is adjusted so that 10% of the positron beam is scattered by the gas. We are able to determine the average absolute pressure in the scattering cell, with better than 1% absolute accuracy, using a thermally regulated capacitance manometer gauge, which directly measures the pressure at the center of the scattering cell. Because capacitance manometers use a direct pressure measurement (unlike an ion gauge), the pressure reading is independent of the specific test gas being studied. We verify for the atoms and molecules studied that the operating pressures used in the scattering cell (typically 0.1 to 1 mtorr) are in a pressure regime where the measured scattering cross sections are independent of the test gas pressure.

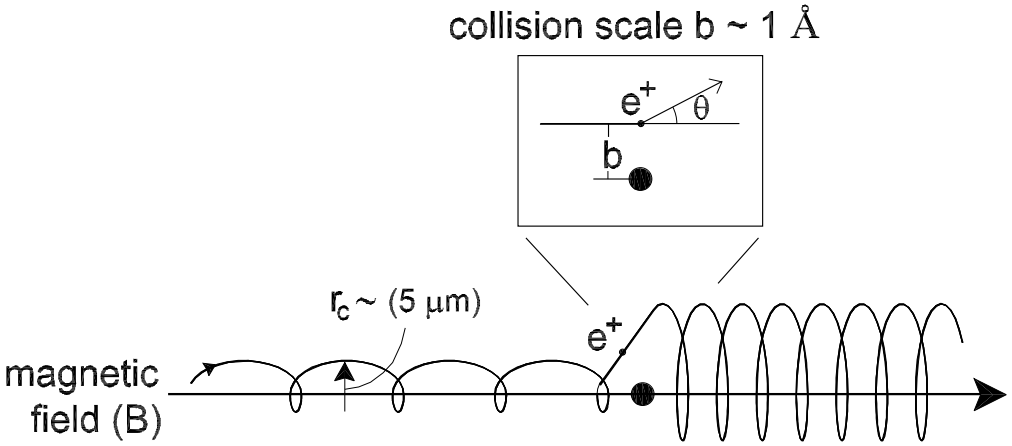

Figure 4.2: Positron scattering in a magnetic field. A positron from a cold beam, with most of its kinetic energy in the parallel component, $E_{\|}$, follows magnetic field until it scatters from an atom [see inset]. The scattering event transfers some total energy, E, of the positron from $E_{\|}$ into $E_{\perp}$, depending on the scattering angle and atomic processes involved. The scattered positron continues along the field with an increased value of $E_{\perp}$ and decreased $E_{\|}$.

4.3 Data Analysis

The scattering measurements presented here exploit the behavior of positrons in a 0.1 tesla magnetic field. As mentioned in Section 2.1, the total positron energy, E, can be expressed as $E = E_{\perp} + E_{\|}$, where $E_{\perp}$ and $E_{\|}$ are the contributions to the motion perpendicular and parallel to the magnetic field. Figure 4.2 depicts a positron scattering from an atom or molecule in a magnetic field. The positron follows a helical path along the magnetic field with a small (5 μm radius) cyclotron orbit. Upon colliding with a test gas atom, the positron scatters at an angle θ, transferring some of its kinetic energy (which is initially in the parallel component, $E_{\|}$) into the perpendicular component, $E_{\perp}$. The interaction occurs on an atomic length scale (i.e., $b \sim 1$ Å). Since b is orders of magnitude smaller than the radius of curvature of the positrons in the magnetic field, the positron scatters as if it were in a field-free region. After the scattering event, the positron continues to be guided by the magnetic field, with some of its total energy E transferred to the test atom and some into $E_{\perp}$, depending on the angle scattered and the elastic or inelastic nature of the scattering event.

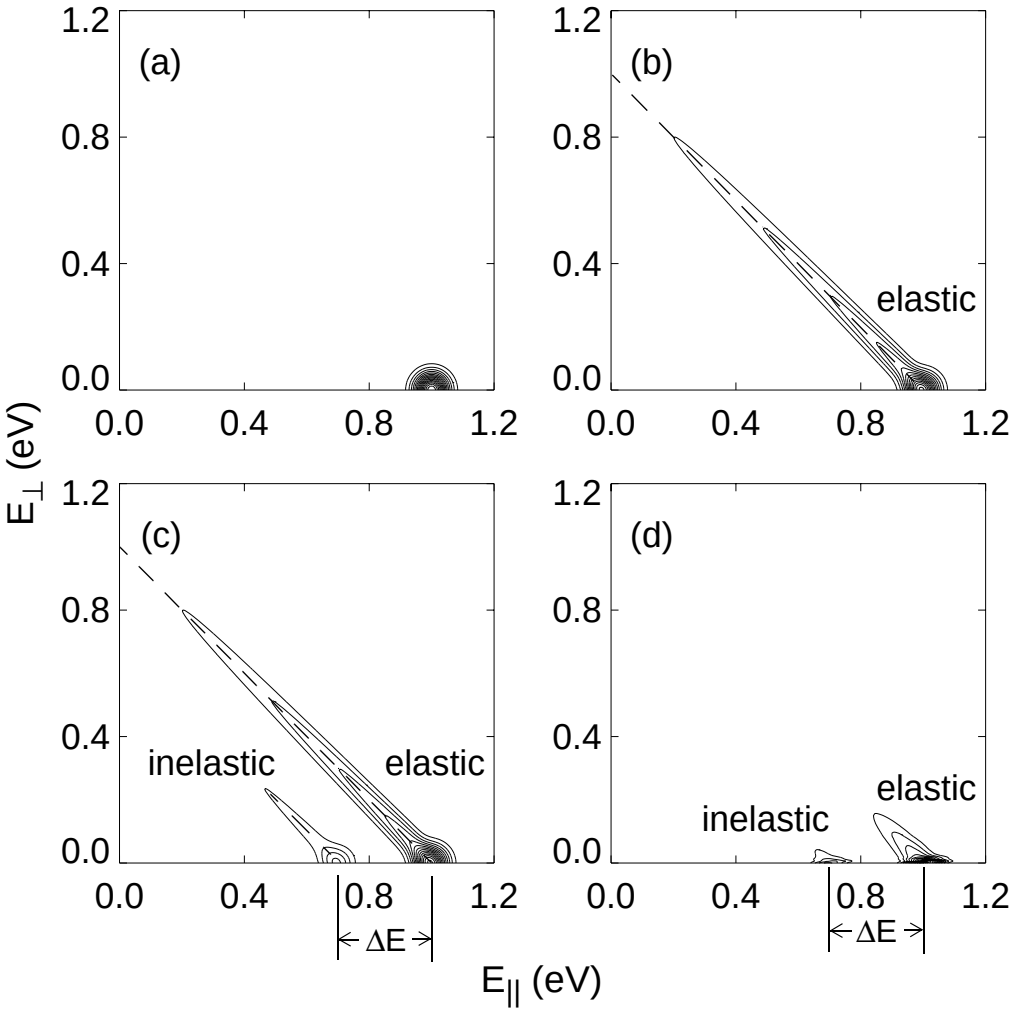

Figure 4.3: Simulated effects of elastic and inelastic scattering on the parallel and perpendicular energy components of an initially strongly magnetized, cold 1 eV charged particle beam: (a) incident beam; (b) the effect of elastic scattering; (c) both elastic and inelastic scattering; and (d) the scattered beam shown in (c), following an adiabatic reduction of the magnetic field by a factor of $M = 10$. The dashed lines show the conservation of total energy as the positrons scatter through angle θ. The total energy loss from a simulated inelastic collision is indicated by the shift $\Delta E = 0.16$ eV.

4.3.1 Elastic DCS Analysis

In cases where only elastic scattering is present (i.e., noble gases below the threshold for electronic excitation and positronium formation), we can extract

the DCS from the parallel energy distribution of the scattered beam. Figure 4.3 shows a calculated energy distribution in ($E_\perp$, $E_\parallel$) space for a cold 1 eV beam (a) before, and (b) after an elastic scattering event. Because the collision is elastic, the total positron energy E is conserved [Fig. 4.3(b) dashed line]; therefore the scattering angle θ is determined solely by the amount of energy transferred from $E_\parallel$ to $E_\perp$. If we assume that the initial trajectory of the positron is in the direction of the magnetic field, then after an elastic scattering event, the positron velocity, $v_\parallel$ in the direction of the field will be $v_\parallel = v\cos(\theta)$, where v is the total velocity of the positron, $v_\parallel$ is the velocity along the magnetic field, and θ is the scattering angle. Thus, $E_\parallel = E\cos^2(\theta)$, which can be rewritten as:

$$\theta = \cos^{-1}\sqrt{E_\parallel/E}. \tag{4.1}$$

The assumption that the incoming positron trajectory is in the direction of the magnetic field is valid for $E_\parallel \gg E_\perp$. Typically a positron will have $E_\parallel \sim 1$ eV and $E_\perp \sim 0.025$ eV. This means that the positrons have an initial angular spread [$\Delta\theta = \sin^{-1}(v_\perp/v)$] of $\sim 9°$, which provides an estimate of our angular resolution.

In order to calculate the DCS, we need to know not only to which angle a given $E_\parallel$ corresponds, but also how many positrons are scattered into that angle. For a given applied voltage V_0, the RPA discriminates against all particles with parallel energy components $E_\parallel$ less than eV_0, and so the RPA measures the parallel energy distribution integrated over energies above $E_\parallel$. Therefore the integrated parallel energy distribution normalized to unity $I(E_\parallel)$ measures the probability for a positron to have a parallel energy greater than or equal to $E_\parallel$. Using this integrated energy distribution, the elastic DCS is obtained by

$$\frac{d\sigma}{d\Omega} = C\left(\frac{dE_\parallel}{d\Omega}\right)\left(\frac{dI(E_\parallel)}{dE_\parallel}\right), \tag{4.2}$$

where the constant of proportionality, C, relates the scattering cross-section to the scattering probability, $dE_\parallel/d\Omega$ represents the relation between the effective solid angle sampled and the energy increments used in the RPA measurement, and $dI(E_\parallel)/dE_\parallel$ is the probability that a positron will be scattered into the energy range $dE_\parallel$. The constant C is given by

$$C = \frac{\sigma}{P_s} = \frac{1}{nl}, \tag{4.3}$$

where σ is the cross section, P_s is the probability of a scattering event, n is the number density of the test gas molecules, and l is the positron path length through the scattering cell. For the experiment described here,

$$C(a_0^2) = 0.029/P_{av}(\text{torr}), \tag{4.4}$$

where P_{av} is the average pressure. We have assumed a scattering cell temperature of 20° C and a path length equal to the scattering cell length of 38 cm. The quantity $dE_{\|}/d\Omega$ in Eq. (4.2) can be calculated using Eq. (4.1) to yield:

$$\frac{dE_{\|}}{d\Omega} = -\frac{1}{\pi}\sqrt{EE_{\|}}. \tag{4.5}$$

Substituting Eq. (4.5) into Eq. (4.2), we obtain a final relationship between the RPA data $I(E_{\|})$ and the DCS for the elastic scattering event:

$$\frac{d\sigma}{d\Omega} = C'\sqrt{\mathrm{EE_{\|}}}\left(\frac{\mathrm{dI(E_{\|})}}{\mathrm{dE_{\|}}}\right), \tag{4.6}$$

where $C' = -\ \mathrm{C}/\pi$. Using Eqs. (4.1) and (4.6) we can determine the DCS for a positron-atomic or positron-molecular elastic scattering event given the parallel energy distribution of the scattered beam.

4.3.2 Measurement of Total Inelastic Cross Sections

We are also able to measure total inelastic cross sections for positron-atom or positron-molecule scattering. Figure 4.3(c) shows the simulated effects on $E_{\perp}$ and $E_{\|}$ of both elastic and inelastic scattering from a positron beam. The positrons that participate in an inelastic scattering event lose some energy ΔE, transferring it to the atom or molecule, and are represented by the shifted beam in Fig. 4.3(c). In order to measure the total inelastic cross section, we must be able to distinguish between an inelastically scattered positron that has lost ΔE to the target atom and an elastically scattered positron whose scattering angle corresponds to a loss of ΔE in its parallel energy component. It is clear from Fig. 4.3(c) that by simply measuring the parallel energy distribution of the scattered beam we cannot distinguish between these two events. To circumvent this problem, we take advantage of the adiabatic invariant $E_{\perp}/B$, discussed in Section 2.1, for a charged particle in a slowly varying magnetic field of strength B. If the positron scatters in a magnetic field B_s and is guided adiabatically into a lower field B_a, where it is analyzed (see Fig. 4.1 magnets #2 and #3, respectively), then $E_{\perp}$ is reduced by the ratio of the large field to the small field, $M = B_s/B_a$, while the total energy of the positron is still conserved. For a large reduction in the field ($M \gg 1$), the resulting parallel energy $E_{\|}$ is approximately equal to the total energy E. Figure 4.3(d) shows the scattered beam after it has undergone a reduction $M = 10$ in magnetic field. It is clear from this figure that the parallel energy distributions of the elastic and inelastic scattering events are now well separated, and therefore they can be discriminated by the RPA.

4.3.3 Total Cross Sections

Although we have not yet published any data on positron total scattering cross sections, such measurements are done routinely using magnetized positron beams

[43, 60, 100] and are, in principle, easy to do with the system described here. The probability for a positron to undergo any scattering event (which is proportional to the total scattering probability) can be measured in two steps. First the RPA is set to 0 V, and the total beam strength is measured. Then the unscattered beam strength is measured by adjusting the RPA voltage a small increment, ΔV, below the beam energy. The analyzer rejects all positrons which have either undergone an inelastic scatter with energy loss greater than $e\Delta V$ or have transferred parallel energy greater than $e\Delta V$ into perpendicular energy by elastic scattering, thus discriminating against all scattered positrons. The total scattering cross section is determined by comparing this signal to the total beam strength and scaling it by the constant of proportionality C, derived in Eq. (4.4), which relates the TCS to the scattering probability. By repeating this at different values of beam energy, the total cross section as a function of beam energy can be determined for a given atomic or molecular species.

4.4 Experimental Results

4.4.1 Differential Cross Sections

Using the method described in Section 4.3.1, we have been able to make DCS measurements for both Ar and Kr at energies ranging from 0.4 to 2.0 eV [31]. The data presented here is the first experimental study of low-energy elastic scattering of positrons from noble gases. DCS measurements are important because they offer a strict test of theoretical models, which in turn test our understanding of the processes governing positron scattering. These processes differ greatly from their electron scattering counterparts. For example, in low-energy positron-atomic elastic scattering, the two dominant long range interactions (static and polarization), which are additive in the electron scattering case, tend to cancel for positron scattering. Virtual positronium formation is also believed to play an important role in positron-atom elastic scattering, and of course this process is not available in the electron case [23].

The DCS data presented here were taken using our earlier accumulator, which was not optimized for such measurements. Although the experimental setup and operation are similar to that described in Section 4.2, the details of the experiment are quite different and are described elsewhere [31]. Figure 4.4 shows the raw data, taken on the new scattering apparatus designed specifically for such experiments. The data are normalized to unity for a 1 eV positron beam scattered from argon atoms. The open circles are the positron beam data with no argon gas present. The closed circles are the scattered positron beam where the pressure in the gas cell has been adjusted for approximately 10% total scattering. Because the positron beam energy (1 eV) is below all inelastic processes, such as positronium formation and electronic excitation, the scattering is purely elastic. The bottom axis of Fig. 4.4 shows the applied voltage on the RPA. The upper

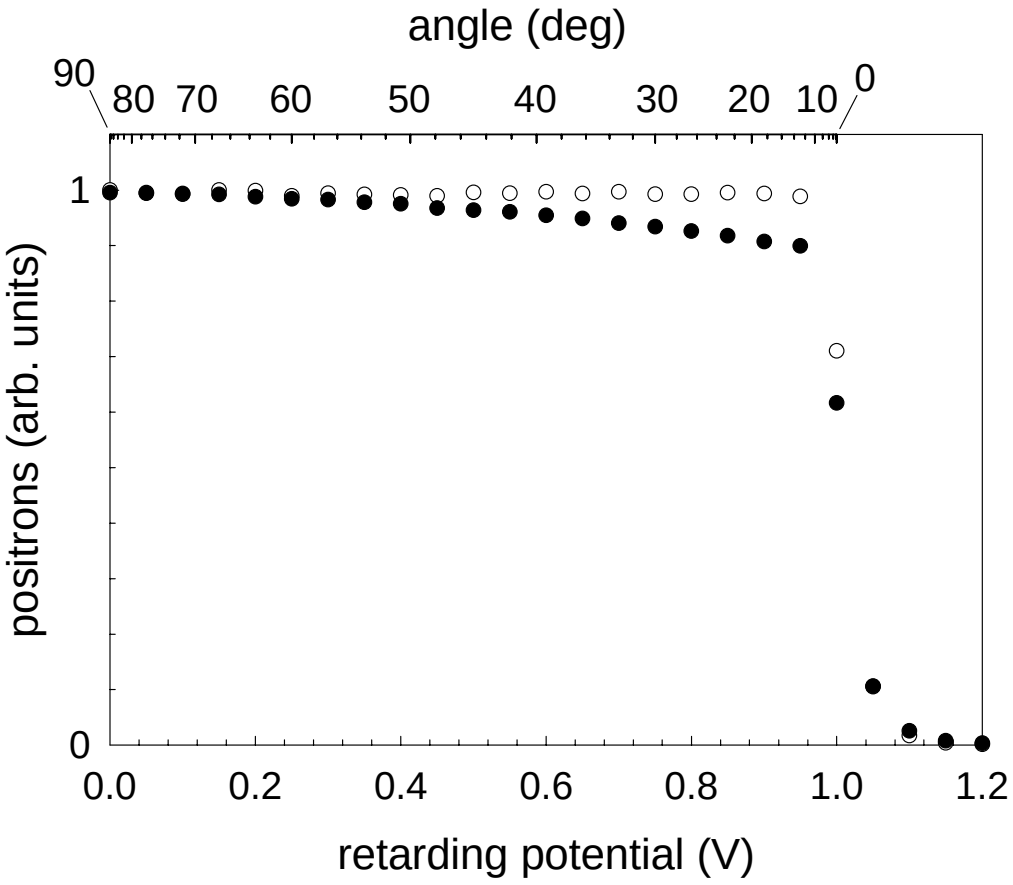

Figure 4.4: RPA data for positron-argon elastic scattering: (∘) 1 eV positron beam with no argon gas present; and (•) positron beam after scattering from argon. The upper horizontal axis indicates scattering angle corresponding to a given positron parallel energy which is shown on the lower axis.

axis shows the corresponding scattering angle θ, as defined by Eq. (4.1), for a given loss in the parallel energy of the positron. For example, a 1 eV positron which scatters transferring 0.2 eV into $E_\perp$, leaving 0.8 eV in $E_\parallel$, corresponds to a scattering angle of approximately 27°. Note that the upper axis shows only scattering angles up to 90°. Positrons that are scattered greater than 90°, (i.e. back-scattered) exit from the entrance of the gas cell. These back scattering events are discussed in Section 4.5.

Figure 4.5 shows absolute DCS measurements in atomic units for positron-krypton scattering at energies of 1.0 and 2.0 eV. Our experiment simultaneously collects both back-scattered and forward-scattered positrons [see Section 4.5],

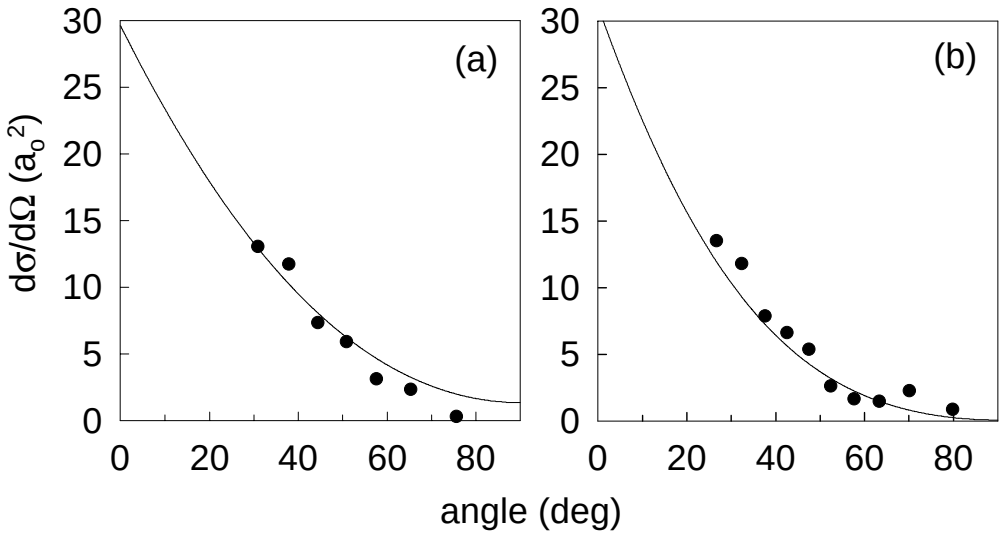

Figure 4.5: Absolute differential elastic cross sections for positron-krypton scattering at energies of (a) 1.0 and (b) 2.0 eV. Solid lines are theoretical predictions of McEachran, *et al.* [75], folded around $\theta = \pi/2$ [see Section 4.5]. There are no fitted parameters.

and so the DCS data is plotted versus the scattering angle, folded around $\theta = \pi/2$. We compare these data with the polarized orbital calculation by McEachran *et al.* [75], where the polarized orbital is a perturbation of the bound-state wave function due to the incident positron. There is good absolute agreement between the DCS data and theory, which has also been folded around $\theta = \pi/2$, over the entire range of energies and angles. For the energies of these measurements, the theoretically predicted contribution due to back-scattering is negligible, so the data represents mainly the forward-scattered positrons.

For the data taken on our earlier apparatus [i.e., Figs. 4.5, 4.6, and 4.8], the dominant source of error is statistical fluctuations due to low repetition rates. This causes an uncertainty in the measurement of $\sim \pm 20\%$. As described in Section 4.2, our new scattering apparatus has a greatly improved repetition rate (2 s vs. 20 s), which should improve this statistical error by ~ 3 for a data set taken in the same amount of time. Another source of error, which is systematic in nature, is our ability to accurately measure the test-gas pressure. This pressure is measured using a stable ion gauge located outside the scattering cell. We extrapolate the pressure inside the cell using a particle code simulation [5]. We believe that the combination of the external ion gauge and the particle code provides an absolute pressure measurement better than 10%. In the new scattering apparatus, this systematic error has been reduced to less than 1% by

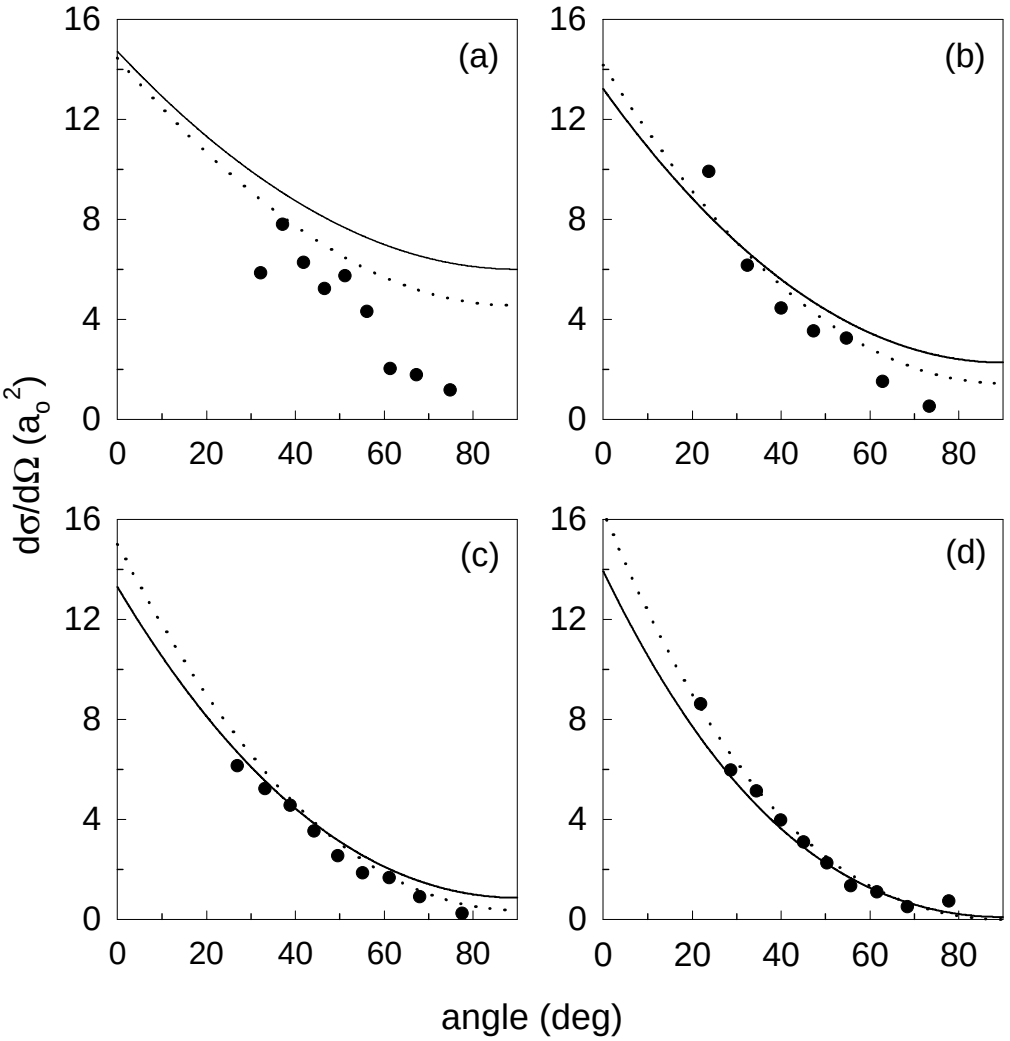

Figure 4.6: Differential elastic cross sections for positron-argon scattering at 0.4, 0.7, 1.0 and 1.5 eV are shown in plots (a)–(d) respectively. Solid and dotted lines are the theoretical predictions of McEachran, *et al.* [74] and Dzuba, *et al.* [23] respectively. The data and theory are folded around $\theta = \pi/2$ because the experiment does not distinguish between forward-scattered and back-scattered positrons [see Section 4.5].

directly measuring the test gas pressure [see Section 4.2].

We also measured previously the DCS for positron scattering from argon, which has a total scattering cross section roughly half that of krypton [31]. Figure 4.6 shows the absolute DCS for positron-argon scattering at energies from 0.4 to 1.5 eV. The solid lines are the predictions of the polarized orbital

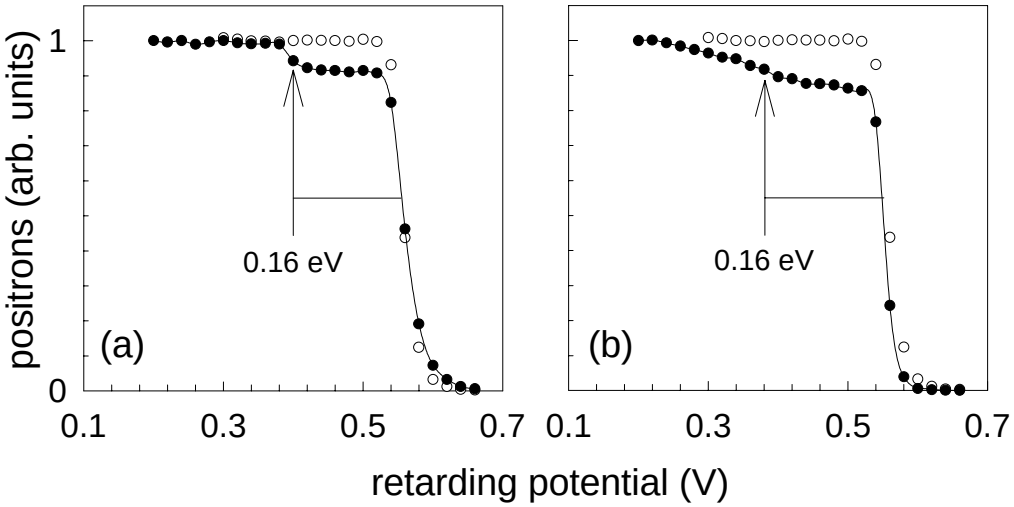

Figure 4.7: RPA data for a positron-CF_4 inelastic scattering event with a magnetic ratio between the scattering cell and analyzer of $M = 10$ in (a) and $M = 1$ in (b). The open circles correspond to a 0.55 eV positron beam with no CF_4 present. The solid circles with a spline fit (solid line) correspond to the scattered beam following excitation of the vibrational mode (υ_3) in CF_4. The arrow indicates the 0.16 eV energy loss due to the vibrational excitation.

calculations of McEachran *et al.* [74]. The dotted lines are the predictions of a many-body theory by Dzuba *et al.* [23]. For the larger beam energies, 1.0 and 1.5 eV, there is good agreement between the experiment and theory at all angles. However at lower beam energies, 0.4 and 0.7 eV, there is a systematic disagreement between the data and predictions for large angles ($\theta \geq 60°$). We believe that this is due to the effect of trapped positrons making multiple passes through the scattering cell. A discussion of this effect and the method we have developed to circumvent it is discussed in Section 4.5.

4.4.2 Total Inelastic Cross Sections

Using the cold beam, we measured the first low-energy total vibrational cross section for positron-molecule scattering, studying the excitation of the vibrational modes in CF_4 [31]. The data in Fig. 4.7, which were taken using our new scattering apparatus, show the integrated parallel energy distribution of positron-CF_4 scattering, with magnetic ratios (a) $M = 10$ and (b) $M = 1$ between the analyzer and scattering cell. The closed and open circles are measurements for a 0.55-eV positron beam with and without the CF_4 test gas present. The arrows correspond to an energy loss of ≈ 0.16 eV due to the excitation of a vibrational

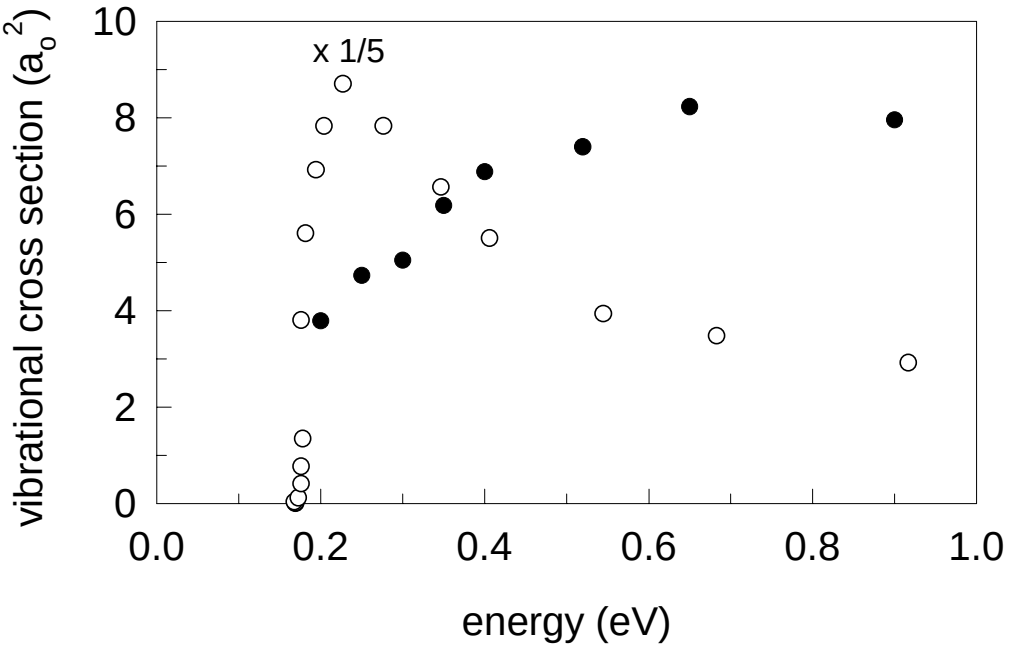

Figure 4.8: Inelastic cross section as a function of energy for the vibrational excitation of CF_4 (•) by positrons, and (◦) from electron swarm data. The electron data is from Ref. [85] and plotted at 1/5 actual value. The collisions with CF_4 excite the asymmetric stretch mode υ_3 at an energy of 0.157 eV.

mode in CF_4. We have identified this energy loss to be due to the asymmetric stretch mode υ_3 (0.157 eV). This is the dominant mode observed in both electron scattering and infra-red absorption experiments [14, 72], and it closely matches the energy loss that we observe. It is clear from Fig. 4.7 that the application of a magnetic ratio between the scattering cell and analyzer greatly reduces the effect of elastic scattering on $E_{\|}$, thus permitting accurate measurement of the inelastic scattering cross section [see Section 4.3.2]. The probability of an inelastic scattering event is determined from Fig. 4.7(b) by measuring the magnitude of the scattered component relative to that of the incident beam. The total vibrational cross section is then calculated using the scale factor C in Eq. (4.4).

Figure 4.8 shows the inelastic cross-section as a function of beam energy for positron and electron collisions with CF_4. The data in Fig. 4.8 were taken using our earlier scattering apparatus, which has a maximum magnetic ratio $M = 3$. Although this ratio does increase the separation between elastic and inelastic scattering events, it is not large enough to completely remove all elastic scattering

effects from the parallel energy distribution, and this represents a source of systematic error in the measurements. We compare our data with the only available electron vibrational cross-section measurements for CF_4, which were obtained using the swarm technique [85]. While the electron cross-section has a distinct peak above the υ_3 threshold (0.157 eV), the positron data is qualitatively different. This difference raises potentially interesting theoretical questions [39]. Although there is theoretical work on the excitation of vibrational modes in molecules by positrons [19, 28, 62], to our knowledge there are no theoretical predictions for positron scattering from CF_4. The only other measurements we are aware of for positron scattering from CF_4 are the total cross-sections measured above 1 eV by Mori *et al.* [82].

4.4.3 Recent Results

The work presented in Sections 4.4.1 and 4.4.2 represent some of the initial experiments to study two-body positron-matter interactions in the energy region below 1 eV. From this work we learned a great deal about the strengths and weaknesses of performing cold positron scattering experiments in a highly magnetized system (see Section 4.5). Using our new scattering apparatus and accumulator we are beginning to exploit this knowledge to explore positron-atomic and positron-molecular scattering processes in more detail. The following are some recent results that we have obtained. They illustrate further the large range of positron scattering processes that we can now investigate.

A number of recent experiments have focused on measuring positron-molecule total vibrational cross sections. Figure 4.9 shows total inelastic cross sections for positron excitation of the vibrational mode of CO at 0.266 eV. The data, which was taken over the range of energies from 0.5 to 7 eV, are compared to the results of (solid line) a body-fixed vibrational close-coupling theory by Gianturco *et al.* [29] and, (dotted line) earlier work by Jain [56] employing a model polarization potential. Note the excellent absolute agreement between the theoretical predictions of Gianturco *et al.* and the data.

We have also measured total inelastic cross sections in cases where more than one vibrational mode is observed. Figure 4.10 shows positron-CH_4 total vibrational cross sections at two excitation energies. The closed circles represent the combined vibrational cross sections of the υ_2 and υ_4 vibrational modes which occur at an energy of 0.190 and 0.162 eV, respectively (i.e., our present energy resolution is not sufficient to distinguish between the modes). Similarly, the open circles represent the υ_1 and υ_3 vibrational modes at an energy of 0.362 and 0.374 eV. The separation between the υ_2,υ_4 and υ_1,υ_3 modes can be seen clearly in the inset in Fig. 4.10 which shows the RPA data for 0.5 eV positron-CH_4 scattering events. It is important to note that the technique described in Section 4.3.2 allows us to make these measurements, even though the vibrational cross sections are ~ 20 times smaller than the elastic scattering cross sections.

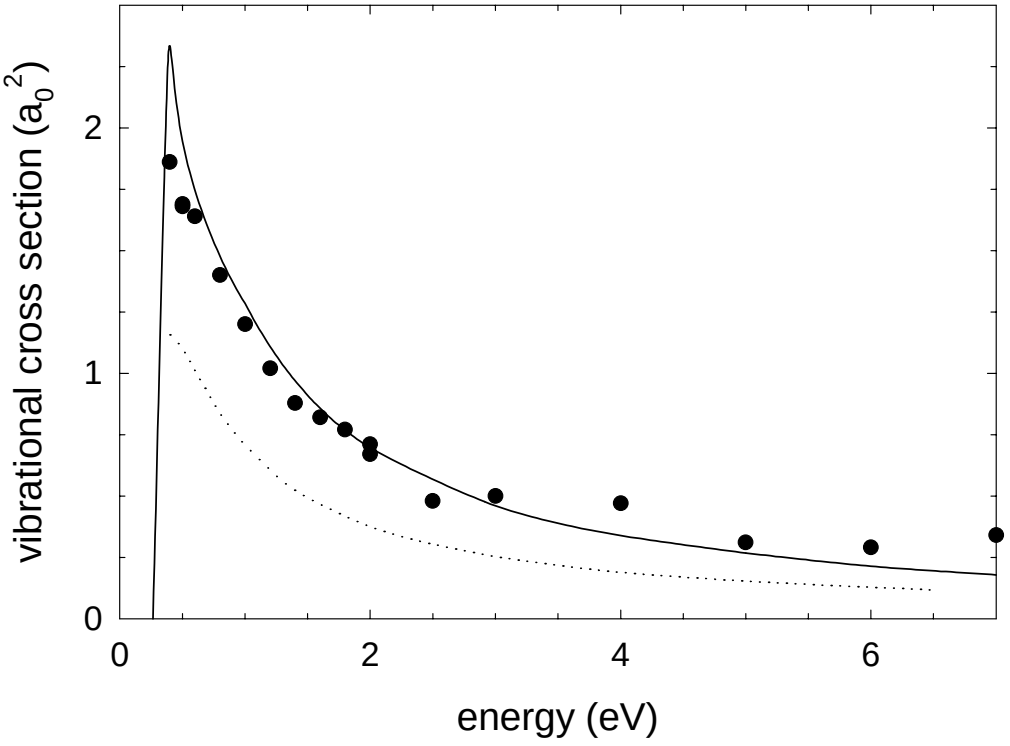

Figure 4.9: Inelastic cross section (in atomic units) as a function of energy for positron excitation of the vibrational mode of CO at 0.266 eV. The solid and dotted lines are the predictions of theories by Gianturco *et al.* [29] and Jain [56], respectively. There are no fitted parameters.

Figure 4.11 shows RPA data for a 0.5 eV positron beam scattering inelastically from CO_2. The two steps in the data set are caused by the excitation of the υ_2 bending mode and the υ_3 asymmetric stretch mode, which have energies of 0.083 and 0.291 eV, respectively. We also have indications that the inelastic cross section for the υ_1 symmetric stretch mode (which is much smaller than the other two modes) can be measured for beam energies above $\sim$ 1 eV. Our ability to measure the total vibration cross section for the υ_3 mode at 83 meV, (i.e., $\sim 4\ a_0^2$ at 0.5 eV), represents the lowest energy vibrational mode excited by positron impact ever measured, and an example of what can be expected of the cold positron beam technique.

Lastly, using the cold beam we have made total cross section measurements at energies lower than any previous experiment. Figure 4.12 shows the total cross sections for positron-molecule scattering in CF_4, CH_3F, and CH_4 at energies as

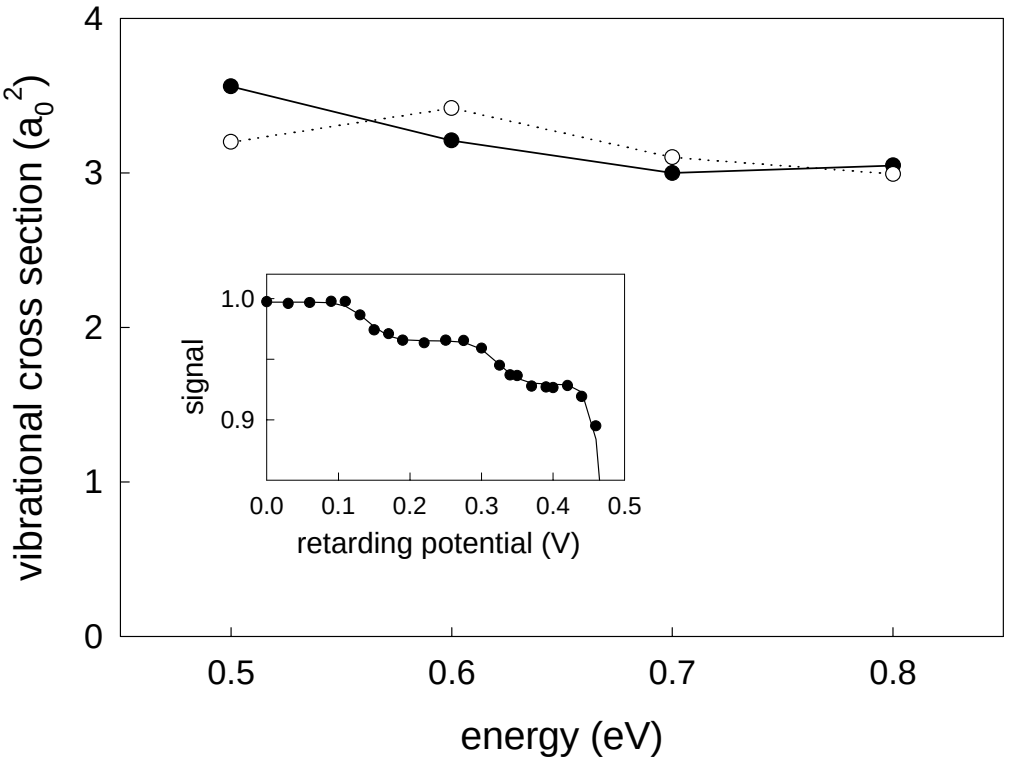

Figure 4.10: Inelastic cross section as a function of positron energy for the vibrational excitation of the (•) $\upsilon_2+\upsilon_4$, and (◦) $\upsilon_1+\upsilon_3$ modes of CH_4. The inset shows an expanded view of the RPA data for 0.5 eV positron-CH_4 scattering events. The steps represent the scattering cross section due to the excitation of the $\upsilon_2+\upsilon_4$ modes at ~ 0.18 eV and the $\upsilon_1+\upsilon_3$ modes at ~ 0.37 eV.

low as 50 meV. By extending these measurements to more of the partially fluorinated hydrocarbons, we hope to increase our understanding of the anomalously large annihilation rates for these molecules [54]. The scattering experiments described above are a small sample of what we expect to accomplish in the future using the cold positron beam.

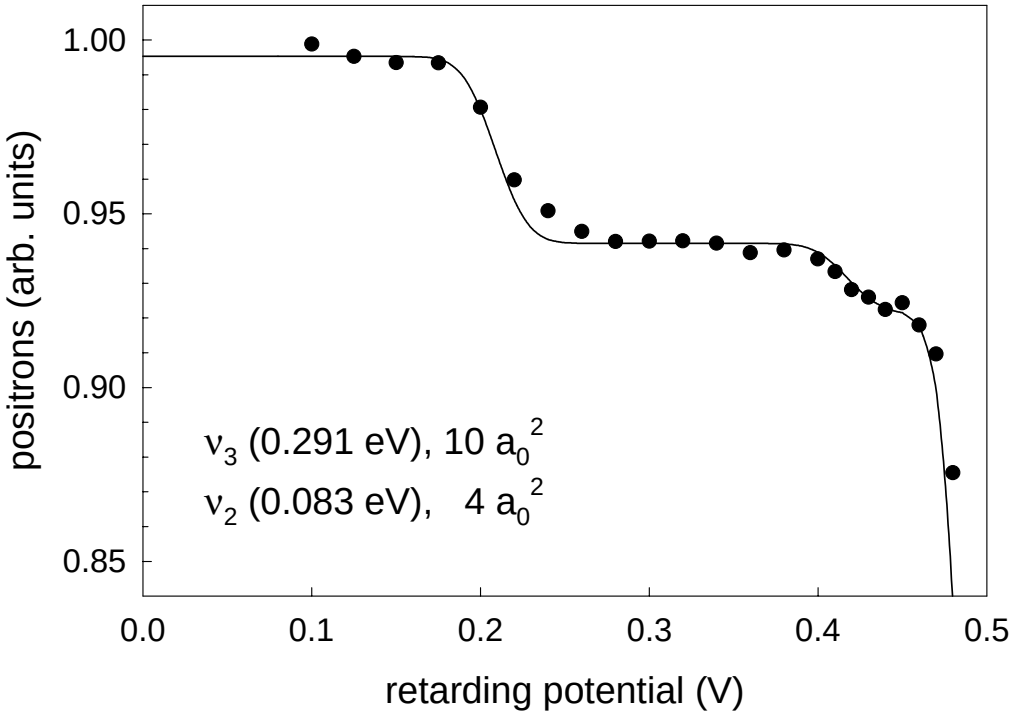

Figure 4.11: RPA data for a 0.5 eV positron-CO_2 inelastic scattering event. The two inflections represent the positron energy loss due to the excitation of the υ_2 and υ_3 modes. The solid line is a fit to the data.

4.5 Measurements Using a Magnetic Beam – Further Considerations

While scattering experiments in a highly magnetized system have some unique advantages over experiments performed using an electrostatic beam, there are also disadvantages to this approach. One difficulty is the detection of back-scattered positrons. In an electrostatic experiment this is relatively easy as long as the experiment has the capability to move the detector beyond a 90° scattering angle, which is usually possible except near 180°. In our system, the positrons are forced to follow the magnetic field after scattering. Figure 4.13(b) depicts the path of a positron as it back-scatters at 150° from an atom or molecule. The location of the positron accumulator, the scattering cell, and analyzer are shown

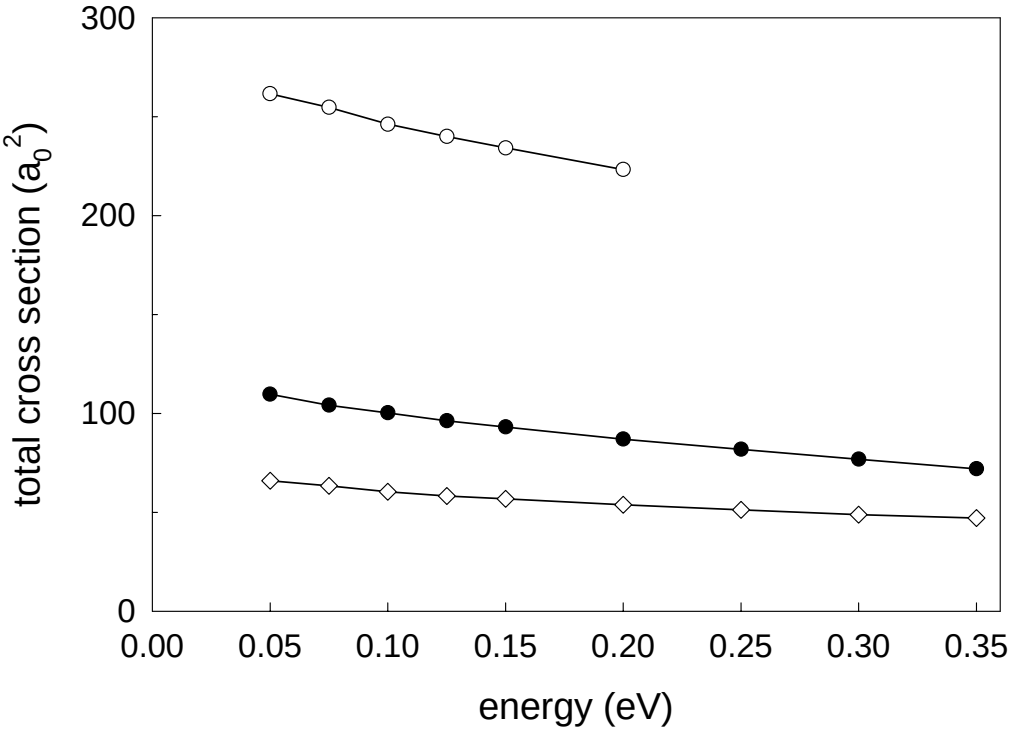

Figure 4.12: Total cross sections for positron scattering with (⋄) CF_4, (∘) CH_3F, and (•) CH_4.

in Fig. 4.13(a). The horizontal arrows show the path of the positron through the scattering apparatus, while the vertical arrows depict the energy transfer from $E_{||}$ into $E_{\perp}$ due to an elastic scattering event. When the positron back-scatters, it transfers some of its parallel energy into perpendicular energy and travels back out of the entrance of the scattering cell. Since it has lost some $E_{||}$, it is then reflected by the potential barrier created by the positron accumulator [see Fig. 4.13(b)] and travels back through the scattering cell, where it has a 90% probability of passing through the cell without scattering (since the single pass scattering probability has been adjusted to be 10%). If the positron is not scattered in the second pass through the cell, the RPA will detect the positron as if it were scattered at 30° in the forward direction. Thus, we are unable to distinguish between back-scattered and forward-scattered positrons, and so we display the DCS results as a superposition of the two scattering components folded around $\theta = \pi/2$. We are currently developing a technique to which will

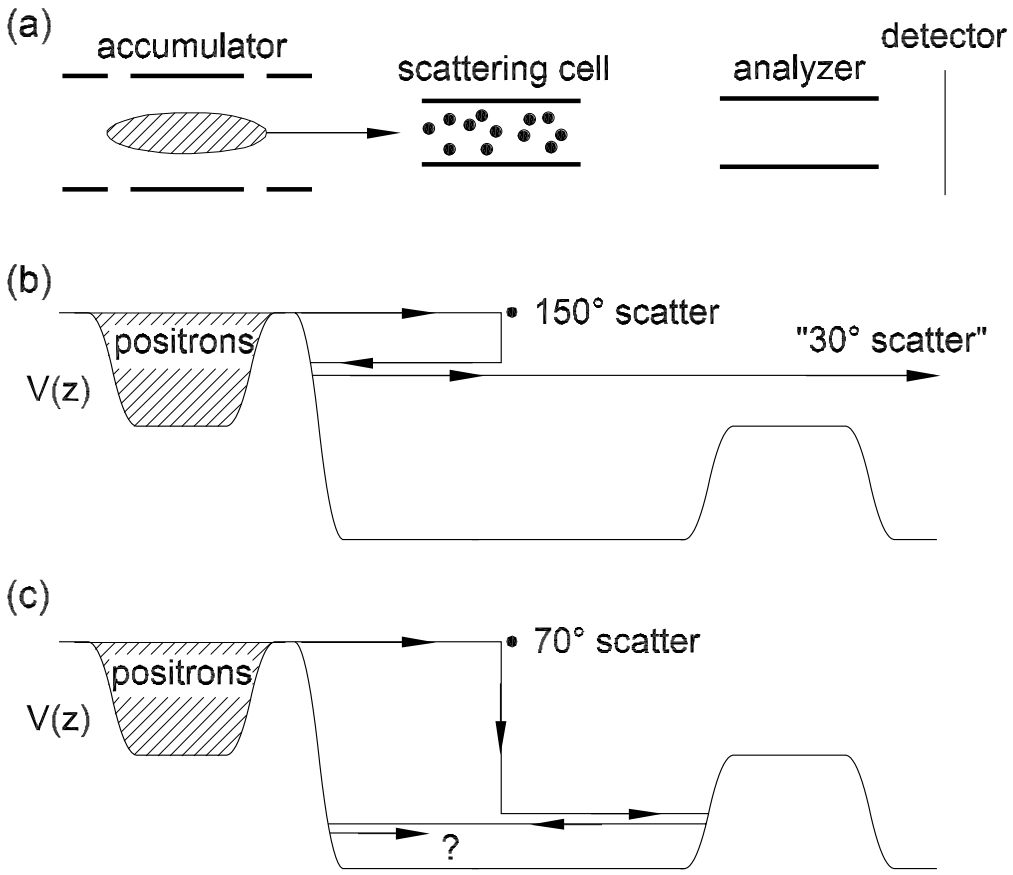

Figure 4.13: (a) Schematic diagram of the scattering experiment, showing the relative positions of the positron accumulator, scattering cell and retarding potential analyzer. The lower figures show the path of a positron: (a) after a 150° scatter with the test gas; and (b) after a 70° scatter. Vertical parts of the trajectories indicate a transfer of energy from the parallel energy component $E_{\|}$, into the perpendicular component $E_{\perp}$, due to elastic scattering events.

allow us to distinguish between the back-scattering and forward-scattering events in order to obtain the full DCS (see Section 6.2.2).

Another effect of scattering in a magnetic field was discovered through a systematic discrepancy between our DCS data and theoretical predictions for large angle scattering ($\theta > 60°$) [see Section 4.4.1]. We noticed that when the theory predicted appreciable scattering cross sections at large angles, our experimental results were consistently low [see Fig. 4.6 (a) and (b)]. Figure 4.13(c) shows the motion of a positron as it scatters elastically at 70°. In this scattering event, the positron transfers an appreciable amount of $E_{\|}$ into $E_{\perp}$. If

the RPA is set up to discriminate against a 70° scattering event, the scattered positron will be trapped in the potential well created by the analyzer and the positron accumulator exit gate, as shown in Fig. 4.13(c). After each bounce, the positron passes through the scattering cell potentially rescattering from the test gas. If the positron rescatters, it can transfer some of its $E_\perp$ back into $E_\parallel$, thereby allowing it to pass through the analyzer and be detected. This will have the effect of making large angle scattering events look like small angle ones in the DCS data. Since the positron must bounce back and forth a number of times before it has a significant chance of rescattering, these secondary scatters can be eliminated by time resolving the measurement.

Such time-resolved measurements have been accomplished using a potential barrier [not shown in Fig. 4.13(a)] located in front of the detector, to prevent any trapped positrons which have rescattered from reaching the detector. The potential barrier is raised after a few microseconds, which is enough time for the initial scattered beam to pass the barrier, but is still short enough to block any rescattered positrons. A typical bounce time for a trapped positron is a few micro-seconds, and so in order to distinguish between the initial scattering event and any rescattered positrons, the beam must have a pulse width less than this. We have been able to create cold pulsed positron beams with a FWHM pulse width less than 1 μs, which are suitable for this purpose. Figure 4.14 shows the effects of time resolution on a 0.7 eV positron-argon DCS. The open circles and filled circles are data taken without and with time resolution, respectively. Looking at the solid lines, which are fitted to the data, one can see that time resolution in the DCS measurement results in an increase in the measured large angle scattering and a decrease in the small angle scattering, which is what one would expect if the rescattered positrons were eliminated. Thus the data in Fig. 4.14 indicates that, by time resolving the data, we can eliminate the difficulty of secondary scattering at large angles.

Another complication in studying scattering using a highly magnetized system is the insensitive detection of scattering events near 90°. Equation (4.3) shows that the probability of a scattering event is proportional to the positron's path length. As we have discussed, a positron in a magnetic field travels along a helical path. Therefore, the path length of a positron traveling through the scattering cell will be greater than the length of the cell. The ratio of these two lengths depends only on the ratio of the energy components, $E_\perp$ and $E_\parallel$,

$$l_{\text{helix}}/l_\parallel = \sqrt{1 + E_\perp/E_\parallel}, \tag{4.7}$$

where l_{helix} is the path length of the positron and $l_\parallel$ is the effective path length for a positron moving in a straight line along the magnetic field. For a cold positron beam with $E_\parallel$ of 1 eV and $E_\perp$ of 0.025 eV, the ratio $l_{\text{helix}}/l_\parallel$ is 1.01, or a 1% correction to the straight path, which is negligible. Problems occur for scattering events close to 90°. In this case, the positron transfers nearly all of its

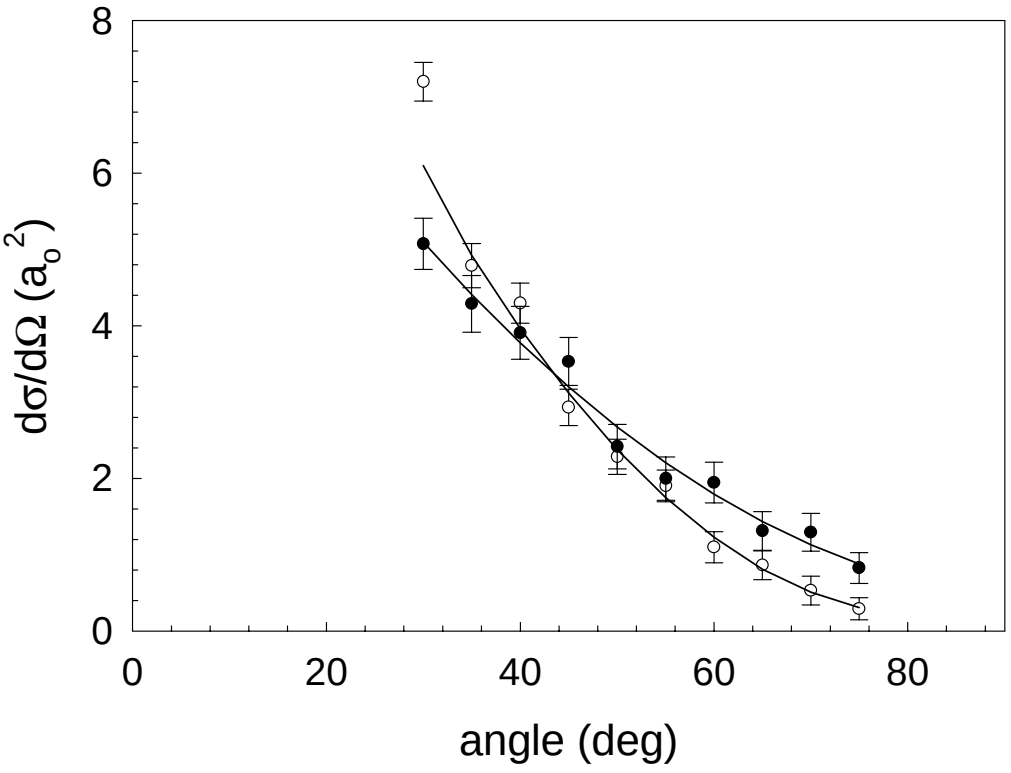

Figure 4.14: Effects of time resolving the DCS measurement for 0.7 eV positron-argon scattering: (∘) data taken without time-resolution and (•) with time-resolution ($\Delta t = 6\ \mu s$). The solid lines are fit to the data. Time resolution increases the detection efficiency for large angle scattering events.

parallel energy into the perpendicular component. It then moves slowly through the cell, gyrating rapidly in the direction perpendicular to the magnetic field until it makes another scattering collision.

We can estimate the maximum angle at which single scattering can be assumed by requiring that the probability for a second scattering event be small. On average, the positron will scatter in the center of the gas cell. Since we have set the probability of scattering to 10% for a path length l equal to the scattering cell length, we can increase the path length by a factor of 6 and still have an acceptable probability for a second scatter of only 30%. Using Eqs. (4.1) and (4.7), this implies that any initial scattering at less than 80° will have less than a 30% chance of scattering a second time.

Some difficulties are common to both the magnetized and electrostatic scattering experiments. An example is measurement of differential scattering near zero degrees. For the electrostatic case, the problem is caused by an inability to physically locate the detector near the unscattered beam, which is necessary to measure small-angle scattering. The difficulty for the magnetized system is the inability to separate the parallel energy distribution for small angle scattering from that of the incident beam. This difficulty is compounded by effects represented in Eq. (4.1), which relates the scattering angle to an energy transfer out of $E_{||}$ and into $E_{\perp}$. One can see from this equation, which is plotted as the upper horizontal axis in Fig. 4.4, that scattering angles below 10° are difficult to study, even with our cold positron beam. This problem can, in principle, be circumvented using a colder beam. Similar problems to those near 0° are encountered for scattering angles near 180° in both the magnetic and electrostatic experiments

Conducting the experiments in a magnetic field has some distinct advantages and disadvantages compared to electrostatic scattering experiments. The distinct advantage is that we can conveniently use our state-of-the-art cold positron beam, allowing us to study scattering in the range of energies $E < 1$ eV which has previously been inaccessible to experiments. In addition, the advantages include a large effective detector size (all scattered positrons are collected), no moving parts, and a simple gas cell and analyzer design (with no need for a complicated gas jet). Some of the disadvantages include a more complicated analysis, differential cross sections near 90° are difficult to detect, and measuring the DCS with both elastic and inelastic processes present is also difficult [see Section 4.5].

4.6 Chapter Summary

We have begun to exploit the ability to produce a state-of-the-art cold positron beam to study atomic and molecular physics in a new range of positron energies. This effort has led us to investigate techniques to study scattering events in a magnetic field. We are continuing to improve our understanding of this type of experiment. Even at this early stage of development, we have been able to make new measurements in the energy range below 1 eV, including DCS measurements where even the equivalent electron experiments have proven difficult. Examples of these include, positron-atom DCS for argon and krypton at energies ranging from 0.4 to 2.0 eV. As discussed above, we have been able to make the first measurements of low-energy positron-molecule vibrational cross sections, studying positron-CF_4 collisions down to positron energies as low as 0.2 eV.

Currently, we are continuing our study of positron-molecular vibrations, by measuring the total vibrational cross sections for a broad range of molecules including CO, CO_2, and CH_4, at energies from 0.5 up to 7 eV. We have also

begun studying total cross sections for positron-molecule scattering and have recently measured positron total scattering cross sections for CF_4, CH_3, and CH_4 at energies from 50 meV to several electron volts. By continuing to push the limits of low-energy positron scattering, we hope to study a broad range of positron-matter interactions, not only in atomic and molecular systems but also in materials and at material surfaces [37].

Chapter 5

The Electron-Positron Beam-Plasma Instability

5.1 Introduction

Electron-positron plasmas are examples of a larger class of equal-mass plasmas (or pair plasmas) that owe their unique properties to the symmetry between the two oppositely charged species. Electron-positron plasmas in particular have been extensively studied theoretically because of their relevance in astrophysical contexts such as pulsar magnetospheres [76]. The linear properties of these plasmas are well known [51, 107, 111]. Their nonlinear properties are currently the focus of theoretical and numerical investigations [22, 42, 63, 70, 90, 92, 96–98, 112, 113].

Studies of electron-positron plasmas in the laboratory present substantial challenges to the experimentalist. Until recently, insufficient numbers of positrons were available to create even single-component positron plasmas. With the introduction of a modified Penning-Malmberg trap for accumulating large numbers of positrons [104], it became possible to conduct the first electron-positron plasma experiments in a beam-plasma system [34]. Unfortunately, the accumulation of large numbers of positrons is possible only because of the outstanding confinement properties of Penning traps [87], which can confine only one sign of charge. The creation of an electron-positron plasma in the laboratory requires solving the classic plasma physics problem of neutral plasma confinement, and none of the current configurations for confining neutral plasmas has sufficiently good confinement for electron-positron plasmas.

One possible approach to creating equal-mass plasmas is to use positive and negative ions rather than electrons and positrons. Plasmas containing both positive and negative ions are relatively easy to create by the well-known method of producing a hot-cathode discharge in a mixture of electronegative and electropositive gases such as sulfur hexafluoride and argon. Positive ions are created

by ionization of the argon and negative ions are created by electron attachment to the sulfur hexafluoride [50]. Unfortunately, for the experiments conducted to date, there was a rather large mass ratio between the ions (140:40 for SF_6 and Ar), and so these plasmas are not strictly equal-mass plasmas. Even if it were possible to obtain a more nearly equal mass ratio by the judicious choice of gases, a fundamental problem remains: it is currently impossible to entirely eliminate the small residual electron component, which can completely alter the properties of such plasmas, even in concentrations of less than 1%. Plasmas of this type are therefore properly considered to be three-component plasmas.

Using another approach, Schermann and Major created an electron-free plasma consisting of positive and negative ions of (almost) equal mass in a Paul trap by ionizing thallium iodide to create Tl^+ and I^- ions [93]. The deconfining effects of RF heating were overcome by the cooling effect of a light buffer gas, helium. For electron-positron plasmas, this approach is much less attractive, because the cooling effect of helium for light particles will be minimal. This approach may work, however, by using a molecular species with a high inelastic cross section to provide the required energy loss mechanism. On the basis of current knowledge of positron-molecule collision cross sections, the vibrational excitation of carbon tetrafluoride is the most attractive candidate (see Section 4.4.2). In addition to the Paul trap other approaches to confine equal-mass plasmas have also been investigated, including the use of combined traps [108], magnetic mirrors [6], and nested traps [36].

Nonetheless, all of these techniques are still relatively complicated, and were not attempted for the experiments described in this chapter. Instead, we approached the experimental study of the electron-positron plasmas by investigating the electron-positron beam-plasma system. This approach involves transmitting the abundant species (the electrons) in a single pass through the scarce species (the positrons) confined in a Penning trap. This permits us to take advantage of the good confinement properties of positron plasmas in Penning traps, while still studying a two-component equal-mass system.

The beam-plasma system is interesting in its own right. The free energy in the relative streaming of the two species can give rise to a variety of instabilities and consequent plasma heating [99]. These effects can be important in a variety of laboratory, magnetospheric and astrophysical plasmas. Beam-plasma effects are currently being investigated theoretically for electron-positron plasmas in the context of wave generation and particle acceleration [22, 42, 92, 112]. The transit-time instability, which is the subject of this chapter, was first studied because of its potential as a source of microwave radiation [45, 83].

The data described in this chapter represents a second generation beam-plasma experiment. In our earlier beam-plasma experiments, an electron beam formed from a hot cathode was transmitted through a positron plasma stored in both a cylindrical and quadrupole Penning trap geometry. In the cylindrical case, a two-stream instability, which caused strong heating of the plasma, was

studied. When the electron beam was passed through a positron plasma stored in a quadrupole Penning trap geometry, the electron beam produced a transit-time instability which excited the center of mass mode in the plasma. Because of the large energy spread generated by the hot-cathode electron gun, both experiments were restricted to studying the instabilities at energies above ~ 1 eV. However, theoretical predictions for both the cylindrical [26] and quadrupole [21] trap geometries showed that the maximum growth rate and onset of the instability should occur below this energy. It was clear, therefore, that the narrower energy spread of the electron beam described in Section 5.2.2 would greatly improve the ability to study the instabilities in the energy range near their onset.

This chapter discusses the first application of this electron beam, using it to further investigate the transit-time instability for a positron plasma stored in a quadrupole well. New results are presented exploring the instability in the previously unexplored energy range, including the low-energy onset of the instability. These results are compared with the predictions of a new analytical cold-fluid theory that accurately models the system, and excellent agreement is obtained. Future plans for beam-plasma experiments done both in the cylindrical and quadrupole Penning traps are also discussed.

This chapter is structured as follows. In Sec. 5.2, the details of the experimental apparatus and techniques used to perform the experiments are presented. In Sec. 5.3, the experimental results are discussed and compared with theory. Finally, a summary is presented in Section 5.4.

5.2 Description of the Experiment

All of the data described in this chapter was taken on the earlier apparatus. Figure 5.1(a) shows a schematic drawing of the beam-plasma experiment. The apparatus consists of a cylindrical Penning-Malmberg trap coaxial with a quadrupole Penning trap. Both traps are enclosed in the same vacuum vessel and use the same confining magnetic field. As shown in Fig. 5.1(a) and (b), the cylindrical trap is the third stage of the three-stage accumulator.

The procedure for conducting the experiment can be split into three phases: (1) Accumulation of a cold positron plasma, which is stored in the quadrupole trap; (2) Accumulation of a reservoir of thermalized electrons stored in the cylindrical trap, and the extraction of an electron beam from this reservoir; and (3) measurement of the excitation of the transit-time instability in the positron plasma by the electron beam. A more detailed explanation of these three phases is presented below.

5.2.1 Positron Plasma Parameters

A plasma containing 1.6×10^7 positrons is accumulated in the cylindrical trap using the technique described in Section 2.4 and then shuttled into the quadrupole

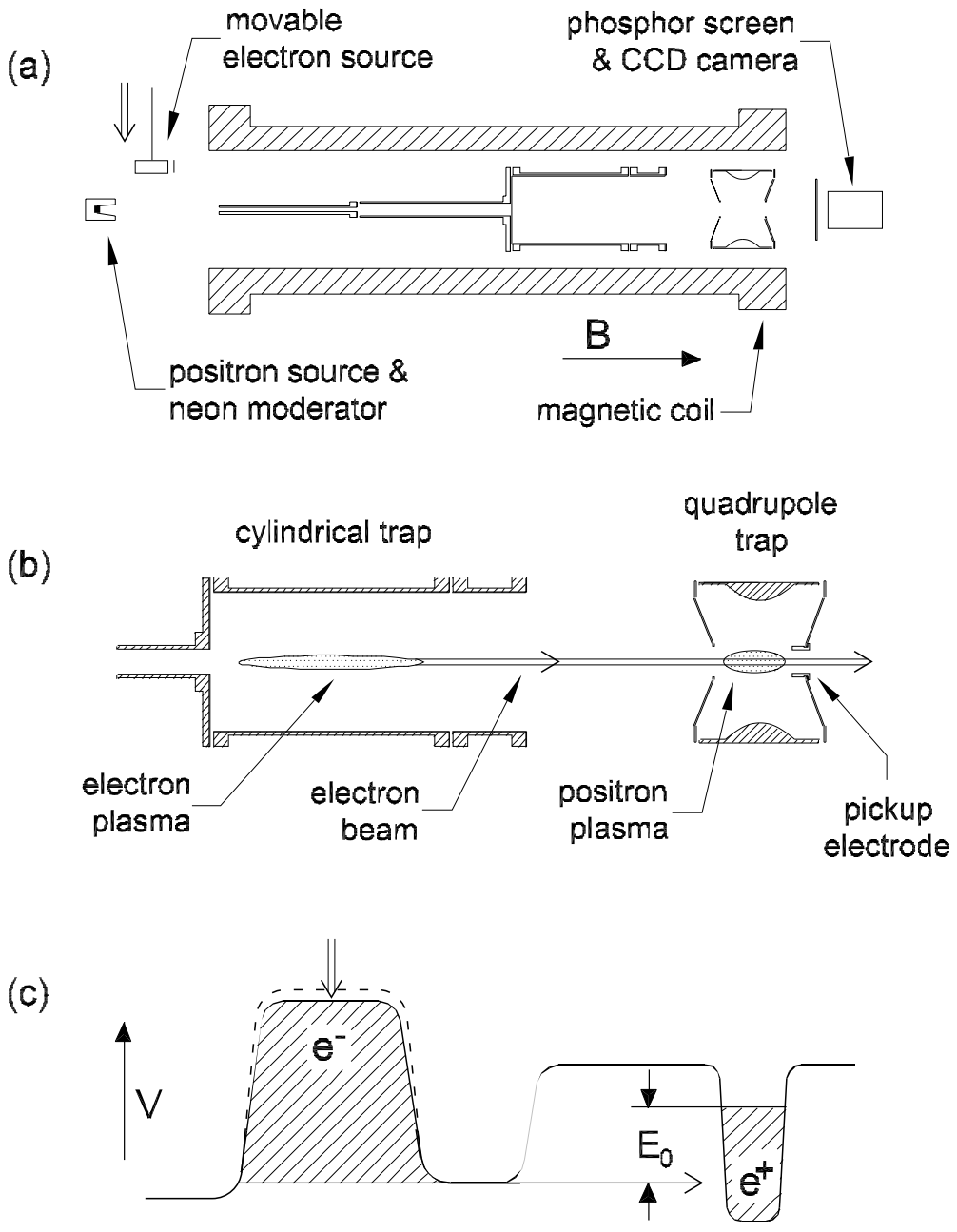

Figure 5.1: (a) Schematic diagram of the beam-plasma experiment showing the ^{22}Na positron source and moderator, movable hot-cathode electron source, magnetic field coil, imaging system, and trap electrode structures. (b) Expanded diagram of the cylindrical and quadrupole Penning traps. Each trap consists of three electrodes from left to right, referred to as the entrance-gate, dump, and exit-gate electrodes. The quadrupole trap also has a small pickup electrode located near the positron plasma. (c) Schematic diagram of the potential profile V(z) used to contain the electrons and positrons in there respective potential wells.

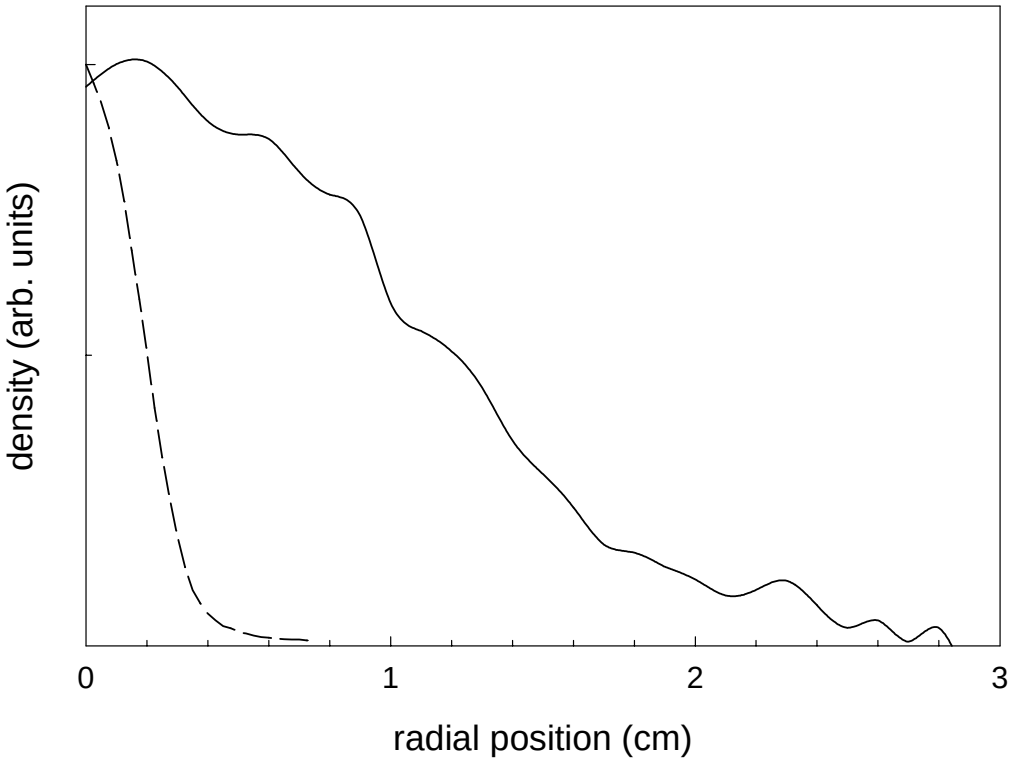

Figure 5.2: Axially integrated radial density profile of a plasma containing 1.3×10^7 positrons (solid line). Also shown is the radial profile of the electron beam (dashed line), which is formed from a cold plasma containing 1×10^9 electrons. As discussed in the text these profiles indicate a positron plasma diameter of $D_p \simeq 2.4$ cm and an electron beam diameter of $D_b \simeq 0.4$ cm.

trap at an efficiency of 80%. The plasma cools to room temperature (0.025 eV) in approximately 1 s by further collisions with the nitrogen buffer gas [38]. The buffer gas is then pumped out to a base pressure of 5×10^{-9} torr in 10 s.

In order to confirm that the accumulated positrons are in the plasma state, it is necessary to obtain plasma parameters such as the Debye length and the dimensions of the charge cloud. These parameters were not measured directly, but inferred from measurements of the axial-integrated plasma density profile. This is accomplished by dumping the plasma onto a phosphor screen biased to -10 kV, which is then imaged using a CCD camera [see Fig. 5.1(a)]. The solid line in Fig. 5.2 shows a typical axial-integrated radial density profile of a plasma containing 1.3×10^7 positrons. The dashed line represents the narrower density profile of the electron beam, which will be described in Sec. 5.2.2. The radial

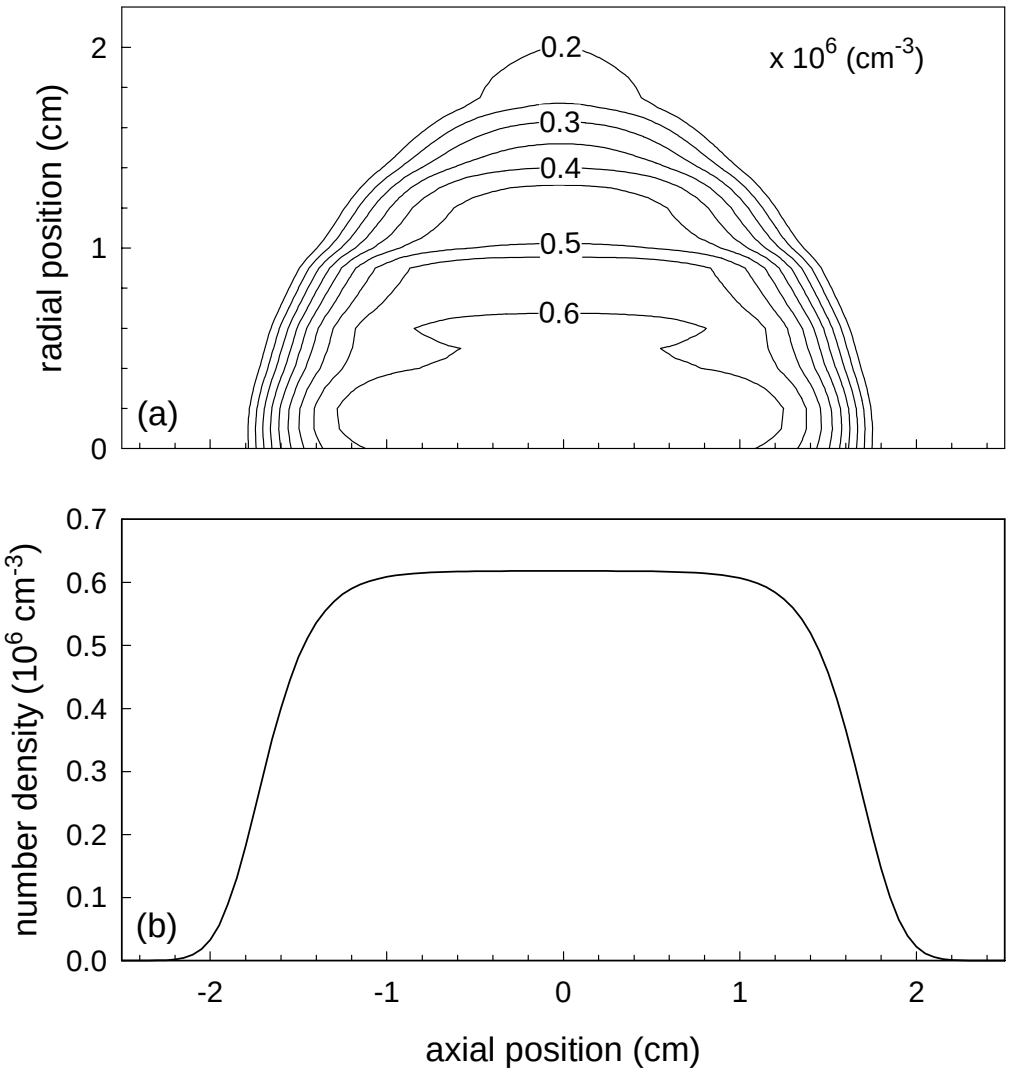

Figure 5.3: (a) Contour plot of the density of a 1.3×10^7 positron plasma stored in the quadrupole well. It was calculated using a Poisson-Boltzmann equilibrium code, using the radial density profile of the positrons shown in Fig. 5.2 as the initial positron distribution. (b) Positron number density along the trap axis, indicating a central density of $n_p \simeq 6 \times 10^5$ cm^{-3}.

density profile of the plasma is used as input to a Poisson-Boltzmann equilibrium code to calculate the spatial distribution of the positrons in the trap.

The results of this calculation are displayed in Fig. 5.3(a), which shows the

positron number density as a function of position in the plasma. From the figure a plasma length of $L_p \simeq 2.8$ cm FWHM and a plasma diameter of $D_p \simeq 3$ cm FWHM is determined. These dimensions corresponds to a plasma aspect ratio of $\alpha = L_p/D_p \simeq 0.9$. We note that the plasma diameter calculated in this way is slightly larger than the plasma diameter given in Fig. 5.2. This is due to the line-integrated nature of the CCD camera image, versus the three dimensional positron density profile in Fig. 5.3(a).

Figure 5.3(b) shows the positron number density as a function of position along the axis of symmetry of the trap. The figure indicates a central plasma density of $n_p \simeq 6 \times 10^5$ cm^{-3}, yielding a Debye length of $\lambda_D \simeq 1.5$ mm. By comparing the Debye length with the plasma dimensions, we see that $\lambda_D \ll L_p$, $\lambda_D \ll D_p$, and $N_D \sim 10^4 \gg 1$, where N_D is the number of positrons in a Debye sphere. Thus, the charge cloud indeed satisfies all of the conditions to be a single-component plasma.

The last parameter needed for the analysis of the experiment is the plasma space charge potential. It is important to determine this parameter because it effects the energy of the electron beam as it passes through the positron plasma [see Section 5.2.3]. The space charge potential is determined by dumping the plasma and measuring the potential difference on the dump electrode at the start and stop of the dump, as defined by the potential when the positrons start exiting the trap and the potential when all the positrons have been expelled, respectively. For the plasmas used in this experiment, a space charge of 1.6 V is typically measured. In order to verify the direct measurement of the space charge, the Poisson-Boltzmann code was used to calculate it. Figure 5.4 shows the potential profile of the quadrupole trap along its axis of symmetry with and without a positron plasma present. The difference between the two curves represents the positron plasma space charge of ~ 1.3 V for a plasma containing 1.3×10^7 positrons. The discrepancy between the space charge measurement and calculation is most likely caused by uncertainties in the measured total number of positrons, which is needed in the Poisson-Boltzman code.

5.2.2 Cold Electron Beam Parameters

Following accumulation of a positron plasma in the quadrupole trap, a cold electron beam is generated in the manner described in Section 3.4. To accurately study the electron-beam positron-plasma transit-time instability, the rise time of the electron beam current, t_r must satisfy the condition $t_r \ll 1/\gamma$, where γ is a typical growth rate of the instability ($\sim 5 \times 10^4$ s^{-1}), and the beam current must remain constant over the duration of the interaction. We use the adaptive dump technique (see Fig. 3.6) to produce a beam that satisfies these criteria.

It is also important that the beam diameter be small compared to the plasma diameter. One simple way to accomplish this is by making the electron beam source diameter small compared to the positron plasma, since the extracted

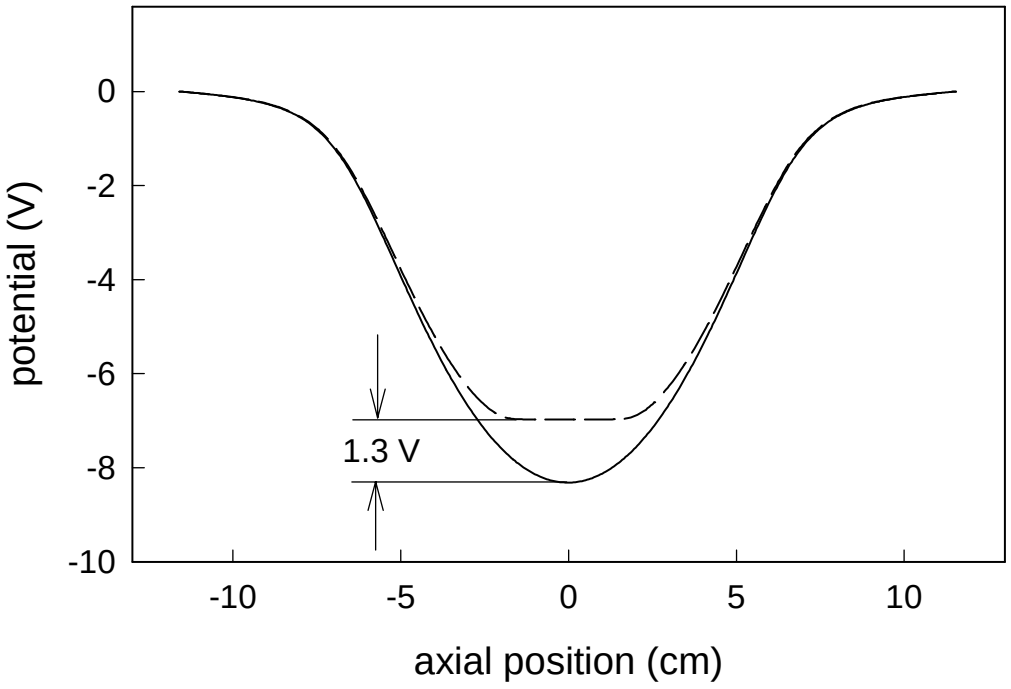

Figure 5.4: Potential profile along axis of symmetry of the trap without any charge present (solid line), and with 1.3×10^7 positrons (dashed line). The difference in potential between the two plots at the center is due to the plasma space charge of 1.3 V.

electron beam diameter is directly related to the size of the electron source. To do this, a 2.9 mm aperture is located in front of the hot-cathode electron gun. Figure 5.2 compares the radial profiles of the electron beam and positron plasma. The figure indicates an electron beam diameter $D_b \simeq 4$ mm. Thus the electron beam diameter is smaller than that of the plasma, and there is little radial expansion during the beam formation process.

5.2.3 Beam-Plasma Experiment

The beam-plasma transit-time instability is studied in the following manner. First, a positron plasma of 1.6×10^7 positrons is accumulated in the cylindrical trap and transferred into the quadrupole trap. As the positron plasma cools to room temperature, the hot-cathode electron gun is moved into position [see Fig. 5.1(a)], and an electron plasma is accumulated in the cylindrical well. Figure 5.1(c) shows schematically the potential profiles generated by the cylindrical

and quadrupole traps that are used to confine the electron and positron plasmas, respectively, along with the space charge of both plasmas (indicated by shading). After the electron and positron plasmas have cooled to room temperature, an electron beam is generated and magnetically guided through the positron plasma. As the electron beam traverses the positron plasma, the transit-time instability causes the center of mass oscillations to grow in amplitude. The oscillations are detected using a pickup electrode, shown in Fig. 5.1(b), which measures the image charge generated by the positron plasma.

After each cycle, the beam energy is adjusted by varying the potential on the exit-gate electrode of the cylindrical trap. The energy of the electron beam relative to the positron plasma is denoted in Fig. 5.1(c) by E_0. The relative beam energy is the sum of eV_s and eV_t, where V_s is the space charge of the positron plasma, and V_t (which is negative in Fig. 5.1(c)) is the potential difference between the dump electrode of the quadrupole trap and the exit-gate electrode of the cylindrical trap. For example, if the dump and exit-gate electrodes of the quadrupole and cylindrical traps were both at the same potential, the electron beam energy through the positron plasma would be eV_s.

As we discuss in the next section, in an earlier study of the transit-time instability [34] the measured growth rates were an order of magnitude larger than they are for the current experiment. Consequently, when the electron beam passed through the plasma, any noise in the plasma could act as a "seed" for the growth of the instability. In the current experiment, there are a few beam energies where the growth rates are not large enough to insure that the center of mass mode can grow above the detection amplifier noise before the reservoir of electrons is depleted. In these cases, we found it essential to actively "seed" the center of mass mode to some small amplitude before the electron beam is turned on. This is accomplished by applying a sinusoidal signal, at the same frequency as the center of mass mode (~ 4.2 MHz), to the entrance gate of the quadrupole trap. Because of the high-Q properties of the quadrupole trap, the timing of the seeding is not critical, and can be done as much as a few milliseconds before the electron beam is turned on. To insure that the seeding processes does not effect the measured growth rate a systematic check was performed by measuring the instability growth rate with and without actively seeding the plasma in an energy regime where the seeding was not necessary.

5.3 Results

Figure 5.5 shows the rms signal from the pickup electrode as the electron beam passes through the positron plasma. The inset shows a 2.6 μs long time record of the pickup electrode signal, illustrating the individual oscillations at 4.2 MHz. The plasma center of mass mode has an oscillation frequency corresponding to that of a single positron oscillating in a quadrupole potential well. This frequency

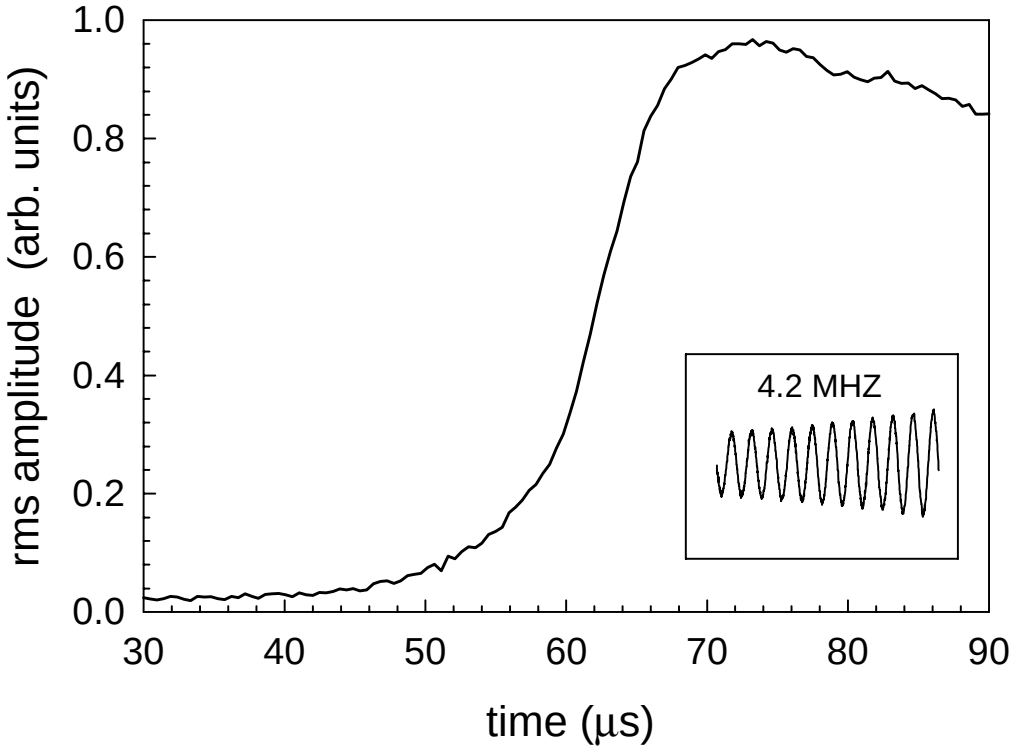

Figure 5.5: The rms amplitude from the pickup electrode signal, showing the growth of the transit-time instability excited by an electron beam traversing a positron plasma stored in a quadrupole Penning trap. The inset shows the pickup electrode signal on an expanded time scale at 60 μs, illustrating the individual center of mass oscillations at a frequency of 4.2 MHz.

is given by $f_z = \sqrt{qV/4\pi^2 m Z_0^2}$, where q is the positron charge, $V \simeq 15$ V is the potential difference applied between the end and dump electrodes, m is the positron mass, and $Z_0 \simeq 6.3$ cm is a length parameter which is defined by the quadrupole geometry [109]. Using this expression, a center of mass oscillation frequency $f_z \simeq 4.1$ MHz is predicted. The difference between the calculated and measured frequencies is likely due to small departures from the ideal quadrupole geometry.

The electron beam is turned on at $t = 0$ exciting the instability in the plasma. Some time later the amplitude of the center of mass oscillations begin to grow out of the noise in the center of mass mode. After the initial linear growth, the growth rate of the center of mass mode begin to decrease, causing the amplitude

of oscillation to overshoot its final value and then eventually stabilize (not shown in Fig. 5.5). In the earlier study of the transit-time instability [34], the initial growth phase was also followed by a decay phase. Using a γ-ray detector, it was determined that the decay in this case was due to the ejection of positrons from the quadrupole trap when the plasma oscillations became so large that they were no longer confined by the potential well. We note that the potential well confining the positrons was ~ 6 eV deep, and the electron beam energy used was only $1 - 2$ eV, so that some of the positrons must have been accelerated to energies much larger than that of the relative beam energy. A particle-in-cell simulation confirmed this, showing that the center of mass mode, could cause the ejection of positrons from the trap [34].

In the present experiment, we decided to study the system in a less violent regime. To accomplish this, beam currents were used that are an order of magnitude smaller than in the earlier experiment. This resulted in small amplitude plasma oscillations. We verified using a γ-ray detector that these oscillations do not eject positrons from the potential well, and therefore the overshoot and saturation of the center of mass mode must be caused by an effect other than positron ejection. The most likely possibility is that non-linear plasma effects are responsible for the observed saturation. We have not yet carried out a detailed study of the saturation, but believe that it is likely to be an interesting area of further research.

Figure 5.6 shows the measured instability growth rate as a function of beam energy for two beam currents. The predictions of an analytic cold-fluid theory, developed by Dubin [21], are also shown. This theory, which has no fitted parameters, is in excellent agreement with the data over the entire range of energies studied. The agreement with the cold-fluid theory implies that the system acts like a transit time oscillator, exciting a high-Q oscillation of the center of mass motion of the plasma. The theory also predicts that the instability growth rates scale linearly with beam currents, which is confirmed by the data sets taken with beam currents of 0.03 and 0.08 μA. Our previous experiments, which also agreed with the cold-fluid theory, were limited by large beam energy spreads to studying the instability at beam energies above the maximum of the growth rate. The new cold electron beam allows us to study the instability over the entire range of interest; from onset through the maximum growth rate and beyond. We note that the data indicates the onset of the instability occurring at an energy 0.05 eV below the theoretically predicted onset. This discrepancy is most likely due to the finite electron beam energy spread of 0.1 eV, which is not included in the theoretical calculations.

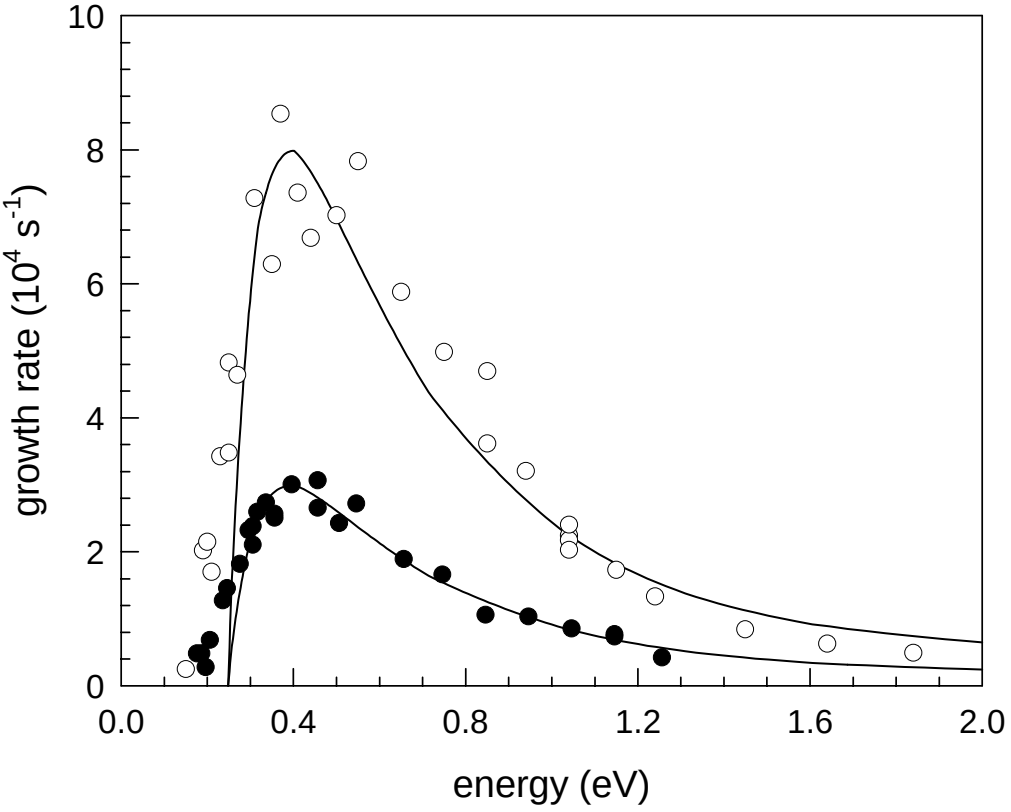

Figure 5.6: Growth rates for the beam-plasma interaction in the quadrupole trap. The solid and open circles are the data using a 0.03 and 0.08 μA electron beam, respectively. The solid lines are the results of a cold-fluid theory by Dubin [21]. There are no fitted parameters used between the theory and experiment.

5.4 Chapter Summary

We have investigated a beam-plasma system in a new and interesting range of beam energies, studying a transit-time instability in a positron plasma stored in a quadrupole Penning trap. Using a new technique that we developed to generate cold electron beams, we have been able to measure the growth rate of the center of mass mode from the onset of the instability through the maximum in the growth rate. Comparison of the data with the results of a cold-fluid theory by Dubin [21] shows excellent agreement over the entire range of energies and beam currents studied.

The experiments presented here represent further studies of the electron-positron beam-plasma system. These experiments are the only ones currently

being conducted on this type of plasma, or on any type of equal-mass plasma. Although the techniques described here are not suitable for studying the properties of equal-mass plasmas where the species have no net currents relative to each other, it is likely to be the only experimentally accessible system available for studies of this type of plasma in the near term. The excellent agreement between the experimental results and an analytical cold-fluid theory is therefore gratifying. Experiments of this type are likely to be of value in extending our understanding of equal-mass plasmas. The combination of the ability to efficiently accumulate and store large numbers of positrons with the new technique to produce cold electron beams should provide opportunities to investigate other interesting phenomena in electron-positron plasmas.

Chapter 6

Conclusion

6.1 Summary

The ability to generate a versatile beam of intense, cold positrons has opened up a new range of energies for the experimental study of positron-matter interactions. The cold beam, which is discussed in Chapter 3, is formed from a thermalized reservoir of cold positrons stored in a Penning trap. The beam has an energy spread of 18 meV and can be generated with a beam energy ranging from $<$ 50 meV upward, making it the only tool available for the study of positron-matter interactions significantly below 1 eV. We have also been able to generate cold electron beams using this technique. Although not as exotic an application as for positrons, the generation of a cold electron beam in a strong magnetic field is a non-trivial task, and allows us to peruse experimental studies of electron-positron plasmas where a strong field is necessary for positron confinement.

Using the cold positron beam we have begun to study low-energy positron-atomic and positron-molecular interactions (see Chapter 4). The first positron-molecule vibrational excitation cross section measurements were performed using the original positron accumulator by studying positron excitation of the υ_3 vibrational mode of CF_4 at energies down to the onset of the vibrational mode. Positron-atom DCS at energies below that of any previous measurement have also been studied. These measurements, which included positron excitation of argon and krypton at energies from 0.4 to 2.0 eV were compared with theoretical predictions [23, 74, 75] and agree well over a large range of energies and angles.

Using information gained from these experiments and an improved understanding of positron scattering in a strong magnetic field, a new scattering apparatus was designed and constructed. This apparatus, which is now attached to the new positron accumulator, has a greatly improved signal-to-noise ratio, data collection rate, and magnetic ratio, allowing the measurement of positron scattering cross sections in a fraction of the time required in the earlier apparatus. By performing scattering experiments on the new apparatus, we have expanded

our understanding of the strengths and limitations of positron scattering in a strong magnetic field, and expect that future design enhancements will expand further our ability to study low-energy positron-matter interactions.

Currently a broad study of positron-molecule vibrational excitation cross sections is being performed. Studies include the vibrational excitation of CO, CO_2, and CH_4 with energies ranging from 0.5 up to 7 eV. Multiple vibrational modes have been measured in a number of these molecules. For example, in CO_2, we have measured the vibrational cross sections for the υ_3 and υ_2 modes which occur at 291 and 83 meV, respectively. The ability to perform these state-of-the-art vibrational cross section measurements is, in turn, a motivation for future theoretical calculations. Initial comparison of the measured positron-CO_2 inelastic cross sections with theoretical predictions by Gianturco [29] are in excellent agreement over almost the entire energy range calculated, and plans to calculate vibrational cross sections for the other molecules being studied are in progress [27].

The first application of the method developed to produce a cold magnetized electron beam was used to extend our understanding of electron-beam positron-plasma instabilities. Chapter 5 discusses growth rate measurements of the instability caused by transmitting the cold electron beam through a positron plasma stored in a quadrupole well. Using the cold beam we have been able to extend the range of energies in which the transit-time instability can be studied to include the onset through the maximum in growth rate. Comparison of the measured instability growth rates with predictions from a cold fluid theory [21] are in excellent absolute agreement over the entire range of energies and beam currents studied.

6.2 Future Work

6.2.1 Cold Beams

Because the techniques used to form the cold positron and electron beams are not fully matured, it is reasonable to expect that modifications of the beam formation method will yield improvements in the energy spread, intensity, and versatility of the beam. We are currently constructing a high-field (5 tesla) ultra-high-vacuum positron storage stage [103]. In this device, the positron plasmas will be surrounded by electrodes cooled to 4 kelvin, and so the plasma will equilibrate to this temperature by cyclotron radiation. Using this accumulator as a reservoir of cold positrons, in principle, it should be possible to produce extremely bright milli-electron-volt positron beams for use in a broad range of experiments.

Another experiment under investigation is the ability to compress the positron plasma using a rotating electric field. It has been shown for electrons that by applying a rotating electric asymmetry onto the walls of the confining electrodes,

a torque can be applied to the plasma, thereby compressing it [2]. A decrease in the plasma radius by a factor ~ 4.5, accompanied by an increase in the plasma density of 20, was observed in these experiments. Use of this technique in the high-field stage should increase the plasma density and the brightness of extracted positron beams.

Lastly, there are two approaches being considered to improve the overall efficiency of the positron accumulator, and therefore the signal-to-noise ratio of our positron-matter experiments. The first is to increase the trapping efficiency of the new positron accumulator. The current efficiency of the accumulator is still 50% less than that of the earlier accumulator. Indications point to a reduced positron life time through the second stage, caused by positron transport to the walls. By enlarging the diameter of the second stage electrode, the trapping efficiency is hoped to improve to at least 30% from its current value of 20%. The second approach is to increase the efficiency of our neon moderator by changing the cone geometry. The cone geometry used in the new accumulator was designed to maximize the number of the high energy positrons from the source that can hit it. Unfortunately, the efficiency of the new cone geometry is ~ 5 times worse than the cone geometry used on the earlier accumulator. We expect that by changing the cone geometry back to one that more closely resembles the original design, the moderator efficiency should improve by a factor of ~ 5.

6.2.2 Positron Atomic and Molecular Scattering

The low-energy atomic and molecular scattering experiments described in this thesis are examples of scattering processes that can be studied using the new apparatus. Plans to systematically measure total inelastic cross sections for positron-molecule interactions are already underway. We have also shown that these techniques can be used to measure total cross sections at energies as low as 50 meV. By measuring the total cross section for partially fluorinated hydrocarbons (i.e., CH_4 through CF_4), we hope to improve our understanding of the anomalous large annihilation rates observed in positron-hydrocarbon interactions [54].

Another interesting related topic to study is the possible existence and nature of low-lying positron-molecule resonances and weakly bound states. For example, by measuring the elastic scattering cross section in the regime where $ka < 1$, where k is the momentum of the positron and a is the s-wave scattering length, it should be possible to use asymptotic formulae to measure the sign and magnitude of the scattering length, and thereby determine the expected energies of bound states or resonances [39].

Possible techniques to measure the scattering cross section, $\sigma(E_0, E, \theta)$ when both elastic and inelastic processes are present are also being investigated. Here, E_0 and E are the incident and scattered positron energies and θ is the scattering angle. This can, in principal, be accomplished by taking retarding-potential

data at different magnetic ratios M, and using analysis techniques similar to tomographic reconstruction to unfold the scattering cross section [7].

One of the current deficiencies of the scattering experiments described here is the inability to distinguish back-scattered particles from forward-scattered particles (see Section 4.5). One possible solution to this problem is to incorporate a set of $E \times B$ drift plates in between the scattering cell and accumulator. By placing appropriate potentials on the $E \times B$ drift plates, the positron path can be altered depending on the direction of travel along the magnetic field. Therefore, by placing $E \times B$ plates and an energy analyzer between the scattering cell and the accumulator, the energy distribution for both the back-scattered and forward-scattered positrons could be measured. This would then allow measurement of the complete DCS from nearly 0 to 180 degrees. For total inelastic cross sections, this technique would allow separate measurements of the contribution due to the forward and backward inelastic scattering cross sections, providing information about the angular dependence of the inelastic scattering cross section.

The study of surfaces is also an interesting area of future research. There are a number of novel surface science techniques, such as Positron Annihilation Lifetime Spectroscopy (PALS), which can be enhanced using the cold positron beam [37]. In PALS positrons injected into the surface are trapped and subsequently annihilate in vacancy-type defects. By measuring the positron lifetime, information about the defects can be obtained. Using the cold beam can enhance this technique, allowing a depth profile of the void size and concentration. This is accomplished by varying the beam energy, and therefore the depth at which the positron is implanted into the solid.

Lastly, although a broad survey of annihilation rates using room-temperature positrons has been completed [53–55], there is only a small body of work on positron annihilation as a function of positron energy below the threshold for positron formation [66]. The cold beam could be used to greatly expand these studies. For example, the parameter $E_{e^+} - E_i + E_{\mathrm{Ps}}$ is the energy difference between the positron energy, E_{e^+}, and the positronium formation threshold energy, $E_i - E_{\mathrm{Ps}}$, and it is thought to play a significant role in annihilation rates. Recent theories predict resonance behavior in the annihilation rates at energies $E_{e^+} - E_i + E_{\mathrm{Ps}} \sim 0$, and this effect could be studied experimentally using the cold positron beam.

6.2.3 Electron-Positron Plasmas

There are a number of experiments that could now be performed to increase our understanding of the electron-beam positron-plasma system, beyond those described in Chapter 5. For example, by stabilizing the center of mass mode with an active feedback system [106], it should be possible to measure the growth rate of higher order modes. There may also be effects worth studying at energies

below the instability onset. In this energy range, cold-fluid theory predicts that there is a band of energies at which the growth rate is negative, and this should therefore have a damping effect on the center of mass oscillations. By exciting the center of mass mode to large amplitudes before the electron beam traverses the plasma, we can, in principal, study these negative growth rates.

Also re-examining the two-stream instability generated in the cylindrical trap [34] using the cold electron beam will likely yield interesting new insights. It is clear from the earlier experiments that the onset of the instability occurs at an energy below that studied. It should be possible to use the new cold beam to measure the heating rate for a range of positron energies from the onset of the instability through the maximum heating rate. Another interesting aspect of the two-stream instability is the method in which the plasma is heated. The heating is assumed to arise from the growth of unstable plasma modes which then transfer energy to the plasma particles. Direct measurements of these unstable modes should prove insightful. To measure them, a pickup electrode must be located near the plasma in order to detect the image charge generated by the (presumably short wavelength) plasma oscillations. We believe that these experiments can offer further insight into the underlying physics of the instability.

Prospects for studying *relativistic* electron-positron plasmas, which is of keen interest to the astrophysics community, continue to be poor, at least in the intermediate term. Obtaining Debye lengths that are smaller than the plasma size, which is essential for the charge cloud to behave as a plasma, would require about five orders of magnitude more positrons than can now be accumulated. However, progress in the accumulation of positron plasmas continues. For example, the number of positrons now available is three orders of magnitude more than the first positron plasma created in 1989, and a further two orders of magnitude increase can be expected within the next few years [102].

6.3 Concluding Remarks

We have developed a new technique to produce intense, cold, magnetized positron and electron beams. Using these beams we have studied both electron-beam positron-plasma instabilities and two-body interactions of low-energy positrons with atoms and molecules in an energy regime previously inaccessible to experiment. This research has expanding our knowledge of positron-matter interactions at low-energies and has helped to improve our ability to perform such experiments in a magnetic field. The work presented here demonstrates the effectiveness of this approach; we expect that the cold beam technique will continue to make advances in both positron-atomic and beam-plasma physics.

References

[1] T. Akahane, T. Chiba, N. Shiotani, S. Tanigawa, T. Mikado, R. Suzuki, M. Chiwaki, T. Yamazaki, and T. Tomimasu. Stretching of slow positron pulses generated with an electron linac. *Applied Physics A*, A51:146–150, 1990.

[2] F. Anderegg, E. M. Hollmann, and C. F. Driscoll. Rotating field confinement of pure electron plasmas using Trivelpiece-Gould modes. *Physical Review Letters*, 81:4875–4878, 1998.

[3] C. D. Anderson. The apparent existence of easily deflectable positives. *Science*, 76:238–239, 1932.

[4] C. D. Anderson. The positive electron. *Physical Review*, 43:491–494, 1933.

[5] T. J. Bartel, S. Plimpton, J. Johannes, and J. Payne. *Icarus: A 2D Direct Simulation Monte Carlo (DSMC) Code for Parallel Computers, Users Manual - V3.0.* Sandia National Laboratories Report SAND96-0591, 1996.

[6] H. Boehmer, M. Adams, and N. Rynn. Positron trapping in a magnetic mirror configuration. *Physics of Plasmas*, 2:4369–71, 1995.

[7] D. Boyd, W. Carr, R. Jones, and M. Seidl. Energy lost by an electron beam in interaction with a plasma. *Physics Letters*, 45A:421, 1973.

[8] B. H. Bransden. *Case studies in atomic collision physics.* North-Holland, Amsterdam, 1969.

[9] D. T. Britton, P. A. Huttunen, J. Mkinen, E. Soininen, and A. Vehanen. Positron reflection from the surface potential. *Physical Review Letters*, 62:2413–2416, 1989.

[10] B. L. Brown, W. S. Crane, and A. P. Mills, Jr. Generation of highly monochromatic positrons using cold moderators. *Applied Physics Letters*, 48:739–41, 1986.

[11] K. F. Canter, P. G. Coleman, T. C. Griffith, and G. R. Heyland. Measurement of total cross sections for low energy positron-helium collisions. *Journal of Physics B*, 5:L167 – 70, 1972.

[12] M. Charlton. Experimental studies of positrons scattering in gases. *Reports on Progress in Physics*, 48:737, 1985.

[13] M. Charlton and G. Laricchia. The production of low energy positrons and positronium. *Hyperfine Interactions*, 76:97–113, 1993.

[14] L. G. Christophorou, J. K. Olthoff, and M. V. V. S. Rao. Electron interactions with CF_4. *Journal of Physical and Chemical Reference Data*, 25:1341–1388, 1996.

[15] P. G. Coleman, T. C. Griffith, and G. R. Heyland. A time of flight method of investigating the emission of low energy positrons from metal surfaces. *Royal Society of London A*, 331:561–569, 1972.

[16] P. G. Coleman and J.D. McNutt. Measurement of differential cross section for the elastic scattering of positrons by argon atoms. *Physical Review Letters*, 42:1130–1133, 1979.

[17] D. G. Costello, D. E. Groce, D. F. Herring, and J. W. McGowan. Evidence for the negative work function associated with positrons in gold. *Physical Review B*, 5:1433–1439, 1972.

[18] W. S. Crane and A. P. Mills Jr. Subnanosecond bunching of a positron beam. *Review of Scientific Instruments*, 56(9):1723, 1985.

[19] G. Danby and J. Tennyson. R-matrix calculations of vibrationally resolved positron-N_2 scattering cross sections. *Journal of Physics B*, 24:3517–3529, 1991.

[20] P. A. M. Dirac. On the annihilation of electrons and protons. *Proceedings of the Cambridge Philosophical Society*, 26:361–375, 1930.

[21] D. H. E. Dubin. Private communication, 1995.

[22] A.E Dubinov, V.D. Selemir, and A.V. Sudovtsov. Excitation of wake fields in an electron-positron plasma by an ultra relativistic proton beam. *Physics Letters A*, 223:186–188, 1996.

[23] V. A. Dzuba, V. V. Flambaum, G. F. Gribakin, and W. A. King. Many-body calculations of positron scattering and annihilation from noble gas atoms. *Journal of Physics B*, 29:3151–3175, 1996.

[24] D. L. Eggleston, C. F. Driscoll, B. R. Beck, A. W. Hyatt, and J. H. Malmberg. Parallel energy analyzer for pure electron plasma devices. *Physics of Fluids B*, 4:3432–9, 1992.

[25] D. A. Fischer, K. G. Lynn, and D. W. Gidley. High-resolution angle-resolved positron reemission spectra from metal surfaces. *Physical Review B*, 33(7):4479, 1986.

[26] J. P. Freidberg and D. W. Hewett. Eigenmode analysis of resistive mhd stability by matrix shooting. *Journal of Plasma Physics*, 26:177, 1981.

[27] F. A. Gianturco. Private communication, 2000.

[28] F. A. Gianturco and T. Mukherjee. The role of vibrational coupling in low-energy positron scattering from molecular targets. *Journal of Physics B*, 30:3567–3581, 1997.

[29] F. A. Gianturco, T. Mukherjee, and P. Paioletti. Positron scattering from polar molecules: Rotovibrationally inelastic collisions with CO targets. *Physical Review A*, 56:3638–3652, 1997.

[30] F. A. Gianturco and P. Paioletti. Elastic collisions and rotational excitation in positron scattering from CO_2 molecules. *Physical Review A*, 55:3491–3503, 1997.

[31] S. J. Gilbert, R. G. Greaves, and C. M. Surko. Positron scattering from atoms and molecules at low energies. *Physical Review Letters*, 82:5032–5035, 1999.

[32] S. J. Gilbert, C. Kurz, R. G. Greaves, and C. M. Surko. Creation of a monoenergetic pulsed positron beam. *Applied Physics Letters*, 70:1944–1946, 1997.

[33] E. Gramsch, J. Throwe, and K. G. Lynn. Development of transmission positron moderators. *Applied Physics Letters*, 51:1862–4, 1987.

[34] R. G. Greaves and C. M. Surko. An electron-positron beam-plasma experiment. *Physical Review Letters*, 75:3846–3849, 1995.

[35] R. G. Greaves and C. M. Surko. Solid neon moderator for positron trapping experiments. *Canadian Journal of Physics*, 51:445–8, 1996.

[36] R. G. Greaves and C. M. Surko. Antimatter plasmas and antihydrogen. *Physics of Plasmas*, 4:1528–1543, 1997.

[37] R. G. Greaves and C. M. Surko. Technological applications of trapped positrons. In J. Bollinger, R. Spencer, and R. Davidson, editors, *Nonneutral Plasma Physics III*, pages 19–28. AIP Conference Proceedings 498, 1999.

[38] R. G. Greaves, M. D. Tinkle, and C. M. Surko. Creation and uses of positron plasmas. *Physics of Plasmas*, 1:1439–1446, 1994.

[39] G. F. Gribakin. Mechanisms of positron annihilation on molecules. *Physical Review A*, A61:022720, 2000.

[40] T. C. Griffith and G. R. Heyland. Experimental aspects of the study of the interaction of low-energy positrons with gases. *Physics Reports*, 39:169, 1978.

[41] E. M. Gullikson, A. P. Mills, Jr., W. S. Crane, and B. L. Brown. Absence of energy loss in positron emission from metal surfaces. *Physical Review B*, 32:5484–6, 1985.

[42] D. Gyobu, J. Sakai, M. Eda, T. Neubert, and M Nambu. Emission of electromagnetic waves from langmuir waves generated by electron beam instabilities in pair plasmas. *Journal of the Physical Society of Japan*, 68:471–77, 1999.

[43] A. Hamada and O. Sueoka. Total cross section measurements for positrons and electrons colliding with molecules II. HCL. *Journal of Physics B*, 27:5055–5064, 1994.

[44] G. Hart, J. M. Curtis, and Bryan G. Peterson. Velocity space dynamics of a pure-electron plasma during a dump. *Bull. Am. Phys. Soc.*, 41:1523, 1996.

[45] O. Heil and A. Arsenjewa-Heil. Eine neue methode zur erzeugung kurzer ungedampfter electromagnetischen wellen von grosser intensitaten. *Zeit. fur Phys.*, 95:752, 1935.

[46] R. H. Howell, T. E. Cowan, J. Hartley, P. Sterne, and B. Brown. Positron beam lifetime spectroscopy of atomic scale defect distributions in bulk and microscopic volumes. *Applied Surface Science*, 116:7–12, 1997.

[47] L. D. Hulett, Jr., D. L. Donohue, J. Xu, T. A. Lewis, S. A. McLuckey, and G. L. Glish. Mass spectrometry studies of the ionization of organic molecules by low-energy positrons. *Chemical Physics Letters*, 216:236–40, 1993.

[48] L. D. Hulett, Jr., T. A. Lewis, and D. L. Donohue. The extraction of linac-generated slow positrons using the single gap accelerator technique. In L. Dorikens-Vanpraet, M. Dorikens, and D. Seger, editors, *Procedings of the 8th International Conference of Positron Annihilation*, pages 589–591, Belgium, 1989. Singapore: World Scientific.

[49] G. M. A. Hyder, M. S. Dababneh, Y. F. Hsieh, W. E. Kauppila, C. K. Kwan, M. Mahdavi-Hezaveh, and T. S. Stein. Positron differential elastic-scattering cross-section measurements for argon. *Physical Review Letters*, 57:2252–2255, 1986.

[50] T. Intrator, N. Hershkowitz, and R. Stern. Beam-plasma interactions in a positive ion-negative ion plasma. *Physics of Fluids*, 26:1942–8, 1983.

[51] N. Iwamoto. Collective modes in nonrelativistic electron-positron plasmas. *Physical Review E*, 47:604–611, 1993.

[52] Koji Iwata. *Positron Annihilation on Atoms and Molecules.* PhD thesis, University of California, San Diego, 1997.

[53] Koji Iwata, R. G. Greaves, T. J. Murphy, M. D. Tinkle, and C. M. Surko. Measurements of positron-annihilation rates on molecules. *Physical Review A*, 51:473–87, 1995.

[54] Koji Iwata, G. Gribakin, R. G. Greaves, C. Kurz, and C. M. Surko. Positron annihilation on large molecules. *Physical Review A*, A61:022719, 2000.

[55] Koji Iwata, G. F. Gribakin, R. G. Greaves, and C. M. Surko. Positron annihilation with inner-shell electrons in noble gas atoms. *Physical Review Letters*, 79:39–42, 1997.

[56] A. Jain. Vibrational excitation of $\nu' = 1$ and 2 levels of CO molecules by positron impact below the positron formation threshold. *Journal of Physics B*, 19:L379–L384, 1986.

[57] F. Joliot. Production artificielle d'lments radioactifs. *Journal de Physique*, 5:153, 1934.

[58] L. Jong-Liang and J.J.T. Yates. Electron gun for producing a low energy, high current and uniform flux electron beam. *Journal of Vacuum Science and Technology A*, 12:2795, 1994.

[59] I. Kanazawa, Y. Ito, M. Hirose, H. Abe, O. Sueoka, S. Takamura, A. Ichimiya, Y. Murata, F. Komori, K. Fukutani, S. Okada, and T. Hattori. Production of an intense slow positron beam by using an electron linac and its applications. *Applied Surface Science*, 85:124–131, 1995.

[60] W. E. Kauppila and T. S. Stein. Comparisons of positron and electron scattering by gases. *Advances in Atomic, Molecular, and Optical Physics*, 26:1 – 49, 1990.

[61] R. Khatri, K. G. Lynn, A. P. Mills, Jr., and L. O. Roellig. A pulsed positronium beam. *Materials Science Forum*, 105-110:1915–18, 1992.

[62] M. Kimura, M. Takeawa, and Y. Itikawa. Mode dependence in vibrational excitation of a CO_2 molecule by electron and positron impacts. *Physical Review Letters*, 80:3936–3939, 1998.

[63] T. Kitanishi, J. Sakai, K. Nishikawa, and J. Zhao. Electromagnetic waves emitted from an electron-positron plasma cloud moving across a magnetic field. *Physical Review E*, 53:6376–81, 1996.

[64] P. Kubica and A. T. Stewart. Thermalization of positrons and positronium. *Physical Review Letters*, 34:852–855, 1975.

[65] C. Kurz, S. J. Gilbert, R. G. Greaves, and C. M. Surko. New source of ultra-cold positron and electron beams. *Nuclear Instruments and Methods in Physics Research B*, 143:188–194, 1998.

[66] C. Kurz, R. G. Greaves, and C. M. Surko. Temperature dependence of positron annihilation rates in noble gases. *Physical Review Letters*, 77:2929–32, 1996.

[67] C. Kuyatt and J. Sympson. Electron monochromator design. *Review of Scientific Instruments*, 38:103, 1967.

[68] G. Laricchia and M. Charlton. Collisions involving antiparticles. *Philosophical Transactions of the Royal Society London, Series A*, 357:2259–1277, 1999.

[69] K. G. Lynn, M. Weber, L. O. Roellig, A. P. Mills, Jr., and A. R. Moodenbaugh. A high intensity positron beam at the Brookhaven reactor. In J. W. Humbertston and E. A. G. Armour, editors, *Atomic Physics with Positrons. Proceedings of a NATO Advanced Research Workshop*, pages 161–74. Plenum, New York, NY, USA, 1987.

[70] G.Z. Machabeli, S.V. Vladimirov, and D.B. Melrose. Nonlinear dynamics of an ordinary electromagnetic mode in a pair plasma. *Physical Review E*, 59:4552–8, 1999.

[71] J. H. Malmberg and C. F. Driscoll. Long-time containment of a pure electron plasma. *Physical Review Letters*, 44:654–7, 1980.

[72] A. Mann and F. Linder. Low-energy electron scattering from halomethanes: I. elastic differential cross section for e-CF_4 scattering. *Journal of Physics B*, 25:533–543, 1992.

[73] H. Massey. Slow positrons in gases. *Physics Today*, 29:42, 1976.

[74] R. P. McEachran, A. G. Ryman, and A. D. Stauffer. Positron scattering from argon. *Journal of Physics B*, 12:1031–31, 1979.

[75] R. P. McEachran, A. D. Stauffer, and L. E. M. Campbell. Positron scattering from krypton and xenon. *Journal of Physics B*, 13:1281–92, 1980.

[76] F. C. Michel. Theory of pulsar magnetospheres. *Reviews of Modern Physics*, 54:1–66, 1982.

[77] A. P. Mills. Further improvements in the efficiency of low-energy positron moderators. *Applied Physics Letters*, 37:667–8, 1980.

[78] A. P. Mills, Jr. Surface analysis and atomic physics with slow positron beams. *Science*, 218:335–40, 1982.

[79] A. P. Mills, Jr. Positron and positronium sources. *Experimental Methods in the Physical Sciences*, 29A:39–68, 1995.

[80] A. P. Mills, Jr. and E. M. Gullikson. Solid neon moderator for producing slow positrons. *Applied Physics Letters*, 49:1121–3, 1986.

[81] A. P. Mills Jr., E. D. Shaw, R.J. Chichester, and D. M. Zuckerman. Production of slow positron bunches using a microtron accelerator. *Review of Scientific Instruments*, 60(5):825, 1989.

[82] S. Mori, Y. Katayama, and O. Sueoka. Total cross sections for positrons and electrons colliding with SiH_4 and CF_4. *Atomic Collisions Research Japan*, 11:19, 1985.

[83] Muller. Experimentelle untersuchungen uber elektronen-schwingungen. *Hoch. U. Elek.*, 43, 1934.

[84] T. J. Murphy and C. M. Surko. Positron trapping in an electrostatic well by inelastic collisions with nitrogen molecules. *Physical Review A*, 46:5696–705, 1992.

[85] Y. Nakamura. Recent electron swarm studies using rare gas/molecular gas mixtures. In R. W. Crompton, M. Hayashi, D. E. Boyd, and T. Makabe, editors, *Gaseous Electronics and Their Applications*, pages 178–200. KTK Scientific, Tokyo, 1991.

[86] T. M. O'Neil. A confinement theorem for nonneutral plasmas. *Physics of Fluids*, 23:2216–2218, 1980.

[87] T. M. O'Neil. Nonneutral plasmas have exceptional confinement properties. *Comments on Plasma Physics and Controlled Fusion*, 5:213–17, 1980.

[88] Eric Ottewitte and Alex H. Weiss, editors. *AIP Conference Proceedings 303*. American Institute of Physics, New York, 1992.

[89] A. Passner, C. M. Surko, M. Leventhal, and A. P. Mills, Jr. Ion production by positron-molecule resonances. *Physical Review A*, 39:3706–9, 1989.

[90] A. D. Rogava, S. M. Mahajan, and V. I. Berezhiani. Velocity shear generated alfven waves in electron-positron plasmas. *Physics of Plasmas*, 3:3545–3555, 1996.

[91] G. G. Ryzhikh and J. Mitroy. Positronic lithium, an electronically stable li-e^+ ground state. *Physical Review Letters*, 79:4124–4126, 1997.

[92] J. Sakai, M. Eda, and W. Shiratori. Wave generation and particle acceleration in an electron-positron plasma. *Physica Scripta*, T75:67–71, 1998.

[93] J. P. Schermann and F. G. Major. Characteristics of electron-free confinement in an rf quadrupole field. *Applied Physics*, 16:225–230, 1978.

[94] P. J. Schultz and K. G. Lynn. Interaction of positrons beams with surfaces, thin films, and interfaces. *Reviews of Modern Physics*, 60:701–79, 1988.

[95] D. Segers, J. Paridaens, M. Dorikens, and L. Dorikens-Vanpraet. Beam handling with a penning trap of a linac-based slow positron beam. *Nuclear Instruments and Methods in Physics Research*, A337:246–52, 1994.

[96] V. Skarva, V.I. Berezhiani, and G. Carlini. Propagation of relativistic electron-positron solitary waves across an ambient magnetic field. *Physica Scripta*, 57:456–9, 1998.

[97] L. Stenflo, P. K. Shukla, and M. Y. Yu. Nonlinear propagation of electromagnetic waves in magnetized electron-positron plasmas. *Astrophysics and Space Science*, 117:303–8, 1985.

[98] G. A. Stewart. Nonlinear electrostatic waves in equal-mass plasmas. *Journal of Plasma Physics*, 50:521–36, 1993.

[99] T.E. Stringer. Electrostatic instabilities in current-carrying and counterstreaming plasmas. *Plasma Physics*, 6:267, 1964.

[100] O. Sueoka and A. Hamada. Total-section measurements for 0.3-10 eV positrons scattering on N_2 CO, and CO_2 molecules. *Journal of the Physical Society of Japan*, 62:2669–2674, 1993.

[101] O. Sueoka, Y. Ito, T. Azuma, S. ¡ori, K. Katsumura, H. Kobayashi, and Y. Tabata. Production of slow positrons using an electron LINAC. *Japanese Journal of Applied Physics*, 24:222–224, 1985.

[102] C. M. Surko, S. J. Gilbert, and R. G. Greaves. Progress in creating low-energy positron plasmas and beams. In J. J. Bollinger, R. L. Spencer, and

R. C. Davidson, editors, *Non-Neutral Plasma Physics III*, pages 3–12, New York, 1999. American Institute of Physics.

[103] C. M. Surko, R. G. Greaves, K. Iwata, and S. J. Gilbert. Atomic and molecular physics using positron accumulation techniques – summary and a look to the future. *Nuclear Instruments and Methods in Physical Research B*, in press.

[104] C. M. Surko, M. Leventhal, and A. Passner. Positron plasma in the laboratory. *Physical Review Letters*, 62:901–4, 1989.

[105] R. Suzuki, Y. Kobayashi, T. Mikado, H. Ohgaki, M. Chiwaki, and T Yamazaki. An intense pulsed positron beam. *Hyperfine Interactions*, 84:345, 1994.

[106] P. Tham, A.K. Sen, A. Sekiguchi, R. G. Greaves, and G. A. Navratil. Feedback-modulated ion beam stabilization of a plasma instability. *Physical Review Letters*, 67:404–7, 1991.

[107] V. Tsytovich and C. B. Wharton. Laboratory electron-positron plasma—a new research object. *Comments on Plasma Physics and Controlled Fusion*, 4:91–100, 1978.

[108] J. Walz, C. Zimmermann, L. Ricc., M. Prevedelli, and T. W. Hansch. Combined trap with the potential for antihydrogen production. *Physical Review Letters*, 75:3257–60, 1995.

[109] C. S. Weimer, J. J. Bollinger, F. L Moore, and D. J. Wineland. Electrostatic modes as a diagnostic in penning trap experiments. *Physical Review A*, 49:3842–3853, 1994.

[110] N. Zafar, J. Chevallier, G. Laricchia, and M. Charlton. Single-crystal nickel foils as positron transmission-mode moderators. *Journal of Physics D*, 22:868–70, 1989.

[111] G. P. Zank and R. G. Greaves. Linear and nonlinear modes in nonrelativistic electron-positron plasmas. *Physical Review E*, 51:6079, 1995.

[112] J. Zhao, K. I. Nishikawa, J. I. Sakai, and T. Neubert. Study of nonlinear alfven waves in an electron-positron plasma with a three-dimensional electromagnetic particle code. *Physics of Plasmas*, 1:103–8, 1994.

[113] J. Zhao, J. I. Sakai, and K. I. Nishikawa. Coalescence of two parallel current loops in a nonrelativistic electron-positron plasma. *Physics of Plasmas*, 3:844–52, 1996.

[114] S. Zhou, H. Li, W. E. Kauppila, C. K. Kwan, and T. S. Stein. Measurements of total and positronium cross sections for positrons and electrons scattered by hydrogen atoms and molecules. *Physical Review A*, 55:361–368, 1997.